



NATIONAL TECHNICAL UNIVERSITY OF ATHENS
INTERDISCIPLINARY INTERDEPARTMENTAL POSTGRADUATE PROGRAM
"MATERIALS SCIENCE AND TECHNOLOGY"

TECHNISCHE UNIVERSITÄT BERLIN
INSTITUTE of NANOPHOTONIK

MASTER THESIS

**III-Nitride Emitters and Converters:
Built-in polarization-induced electric fields, built-in potential, and
effective doping concentration**

by

Electronics Engineer Georgios G. Roumeliotis

Supervisor

Assist. Prof. Dr. Dimitra N. Papadimitriou (NTUA)

Co-Supervisor

Prof. Dr. Michael Kneissl (TU-Berlin)

ATHENS, 2017



NATIONAL TECHNICAL UNIVERSITY OF ATHENS
INTERDISCIPLINARY INTERDEPARTMENTAL POSTGRADUATE PROGRAM
"MATERIALS SCIENCE AND TECHNOLOGY"

TECHNISCHE UNIVERSITÄT BERLIN
INSTITUTE of NANOPHOTONIK

MASTER THESIS

III-Nitride Emitters and Converters:

**Built-in polarization-induced electric fields, built-in potential, and
effective doping concentration**

by

Electronics Engineer Georgios G. Roumeliotis

Supervisor:

Assist. Prof. Dr. Dimitra N. Papadimitriou (NTUA)

Co-Supervisor:

Prof. Dr. Michael Kneissl (TU-Berlin)

Examination-Committee:

Assist. Prof. Dr. Dimitra N. Papadimitriou (NTUA)

Assoc. Prof. Christos Argirousis (NTUA, School of Chemical Engineering)

Prof. Evangelos Christoforou (NTUA, School of Electrical & Computer Engineering)

ATHENS, 2017

This work is part of the Master Thesis of Georgios G. Roumeliotis, student in the NTUA Interdisciplinary Interdepartmental Postgraduate Studies Program "Materials Science and Technology".

It was carried out partly at the National Technical University of Athens at the
***Laboratory of Material Growth and Optical Characterization /
Development of Low Cost – High Efficiency CIS/CIGS Photovoltaics***
Founder and Scientific Responsible: Assist. Prof. Dr. Dimitra N. Papadimitriou

and partly at the Technical University of Berlin at the
Laboratory of Nanophotonics of the Institute of Solid State Physics
Executive Director: Prof. Dr Michael Kneissl

Acknowledgements

For the optical characterization, the following NTUA laboratory facilities were used:

***LABORATORY of Material Growth and Optical Characterization /
Development of Low Cost – High Efficiency CIS/CIGS Photovoltaics***

Host Institution: National Technical University of Athens

Cooperating Institutions:

Centre for Renewable Energy Sources and Saving (CRES)

Technische Universität Berlin (TU-Berlin)

Helmholtz Zentrum Berlin für Materialien und Energie (HZB)

Founder and Scientific Responsible: Assist. Prof. Dr. Dimitra Papadimitriou

The PIN diode samples were developed by S. Neugebauer and Prof. Dr. A. Dadgar.

For the electrical and structural characterization Prof. Dr Michael Kneissl's research work group facilities were used, at the Laboratory of Nanophotonics of the Technical University of Berlin.

The CIGS (Cu(In,Ga)Se₂) thin film solar cell, used as the reference sample was developed by Prof. Dr. Martha-Christina Lux-Steiner's research work group at the Laboratory of Compound Semiconductors of the Department of Solar Energy Research of the Helmholtz Centre Berlin for Materials and Energy.

This master thesis was funded by the Erasmus+ Programme of the European Union for the time period of 02.01.2017 – 31.08.2017.

A special acknowledgement is attributed to Assist. Prof. Dr. Dimitra Papadimitriou for the exceptional amount of time kindly invested in the author's Master Thesis.

Prof. Dr. Michael Kneissl is greatly acknowledged as well as his workgroup members, notably Dr. Tim Wernicke, Norman Susilo, Martin Guttman and Matthias Dreier for their kind support to this Master Thesis.

The NTUA and TU-Berlin members of the Mechanic Workshop are acknowledged for the constructions related to the present Thesis.

Motivation

The motivation behind this work is the quantification and possibly optimization of processes in ultra-violet light emitting diodes (UV LEDs), specifically the Electric fields present which have an effect on the properties of diodes and ultimately LEDs. The materials used in this work are exclusively wurtzite III nitrides: AlN, InN, GaN, and ternary combinations of these binary material systems; all layers of the fabricated devices were grown in the perpendicular to the c-plane direction. Engineering efficient LEDs, Laser diodes (LDs) and photodiode sensors of a predetermined per application narrow band gap in the UVC range (100nm-280nm) is a main future goal. A vast variety of applications includes water purification and photodiode sensors. The piezoelectric [1]-[10], and spontaneous [2], [3], [6], [10] electric fields are affecting the band gap through the quantum confined Stark effect (QCSE), as described in Chapter 1.2, and also the efficiency of such devices. Direct predetermination of the material band-gap and the device efficiency by selecting just the semiconductor or metal element fraction is not possible. Nevertheless, a closer view at the nature of the inherent electric fields generated by the incorporation of a controlled heterostructure inside the intrinsic region of a PIN-LED is expected to decipher the detected response and efficiency and reveal the phenomena behind them. Other factors such as strain/stress [9], [11]-[19], and electronic network efficiency analysis at certain biases and frequencies are also necessary for an effective interpretation leading to the desirable engineering techniques and utilizing a wide range of materials and structure design parameters. Fig. 1 depicts the vast variety of UV light applications.

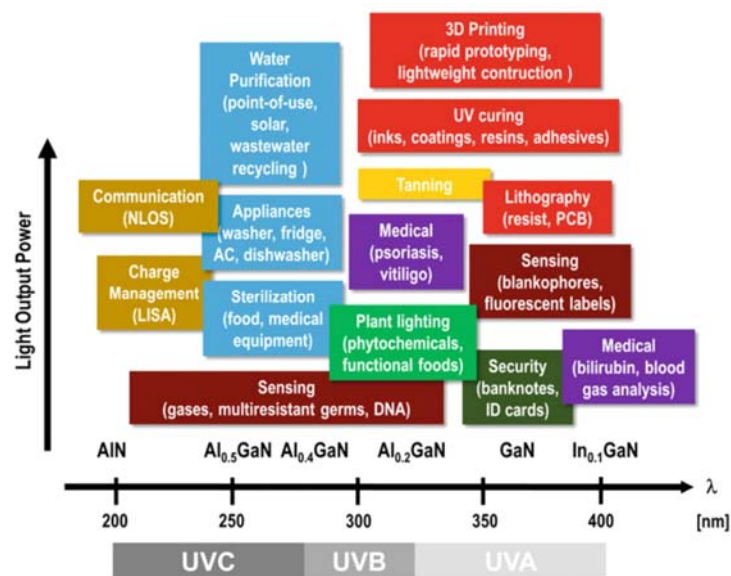


Figure 1 A vast variety of UV light applications [20].

Abstract

The internal electric fields and the electro-optical response of nearly lattice-matched InGaN/GaN and InAlN/GaN heterostructures were experimentally quantified. Capacitance-Voltage (CV) measurements were performed on PIN diodes based on InGaN/GaN and InAlN/GaN quantum wells grown on (0001) sapphire substrates by metalorganic vapour phase epitaxy (MOVPE). Large polarization fields dependent on the indium content were quantified on $\text{In}_{0.055}\text{Ga}_{0.945}\text{N}/\text{GaN}$ (-2.25 ± 1.25 MV/cm) and $\text{In}_{0.17}\text{Al}_{0.83}\text{N}/\text{GaN}$ (5.90 ± 3.10 MV/cm), $\text{In}_{0.20}\text{Al}_{0.80}\text{N}/\text{GaN}$ (5.99 ± 2.76 MV/cm), $\text{In}_{0.22}\text{Al}_{0.78}\text{N}/\text{GaN}$ (5.26 ± 1.25 MV/cm) based heterostructures and associated with the electro-optical properties of the PIN diodes studied by electroreflectance (ER) and electroluminescence (EL) spectroscopy. The electro-optically modulated field (0.04 MV/cm) was determined from Franz-Keldysh Oscillations (FKOs) related to the barrier regions of the InGaN/GaN QW heterostructure. The internal field strength and direction were in agreement with theoretical predictions.

Περίληψη

Τα εσωτερικά ηλεκτρικά πεδία και η ηλεκτρο-οπτική απόκριση ετεροδομών InGaN/GaN και InAlN/GaN με παραπλήσιες πλεγματικές σταθερές ποσοτικοποιήθηκαν πειραματικά. Μετρήσεις Χωρητικότητας-Τάσης (CV) πραγματοποιήθηκαν σε διόδους PIN βασισμένες σε κβαντικά πηγάδια InGaN/GaN και InAlN/GaN, οι οποίες αναπτύχθηκαν σε υπόστρωμα sapphire (0001) μέσω επιταξίας μεταλλοργανικών ατμών (metalorganic vapour phase epitaxy, MOVPE). Ισχυρά πεδία πόλωσης ποσοτικοποιήθηκαν ως συνάρτηση του ποσοστού Ινδίου σε ετεροδομές βασισμένες σε $\text{In}_{0.055}\text{Ga}_{0.945}\text{N}/\text{GaN}$ (-2.25 ± 1.25 MV/cm) και $\text{In}_{0.17}\text{Al}_{0.83}\text{N}/\text{GaN}$ (5.90 ± 3.10 MV/cm), $\text{In}_{0.20}\text{Al}_{0.80}\text{N}/\text{GaN}$ (5.99 ± 2.76 MV/cm), $\text{In}_{0.22}\text{Al}_{0.78}\text{N}/\text{GaN}$ (5.26 ± 1.25 MV/cm) και συσχετίστηκαν με τις ηλεκτρο-οπτικές ιδιότητες των διόδων PIN με φασματοσκοπία Ηλεκτροανακλαστικότητας (Electroreflectance, ER) και Ηλεκτροφωταύγειας (Electroluminescence, EL). Το ηλεκτρο-οπτικά διαμορφωμένο πεδίο (0.04 MV/cm) προσδιορίστηκε από τις ταλαντώσεις Franz-Keldysh (FKOs), οι οποίες σχετίζονται με τις περιοχές φραγμάτων δυναμικού της ετεροδομής του κβαντικού πηγαδιού (QW) InGaN/GaN. Η ισχύς και η διεύθυνση των εσωτερικών πεδίων είναι σε συμφωνία με τις θεωρητικές προβλέψεις.

Table of contents

	<i>Page</i>
<i>Cover</i>	<i>1</i>
<i>Inner Cover Page</i>	<i>2</i>
<i>Title</i>	<i>3</i>
<i>Acknowledgements</i>	<i>4</i>
<i>Motivation</i>	<i>5</i>
<i>Abstract (Περίληψη)</i>	<i>6</i>
<i>Table of Contents</i>	<i>7</i>
<i>List of abbreviations</i>	<i>11</i>
 <i>Introduction: Theory</i>	
<i>1. Group III Nitrides</i>	<i>13</i>
1.1 Materials & Devices.....	14
1.1.1 Materials.....	14
1.1.1.1 Spontaneous & Piezoelectric polarization of GaN.....	17
1.1.1.2 Band structure.....	18
1.1.2 Devices.....	22
1.1.2.1 Light Sources.....	22
1.1.2.1.1 UVC LEDs.....	22
1.1.2.2 Detectors.....	23
1.2 Quantum Confined Semiconductor Structures: Quantum Wells.....	24
1.2.1 Quantum Confined Stark Effect.....	26
1.3 Growth Processes.....	28
1.3.1 Epitaxy.....	28
1.3.2 MOVPE growth.....	28
1.3.3 Metal Contacts Technology.....	28
1.4 Characterization Techniques.....	29
1.4.1 Optical characterization by ER and EL Spectroscopy.....	29
1.4.2 Electrical characterization by Capacitance-Voltage Profiling.....	30

2. Experiment.....	31
2.1 Samples & layer structures.....	31
2.1.1 Growth methods.....	31
2.1.1.1 MOVPE Calibration Samples.....	31
2.1.2 Investigated Samples.....	32
2.1.3 Sample structure (TEM, XRD)	38
2.2 Contacts.....	39
2.2.1 Selected metals.....	39
2.2.2 Parasitic Schottky Contacts.....	39
2.3 Instrumentation setup & Measurement Procedure.....	40
2.3.1 Optical characterization by Modulation Spectroscopy.....	40
2.3.1.1 Modulation Spectrometer (ER & PR).....	53
2.3.1.2 ER instrumentation setup.....	53
2.3.1.3 ER instrumentation setup optimization.....	60
2.3.1.4 Lock-in amplifier settings optimization.....	60
2.3.1.5 Passive filter optimization.....	61
2.3.1.6 Function generator settings optimization.....	61
2.3.1.7 Optics adjustments.....	62
2.3.1.8 Holder & probes optimization.....	63
2.3.1.9 Measurement procedure.....	65
2.3.1.10 ER reference sample.....	66
2.3.2 Electrical characterization by Capacitance-Voltage Profiling.....	67
2.3.2.1 CVP instrumentation setup.....	68
2.3.2.2 CVP calibration procedure.....	71
2.3.2.3 Measurement procedure (CVPT, ZfT, I-V).....	73
3. Results & discussion	
3.1 Electroreflectance & Electroluminescence Spectroscopy.....	75
3.1.1 ER Spectroscopy.....	75
3.1.1.1 Reference sample, ER spectra & fitting.....	75
3.1.1.2 GaN PIN diode ER spectra.....	78
3.1.1.3 InGaN/GaN PIN diode ER spectra.....	79
3.1.1.4 InAlN/GaN PIN diode ER spectra.....	84
3.1.2 Electroluminescence.....	85
3.1.2.1 GaN PIN diode EL spectra.....	85
3.1.2.2 InGaN/GaN PIN diode EL spectra.....	88
3.1.2.3 InAlN/GaN PIN diode EL spectra.....	89

3.2 Capacitance-Voltage Profiling.....	93
3.2.1 Conventional CVP diode equivalent circuit.....	93
3.2.2 Advanced CVP diode equivalent circuit.....	95
3.2.2.1 Nonlinearities.....	96
3.2.2.2 Voltage dependence.....	96
3.2.2.2.1 R(V).....	96
3.2.2.2.2 C(V).....	97
3.2.2.3 Frequency dependence.....	99
3.2.2.4 Transient & steady state response.....	100
3.2.3 Advanced method for accurate CVP.....	101
3.2.3.1 Using directly measured properties.....	101
3.2.3.1.1 Impedance.....	102
3.2.3.1.2 Phase.....	102
3.2.3.1.2.1 Group delay.....	103
3.2.3.2 Contacts mapping.....	103
3.2.3.3 Labview program.....	103
3.2.3.4 Advanced method equations.....	104
3.2.4 Parasitic Schottky contacts impedance.....	106
3.2.5 Theoretical verification of CVP linearity.....	106
3.2.6 Calculation of the Polarization Fields.....	107
3.2.6.1 Measurements analysis.....	107
3.2.6.2 Theoretical values & equations.....	107
3.2.6.3 Experimental values & equations.....	113
3.2.6.4 Comparison.....	118
3.2.6.5 Overall error evaluation combining methods.....	120
3.2.7 Additional Considerations.....	123
3.2.7.1 Light conditions.....	123
3.2.7.2 Voltage regulation.....	123
3.2.7.3 Limitations.....	123
3.2.7.3.1 Voltage.....	124
3.2.7.3.2 Current.....	124
3.2.7.4 Selecting the f- & V-range.....	124
3.2.7.5 Samples degradation & breakdown.....	125
3.2.7.6 Parasitic Diffusion capacitance in forward bias.....	125
3.2.7.7 V_{bi} dependence on N , ϵ_r , N_i , d_u & d_{DHS} (SiLENCE simulation).....	125
3.2.8 Schottky model.....	127
3.2.9 Schottky with intrinsic region model.....	127
3.2.10 p-n junction model.....	127

3.2.11 PIN diode model.....	128
3.2.11.1 Constant Doping profile.....	128
3.2.11.2 General case doping profile.....	128
3.2.11.3 $N(w)$	129
4. Conclusions.....	130
4.1 Summary.....	130
4.2 Future Perspectives.....	131
4.2.1 Equivalent circuit analysis as a means to higher efficiencies.....	131
4.2.2 Future Schottky samples structure design.....	131
4.2.3 Future samples with $E_g(\text{DHS}) < E_g(\text{buffer})$	131
5. References.....	132
6. Curriculum vitae and list of publications.....	142

List of abbreviations

AC	Alternating signal
CB	Conduction band
CIGS	(Cu(In,Ga)Se ₂)
CP	Critical Point
CVP	Capacitance-Voltage Profiling
CVPT	CVP utilizing also the phase response
D	Dimension
DAP	Donor-acceptor pair recombination
DC	Direct and constant signal
DHS	Double heterostructure
DUT	Device under test
E _g	Energy band gap
EM	Electromodulation, electric-field-modulated reflectivity, transmission
ER	Electroreflectance
EL	Electroluminescence
Eq.	Equation
Fig.	Figure
FKOs	Franz-Keldysh Oscillations
HRTEM	High-resolution Transmission Electron Microscopy
inf	Infinite, too high to be measured
I-V	Current voltage measurement
LED	Light-emitting diode
LD	Laser diode
MM	Multimeter
NIR	Near-Infrared
NUV	Near-Ultraviolet
PC	Personal Computer
QCSE	Quantum Confined Stark effect
QW	Quantum well
R	Reflectance
rms	Root mean square
SNR	Signal-to-Noise ratio
TDFE	Third derivative functional form
TEM	Transmission Electron Microscopy
TFSC	Thin film solar cell

TLM	Transmission line measurement
VB	Valence band
Vis	Visible, referring to the Visible spectrum of light
Vp-p	Volts peak-to-peak
WZ	Wurtzite
ZB	Zinc blende
ZfT	Impedance and phase frequency responses
ΔR	Reflectance change, the Reflectance of the sample is modulated by the use of an externally induced electric field

1

Group-III Nitrides

The optical properties of III-V nitrides are much less affected by dislocations than those of III-V arsenides and III-V phosphides [21]. In this context, the nitrides are a main focus in LEDs research and development [2]-[4], [14], [17], [20], [22]-[66]. Properties of the InAlGaN materials system are depicted in Fig. 1.1. Apparently, the entire 400-700nm visible spectrum can be theoretically covered by the InAlGaN materials system.

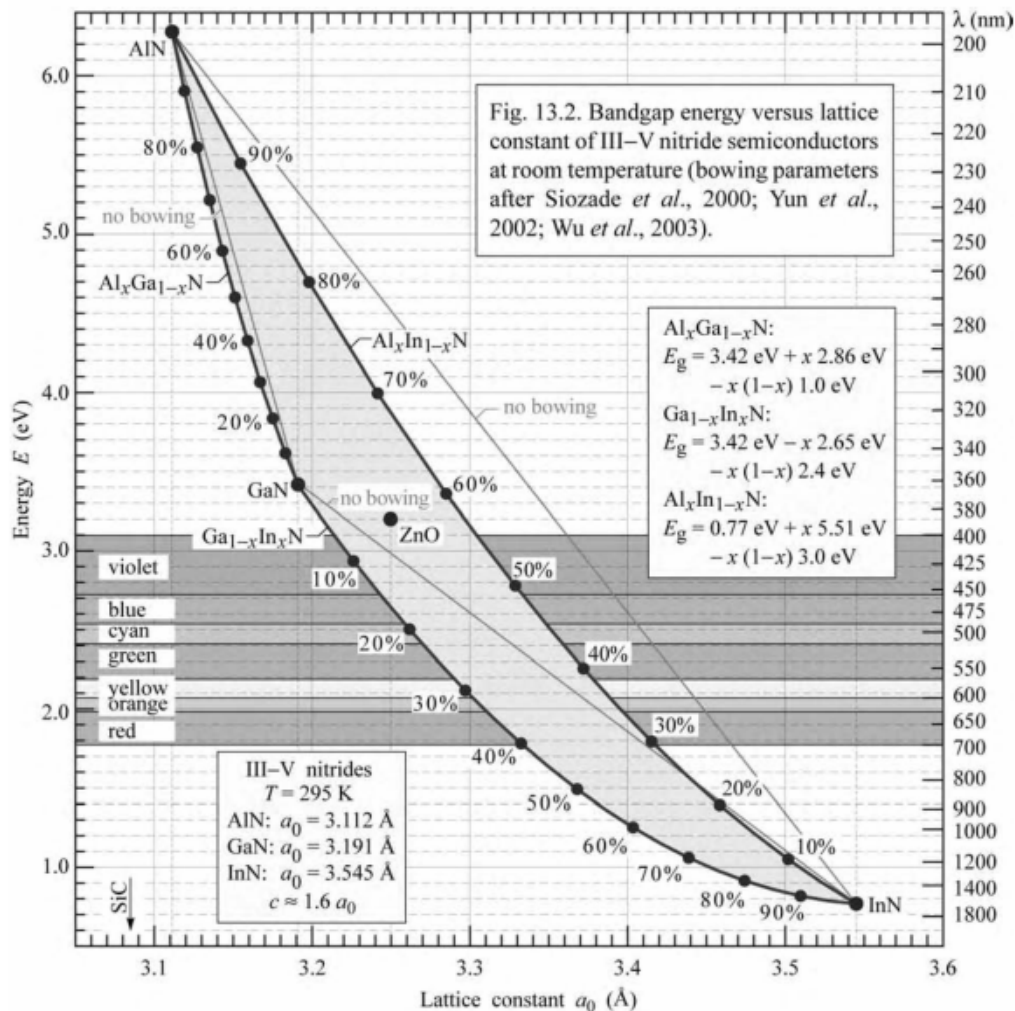


Figure 1.1 Properties of the InAlGaN materials system [21].

1.1

Materials & Devices

1.1.1

Materials

The InGaN material as a combination of InN and GaN was first developed and commercially available in the 1990s. Efficient green and blue light emitters were successfully engineered and soon became the primary material system for this part of the visible spectrum. Since most material systems are greatly affected by the inherent high concentration of threading dislocations in epitaxial films grown on GaN substrates, one of the greatest advantages of the InGaN materials system is its high radiative efficiency. Densities of the threading dislocations are typically in the range of 10^7 - 10^9 cm^{-2} . Various difficulties are present in InGaN growth including the fact that the quality of InGaN films is degrading with increasing Indium content due to the re-evaporation of Indium from the grown surface. Similarly, the InAlGaN system can theoretically cover a wider spectral range; AlN with a band gap of 6.015 eV equivalent to 206.13nm at 300K is well within the UVC range of 100nm-280nm paving the path towards engineering devices for various applications [21], [28], [37], [39], [46], [49], [67]-[89] in the whole spectral range (0.77eV-6.028eV [21]) of the InAlGaN material system. The common epitaxial growth direction of III-V nitrides is in the direction normal to the c-plane of the hexagonal wurtzite structure. Growth in this direction results in polarization charges [90]-[96] present at the layer interface and thus electric fields affecting the optical and electrical properties of nitride materials devices [21], [27]. The direction of this internal electric field [21], [97] depends on the strain induced by the lattice mismatch [98], [99] between the deposited film and the substrate as presented in Fig. 1.1.1.1.

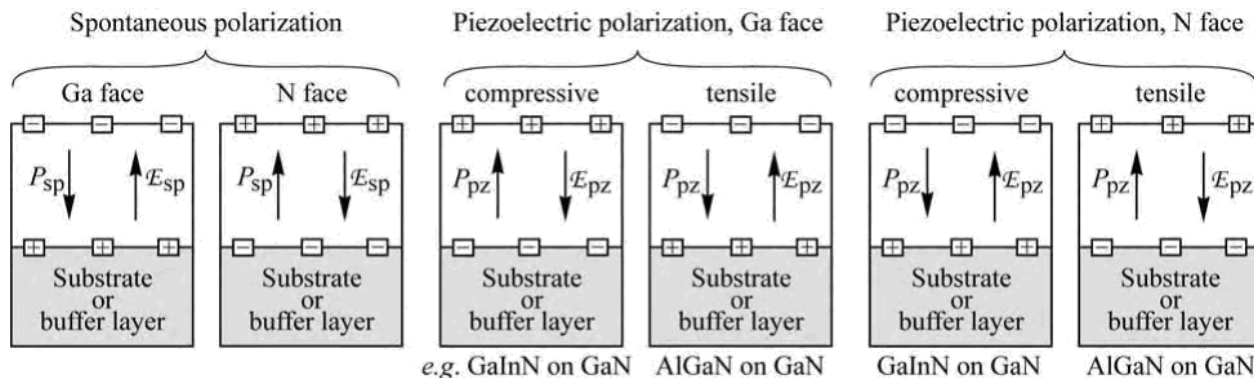


Figure 1.1.1.1 Surface charge and direction of electric field and polarization field for spontaneous and piezoelectric polarization in III-V nitrides for Ga- and N-face orientation [21].

Due to their highly ionic nature III nitride semiconductors are most thermally stable when arranged into the wurtzite (WZ) crystal structure (e.g. α -GaN [41]), with a cohesive energy per bond of 2.20 eV for GaN [67]. They are also able to form metastable zinc-blende (ZB) crystal structures (e.g. β -GaN [41]) when grown heteroepitaxially on cubic substrates or when large lattice mismatches occur between the epitaxially grown material and the substrate; however, a reduction in the cohesive energy for the ZB arrangement (~ -9.88 meV per atom for GaN) results in the WZ structure being energetically favourable [100]. The WZ and ZB GaN crystal structures are shown in Fig. 1.1.1.2.

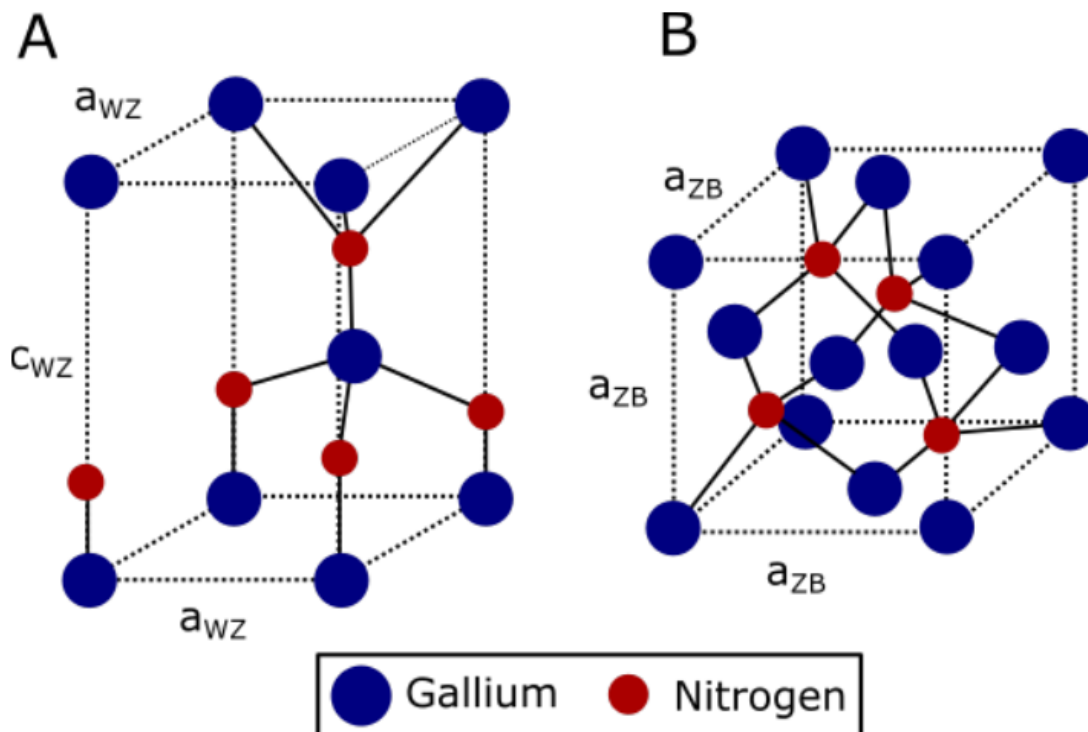


Figure 1.1.1.2 The WZ (A) and ZB (B) GaN crystal structures. Gallium atoms are shown in blue and nitrogen atoms in red. The lattice constants (a and c) for the WZ and ZB structures are indicated.

The WZ crystal structure contains two hexagonal close-packed sub-lattices that interpenetrate to create alternating hexagonal layers with a stacking sequence BABAB in the c-direction [0001]. These alternating hexagonal layers can be represented by 2 repeating unit cells consisting of 5 atoms each in a tetrahedral atomic configuration (Fig. 1.1.1.3).

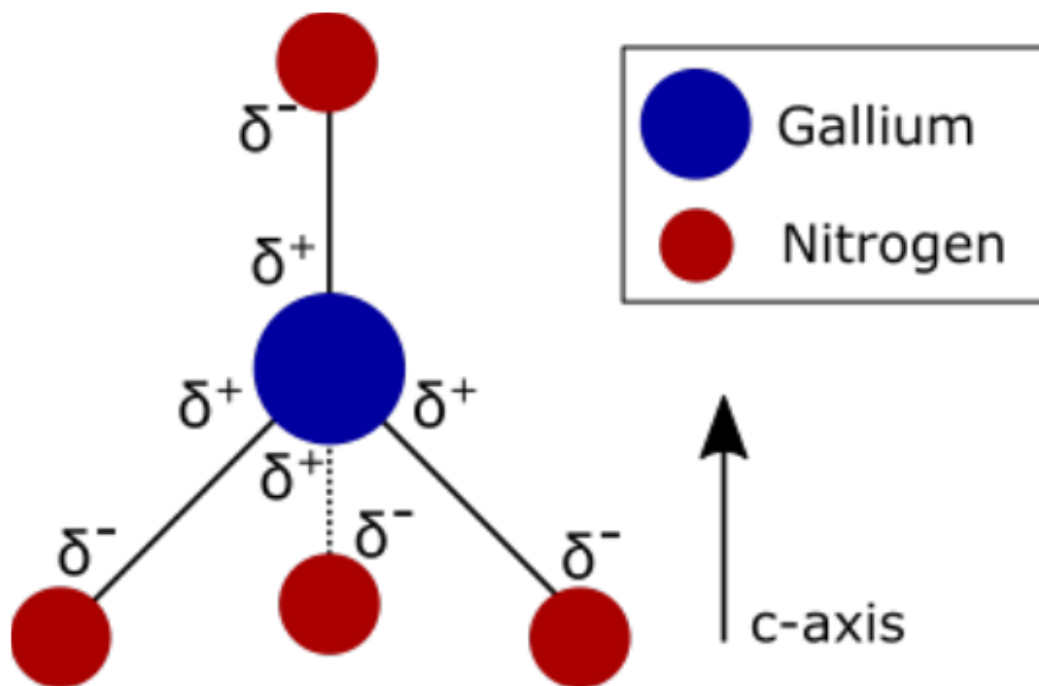


Figure 1.1.1.3 The tetrahedral atomic configuration formed for the gallium and the nitrogen atoms in GaN. Indicated are the dipole moments.

For WZ GaN, the first unit cell consists of a group III atom (such as gallium) surrounded by 4 nitrogen atoms and the second unit cell consists of a nitrogen atom surrounded by 4 group-III atoms. The resulting III nitride unit cells are described by 2 lattice constants, c and a , which represent the spacing between the nitrogen atoms in the hexagonal plane (0001) and the spacing between the nitrogen atoms of the alternating hexagonal planes in the c -direction respectively. The metastable ZB crystal is also constructed by the 2 interpenetrating face-centred cubic crystal lattices; however, in this case, there are 3 hexagonal layers created with a stacking sequence ABCABC that results in the arrangement of the ZB crystal structure. Table 1.1.1.1 contains the lattice constants a and c , and the fundamental energy band gap (E_g) for GaN and InN with the WZ and ZB crystal arrangements.

Table 1.1.1.1 Fundamental properties of GaN and InN in the WZ and ZB crystal arrangements [100].

Parameter	Wurtzite		Zinc-blende	
	GaN	InN	GaN	InN
300K lattice constant a, Å	3.189	3.544	4.50	4.98
300K lattice constant c, Å	5.185	5.718	4.50	4.98
E_g (T=0K), eV	3.510	0.78	3.299	0.78

1.1.1.1

Spontaneous & Piezoelectric polarization of GaN

For the WZ crystal, in table 1.1.1.1 and Fig. 1.1.1.2, the lattice constants a and c are different revealing the crystal anisotropy. It can also be observed that the WZ unit cell is non-centrosymmetric (Fig. 1.1.1.2) and lacks symmetry along the c-axis [0001] in which a gallium-nitrogen bond lays. Due to the asymmetry between the length and angle of this Ga-N bond and the 3 other GaN-N bonds at the base of the pyramid (Fig. 1.1.1.3), even when unstrained, the sum of the crystal polarisation does not equal 0 in the c-direction resulting in a dipole moment across the crystal. The dipole moment induces a spontaneous polarisation field directed either in the +c direction or -c direction depending on whether at the surface there are nitrogen or gallium atoms, respectively [100]. Due to the dipole moment and resulting spontaneous polarisation fields aligned in the c-direction, the c-plane is often referred to as the “polar” plane. In addition to the spontaneous polarisation field there may also exist a strain-induced piezoelectric polarisation field in the c-direction. When biaxial strain is applied across the crystal structure, the individual Ga-N bond lengths and angles are altered causing a variation in the overall magnitude of the polarisation field. Hence, the total internal polarisation field for a given layer is expressed as an addition of the spontaneous polarisation and strain-induced piezoelectric polarisation. These large internal polarisation fields have a significant influence on the optical properties of GaN-based heterostructures grown in the c-direction due to the creation of a surface charge, when the polarisation constant is suddenly altered, and induce an electric field directed along the c-axis.

1.1.1.2

Band structure

The III nitride semiconductor group possesses direct band gaps [101] over a large energy range. It is the ability to create direct gap ternary alloys such as $\text{In}_x\text{Ga}_{1-x}\text{N}$, $\text{In}_x\text{Al}_{1-x}\text{N}$ or $\text{Al}_x\text{Ga}_{1-x}\text{N}$ with energies beyond those of the constituent binary III nitride semiconductors that makes them perfect for the use in optoelectronic devices.

The band structure for III nitrides in the WZ crystal arrangement is shown in Fig. 1.1.1.2.1 on an $E(k)$ diagram over the Γ -point where $k = 0$ with a single $n=1$ conduction band (CB) and 3 separate $n=1$ valence split bands (VBs) with parabolic dispersions. In reality, the bands extend over a larger range of momentum with non-parabolic dispersions, even at the Γ -point. There may also be more than 1 ($n=2,3,4,\dots$) confined states for both the CB and VBs, however, for simplicity, only $n=1$ confined states will be considered from here on.

Near the band edges, i.e., bottom of CB (E_C) and top of VB (E_V), the $E(k)$ relationship can be approximated by a quadratic equation, where m^* is the associated effective mass [68]:

$$E(k) = \frac{\hbar^2 k^2}{2m^*} \tag{1.1.1.2.1}$$

As shown in Fig. 1.1.1.2.1, along a given direction, the two top valence bands can be approximated by two parabolic bands with different curvatures: the heavy-hole band (the wider band in k -axis with smaller $\partial^2 E / \partial k^2$) and the light-hole band (the narrower band with larger $\partial^2 E / \partial k^2$).

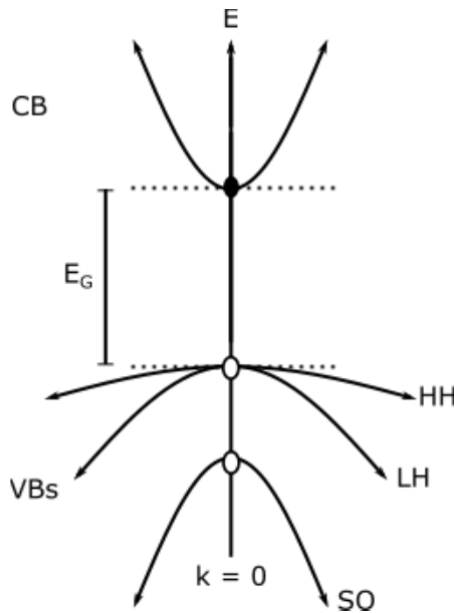


Figure 1.1.1.2.1 A simple $E(k)$ diagram around the Γ -point at $k=0$ for a III nitride semiconductor, featuring a CB and the heavy hole (HH), light hole (LH), and split off (SO) $n=1$ VBs.

The CB originates from electrons orbiting positively charged group-III atoms in a single s-type shell orbital that is spherical in k-space. Therefore, the s-shell CB is symmetric along all possible axes in k-space. The VBs originate from hole states in p-type shell orbitals around nitrogen atoms. P-type shells possess 3 orbitals; the P_x orbital in the x-direction, the P_y orbital in the y-direction, and P_z orbital in the z-direction [0001]. Fig. 1.1.1.2.2 shows the CB and VB orbitals in k-space.

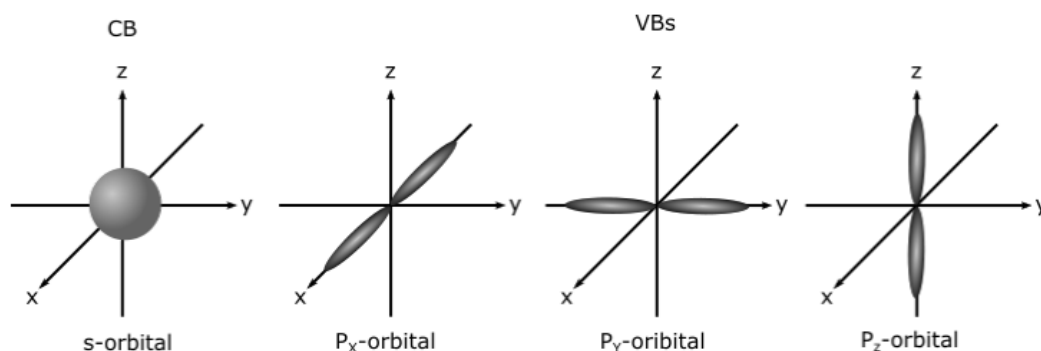


Figure 1.1.1.2.2 The k-space symmetry of the s-orbital (CB) and p-orbitals (VBs). The s-orbital is symmetric along all axes whereas the p-orbitals are only symmetric along the direction they are orientated.

As the CB electrons originate from a single, symmetric s-shell orbital that lays relatively far from the nucleus, they remain largely unaffected by the spin-orbit interaction and crystal field splitting. However, the VB holes are affected by the relativistic spin-orbit interaction and the crystal field splitting. The VB orbitals lay closer to the atomic nucleus than the CB orbital, hence using classical approximations the electrons in the VBs must be moving relatively faster. As the electrons are moving at relativistic speeds through the electric field induced by the nucleus, a large magnetic force is generated. Due to differences between the angular momentum and spin for electrons in the 3 different VBs, the perturbation for each VB structure is different. Therefore, the spin-orbit interaction acts to lift the degeneracy of the 3 VBs as well as further alter the k-space dispersion of each. In addition, there is the crystal field splitting acting on the P_z orbital as this is the only orbital that lays in the same direction as the crystal field, the z-direction. The crystal field splitting results in a relatively large shift in the P_z VB energy. The 3 VBs are commonly referred to as the heavy hole (HH, P_x), light hole (LH, P_y), and split-off (SO, P_z) VBs. The effect that the spin-orbit and crystal field interactions have on the VBs is demonstrated in Fig. 1.1.1.2.3.

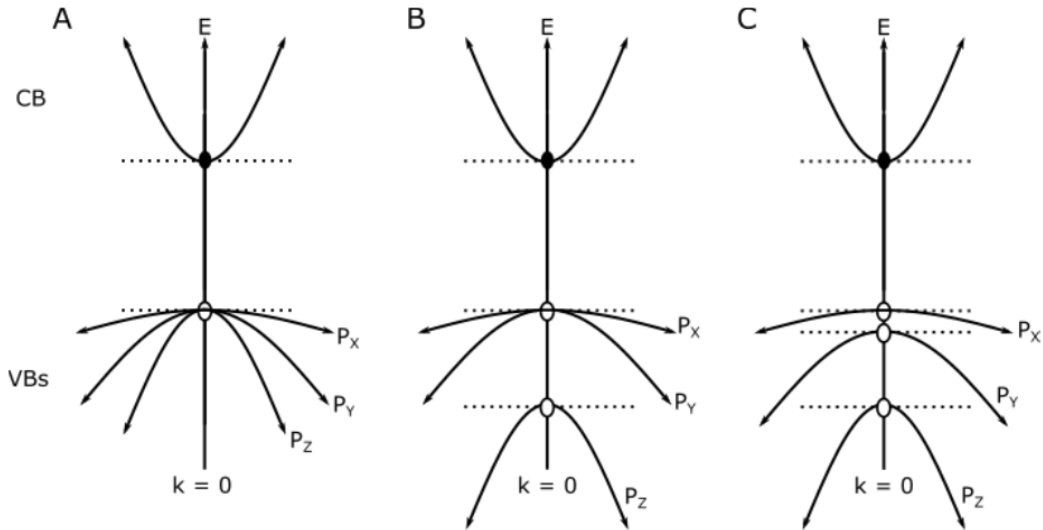


Figure 1.1.1.2.3 Demonstration of how the crystal field and spin-orbit interactions affect the VB structures. A) Degenerate VBs under no influence. B) VBs affected by the crystal field interaction. C) VBs affected by the crystal field and spin orbit interactions.

For c-plane GaN, the biaxial strain is isotropic in the x- and y-directions due to the WZ C_{6v} crystal symmetry and the equal bond lengths in those directions. Isotropic biaxial strain in the x-y direction acts to increase the band gap energy of P_x and P_y VBs equally by preserving k-space symmetry in the x-y plane, however, the P_z VB energy is shifted by a relatively larger amount. For the c-plane orientation, where the growth direction extends in the z-direction, only photons associated with transitions from the CB to the in-plane P_x and P_y VB orbitals are optically allowed. As the x-y symmetry is unbroken by the isotropic strain for c-plane WZ GaN, the photon emission from c-plane GaN samples is unpolarised, when measured perpendicular to the growth plane. In Fig. 1.1.1.2.4, a schematic energy diagram of valence-band top for wurtzite and zinc blende semiconductors is demonstrated.

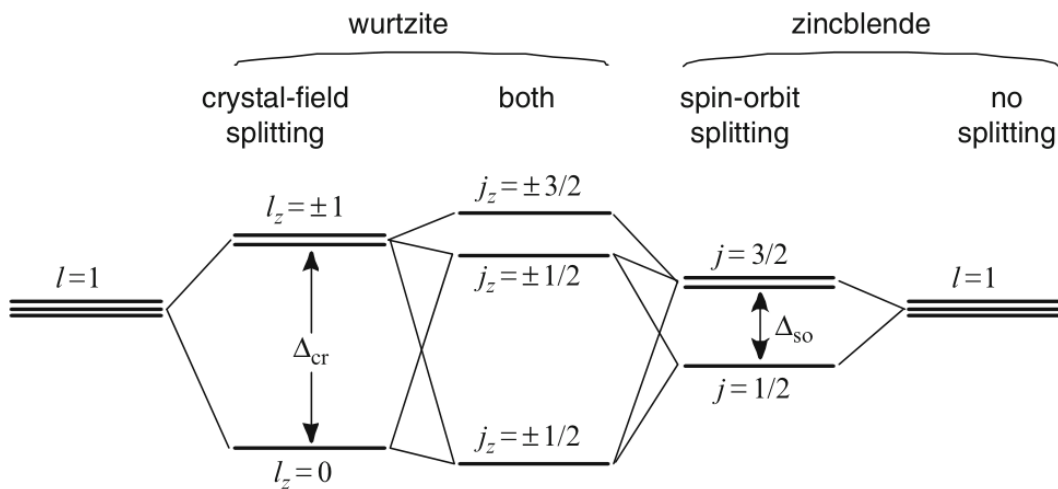


Figure 1.1.1.2.4 Schematic energy diagram of valence-band top for wurtzite and zinc blende semiconductors [25].

Similar to other semiconductor systems, the band gap energy varies as a function of temperature and can be calculated using the Varshni equation [100]:

$$E_g(T) = E_g(0) - \frac{\alpha T^2}{T + \beta} \quad (1.1.1.2.2)$$

where $E_g(T)$ is the band gap energy at any given temperature T (K), $E_g(0)$ is the band gap energy at 0K, and α (meV/K) and β (K) are fitting parameters specific to the semiconductor crystal. The α and β fitting parameters, however, are a function of crystal strain, hence the parameters may vary for heteroepitaxially grown samples where there is a lattice mismatch between the semiconductor material and the substrate. For heteroepitaxial samples, the parameters can instead be determined by experimental fitting to the data or by using deformation potential calculations.

1.1.2

Devices

For the UV range, UV devices of the AlGa_N material system can be utilized with wavelengths less than 360nm. It is often the case that more complicated structures such as superlattices are used to relax or retain the strain induced by the mismatching lattices. Essentially, when AlGa_N thicker films are grown on GaN buffer layers, the AlGa_N is partly allowed to relax to a certain extent, which may be not desirable [21]. Typical examples of photonic devices are LEDs, LDs, and photodiodes used as photodetectors and solar cells.

1.1.2.1

Light Sources

Electromagnetic radiation in the wavelength range of 400nm-700nm can be perceived by the human eye. Sensing white light is based on the fact that the human eye retina incorporates three cones sensitive to different wavelengths. Essentially, they have to be excited at a specific ratio for the light to be colourless [21]. Nitrides light sources include LEDs and LDs. Parts of the non-visible spectrum are also useful in various applications [26] . The infrared spectrum is commonly defined as 700nm-1mm and the UV as 10nm-400nm, the intermediate space being the visible light.

1.1.2.1.1

UVC LEDs

UVC LEDs are LEDs that emit light mainly inside the UVC range. The complete UVC range is 100nm-280nm. Its effectiveness as a disinfection method is exploited to kill or deactivate microorganisms by destroying nucleic acids and disrupting their DNA, termed as Ultraviolet germicidal irradiation (UVGI). Conventional UVC light sources include fluorescent lamps without their common phosphor coating at the 253.7nm and 185nm mercury peaks. An efficiency of 30%-40% is typical at converting the electrical power input to the UVC light output. Such lamps are used for food and water purification. Additionally, deuterium lamps are used in High performance liquid chromatography (HPLC). All these are potential applications for the currently under research and development UVC LEDs. Of course, the barriers of cost, efficiency and durability have to be overcome before entering the modern market.

1.1.2.2

Detectors

Photodiodes are commonly used as photodetectors in several ranges of the spectrum for a large variety of applications ranging from motion detectors to gas sensors. Nearly all of these devices are based on p-n junction principles. A common type of such photodetectors is the PIN photodiode. Apart from the wavelength, other important factors are the minimum and maximum detectable and tolerated power densities, and the response time. The response time in a PIN photodiode is determined by the transit times of the photogenerated carriers across the width of the intrinsic layer. Increasing the layer thickness allows more photons to be absorbed which increases the output signal per input light intensity but unavoidably reduces the speed of response because carrier life times become longer [67].

1.2

Quantum Confined Semiconductor Structures: Quantum Wells

When electrons are free to move in a bulk semiconductor in all directions (3-D), their energy above the conduction-band edge is continuous, given by the relationship to their momentum Eq. (1.1.1.2.1) [68]:

$$E - E_C = \frac{\hbar^2}{2m_e^*} (k_x^2 + k_y^2 + k_z^2) \quad (1.2.1)$$

A quantum well (QW) confines electrons or holes in a two-dimensional (2-D) system. It is formed by two heterojunctions or three layers of materials such that the middle layer has the lowest E_C for an electron well or the highest E_V for a hole well. Quantum wells provide a means of confining the free carriers to a narrow quantum well region by using the two barrier regions cladding the quantum well. In a quantum well, carriers are confined in one direction, say in the x-coordinate such that $k_x=0$. The energy within this well is no longer continuous with respect to the x-direction, but becomes quantized in sub-bands. The most-important parameters for a quantum well are the well width L_x and well height Φ_b . The potential barrier is obtained from the conduction-band and valence-band offsets (ΔE_C and ΔE_V). The solution for the wave function of the Schrödinger equation inside the well is:

$$\psi(x) = \sin\left(\frac{i\pi x}{L_x}\right) \quad (1.2.2)$$

where i is an integer. It should be noted that at the well boundaries, ψ is truly zero only when Φ_b is infinite. With finite Φ_b , carriers can “leak” out (by tunneling) of the well with finite probability. The pinning of nodes at the well boundaries leads to the quantization of sub-bands; with respect to the band edges, each sub-band has a bottom energy of:

$$E_i = \frac{\hbar^2 \pi^2 i^2}{2m^* L_x^2} \quad (1.2.3)$$

These solutions do not take into account a finite barrier height. With L_x as a variable, a quantum well can only be loosely defined. The minimum requirements should be that the quantized energy $\hbar^2\pi^2/2m^*L_x^2$ is much larger than kT , and L_x is smaller than the mean free path and the de-Broglie wavelength $\lambda = h/(2m^*E)^{1/2}$. Since the continuous conduction band is now divided into sub-bands, carriers no longer reside on the band edges E_C or E_V but on these sub-bands only. In effect, the effective energy gap for interband transitions inside the quantum well becomes larger than the bulk E_g .

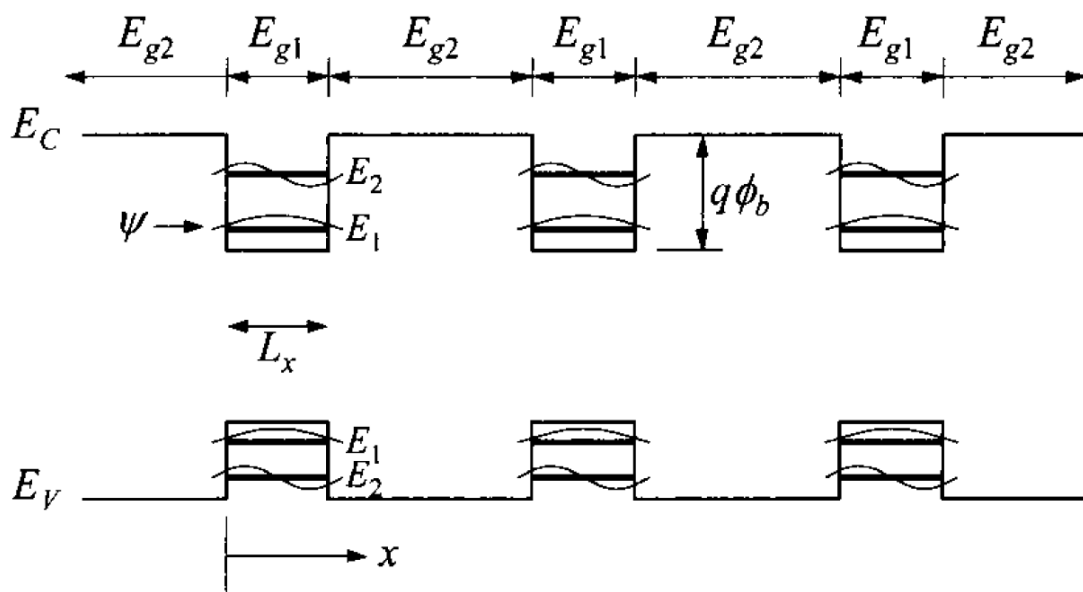


Figure 1.2.1 Energy-band diagrams for heterostructure (composition) multiple quantum wells [68].

1.2.1

Quantum Confined Stark Effect

An important effect present also in nitrides is the Quantum Confined Stark effect (QCSE). In principle, it reduces the transition probability between electron and hole states in a quantum well and also lowers the transition energy [9], [22], [77], [87], [97], [102], [103]. This systematically causes red-shifts. Whenever an otherwise unexpected or unexplained red shift is observed, when considering theoretical models and predictions made by interpolation between binary alloys, the QCSE is a usual explanation.

As discussed in Chapter 1.1, there is a large polarisation field in GaN-based structures that lays in the c-direction as a result of the intrinsic spontaneous crystal polarisation and strain induced piezoelectric polarization fields. When the polarisation fields are suddenly changed (for example between the InGaN/GaN heterointerface) a large built-in electric field is induced, which has a strong influence on the confined energy states inside the quantum well (QW). The built-in electric field has two fundamental consequences on the optical properties of c-plane InGaN/GaN QWs. Firstly the electric field induces the quantum confined Stark effect (QCSE) that acts to reduce the confined energy states of the CB electrons and VB holes, reducing the overall recombination energy of the system [100]. For the second effect, it must be considered that the QW confinement potentials become tilted into triangular forms. This occurs as the electrons and holes are pushed in opposite directions by the electric field due to their relative charges (Fig. 1.2.1.1). The spatial separation of the electrons and holes reduces the overall e-h wavefunction overlap and leads to a reduction in the oscillator strength. A reduction in oscillator strength decreases the recombination probability between the carriers, thus increasing the radiative recombination lifetime that consequently may result in an overall reduction of the internal quantum efficiency.

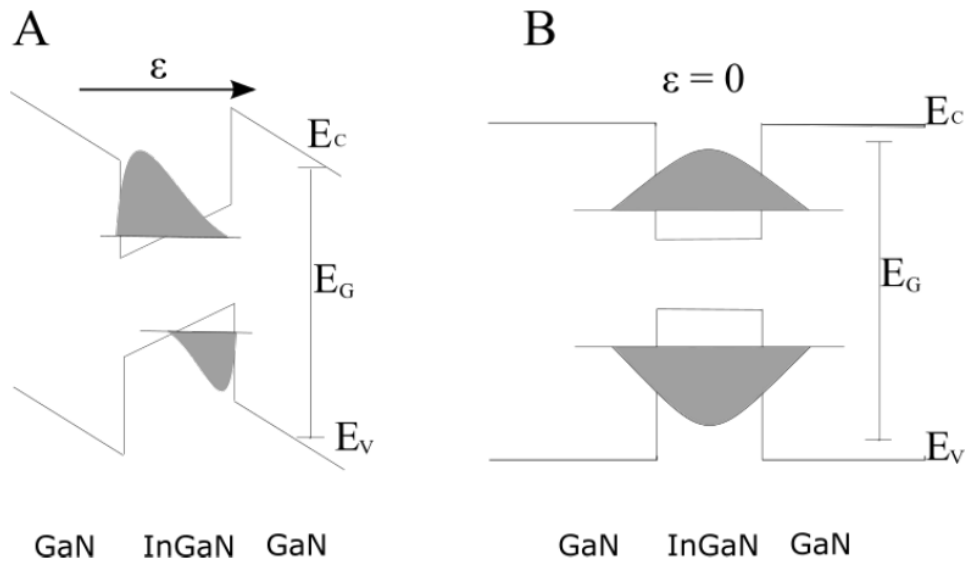


Figure 1.2.1.1 The confined electron and hole states for a typical c-plane QW (A) and non-polar QW (B). The built-in electric field in the c-plane QW reduces the overall recombination energy and the e-h wavefunction overlap by spatially separating the electrons and holes across the QW.

1.3

Growth Processes

1.3.1

Epitaxy

Epitaxy is the technique of deposition of crystalline overlayers on crystalline substrates. A few atomic layers are usually deposited to retain the lattice constant of the substrate thus straining the deposited layers to this lattice constant [104]-[108].

1.3.2

MOVPE growth

Compounds containing Aluminium are often difficult to grow by organo-metallic vapor-phase epitaxy (MOVPE) [105], [107]-[110] which is the usual epitaxial technique for the growth of the required layers during the fabrication of a LED. Aluminium is quite reactive and thus a *clean room*, as it is often termed, is a MOVPE requirement. Even minor leaks result in the degradation of Al-containing films [21].

1.3.3

Metal Contacts Technology

Metal contacts are a complex matter in many devices and such is the case in diodes. Particularly, metal-semiconductor interfaces may be a parasitic Schottky diode whereas an ohmic, low resistance behaviour is the ideal. Further considerations include adhesion, mechanical strength, and resistance to oxidation. Nickel, Titanium, and Gold metals are typically used in successive layers respectively, to achieve these highly sought properties [23], [70], [111]-[115].

1.4

Characterization Techniques

The characterization techniques utilized in this work are CVP, presented in Chapter 2.3.2, and modulation techniques (ER and EL spectroscopy), presented in Chapter 2.3.1. The CVP measurements and analysis were conducted at TU-Berlin and the spectroscopic measurements and analysis were conducted at NTU-Athens as already stated in the acknowledgements.

1.4.1

Optical characterization by ER and EL Spectroscopy

Quoting Fred H. Pollak, *"The modulation spectroscopy technique of electromodulation (EM) is a major tool for the study and characterization of a number of semiconductor surfaces/interfaces and also for the evaluation of process-induced damage at surfaces."* [116]. Modulation Spectroscopy is a unique optical characterization technique [18], [19], [35], [36], [77], [90], [103], [117]-[126], that can detect experimentally the derivative of the dielectric function. The sharp-edge lineshape of the PR and ER spectra results in accurate determination of the semiconductor band gap.

The process of luminescence requires a non-equilibrium carrier concentration in the electronic bands or in the electronic states of a defect structure. If the non-equilibrium is obtained by irradiation with light the radiative recombination is called photoluminescence, if it is obtained electrically, for instance, by forward biasing a p-n junction, it is called electroluminescence. Another thermodynamically interesting phenomenon originates from an interaction between excitons in semiconductors. Excitons exhibit a luminescence close to the band gap energy [127].

1.4.2

Electrical characterization by Capacitance-Voltage Profiling

Capacitance-Voltage Profiling (CVP) is a technique readily available that requires experience in the interpretation of the directly measured properties of current and voltage versus time [13], [24], [30], [34] [68], [71], [91]-[94], [106], [113], [128]-[142], as explained in Chapter 2.3.2.3 and moderately expensive equipment. Its principles and engineering required for a proper setup are, even surely delicate and non trivial, far less complicated compared to other techniques as Modulation spectroscopy, as discussed in Chapters 2.3.2 and 2.3.1 respectively. In principle, one measures the capacitance of a diode in reverse bias which is caused by the depletion region width [68]. The input signal is an AC voltage superimposed on a DC bias. The AC signal is necessary because the capacitance is a property which, in principle, can electrically only be calculated through its frequency, in particular through its impedance, or alternately through time, in particular through its discharge evaluating the time constant of the circuit response.

2

Experiment

2.1

Samples & layer structures

2.1.1

Growth methods

The growth technique used for the samples of this work was metal organic phase epitaxy (MOVPE) [105], [107]-[110], on (0001) wurtzite c-plane sapphire substrates, as stated in Chapter 2.1.1, using the appropriate intermediate layers, as explained in Chapter 2.1.2. Subsequently to the crystal growth, the samples were etched using mechanical or chemical etching and metal contacts were fabricated using a combination of metals, as described in Chapter 2.2.1.

2.1.1.1

MOVPE Calibration Samples

Before any sample is grown, a series of calibration samples using simplified structures is grown to accurately estimate the growth speed. Both growth rates and sample stoichiometry are determined using XRD and linearly interpolating between the InN, AlN, and GaN peaks. The calibration samples consist of a semiconductor layer (GaN, InGaN, InAlN) of the material under investigation on an appropriate substrate.

2.1.2

Investigated Samples

The samples investigated in this work consisted of a large number of diodes (ca. 2000) created by etching and metal contact fabrication, after all the crystal layers were grown, on quarter-wafer shaped sapphire substrates. The basic structure was a GaN PIN diode with an intrinsic GaN layer sandwiched between p- and n-doped GaN layers in the form of a quantum well (QW) structure. The only intended difference between samples was the incorporation of an intrinsic $\text{In}_x\text{Ga}_{1-x}\text{N}$ or $\text{In}_x\text{Al}_{1-x}\text{N}$ QW between 2 intrinsic GaN QWs in the form of a double heterostructure (DHS). In Fig. 2.1.2.1, a side-view and a top-view of the PIN diodes is presented whereas, in Fig. 2.1.2.2, a 3D view demonstrates the geometry of the structure. In Figs. 2.1.2.3-7, a full top-view photo shows the usefulness of p-contacts mapping in rows and columns in order to reproduce previous measurements or perform more thorough investigation on each individual diode. In the same Figures, the part which was later separated from the quarter wafer sample in order to examine the nature of the devices through Electroluminescence (EL) and modulated Electroreflectance (ER) measurements is marked by a rectangular.

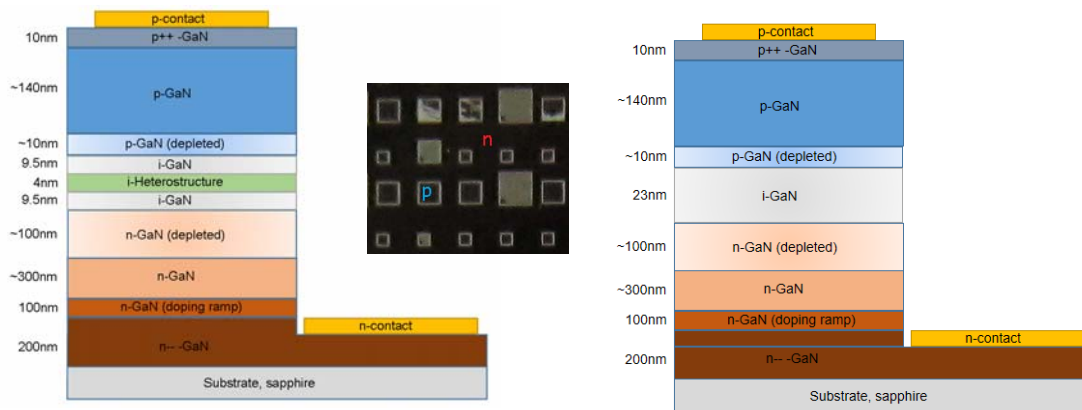


Figure 2.1.2.1 Side-view schematic and top-view photo of PIN diodes.

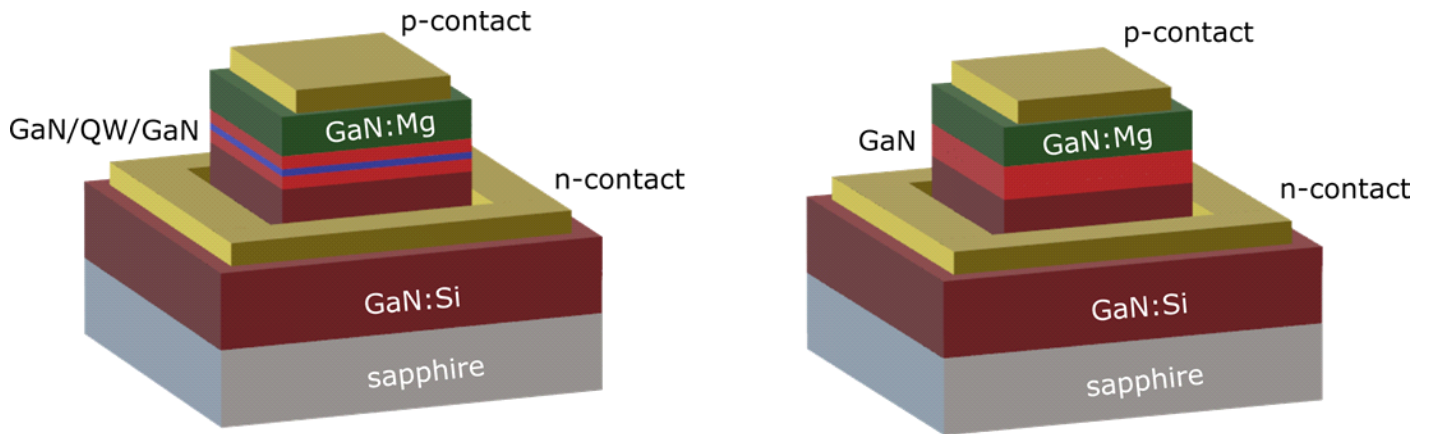


Fig. 2.1.2.2 3D schematic representation of the PIN diodes

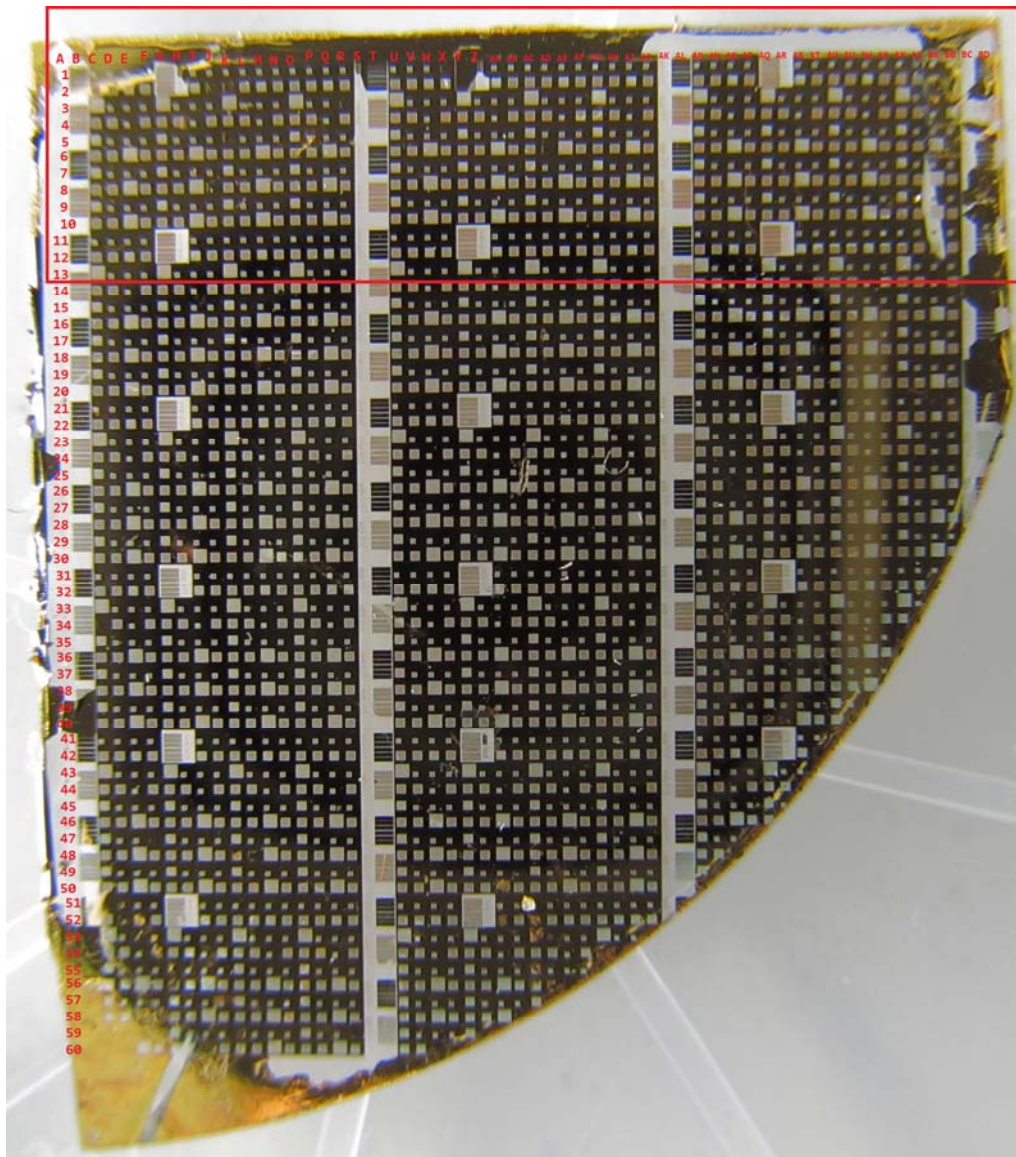


Figure 2.1.2.3 The $\text{In}_{0.055}\text{Ga}_{0.945}\text{N}/\text{GaN}$ (DHS) PIN diodes (MD9327).

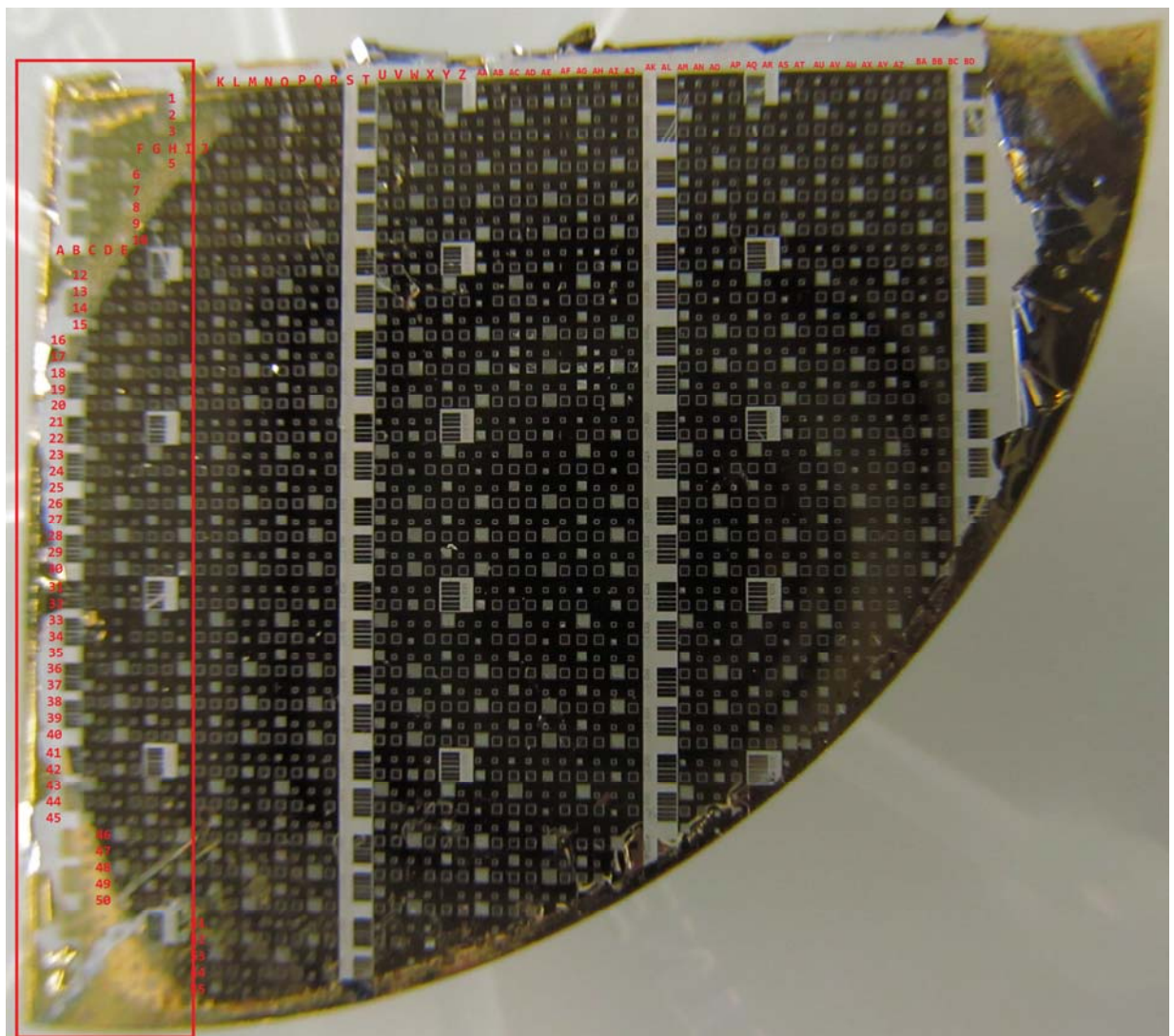


Figure 2.1.2.4 The GaN/GaN (no DHS) PIN diodes (MD9328).

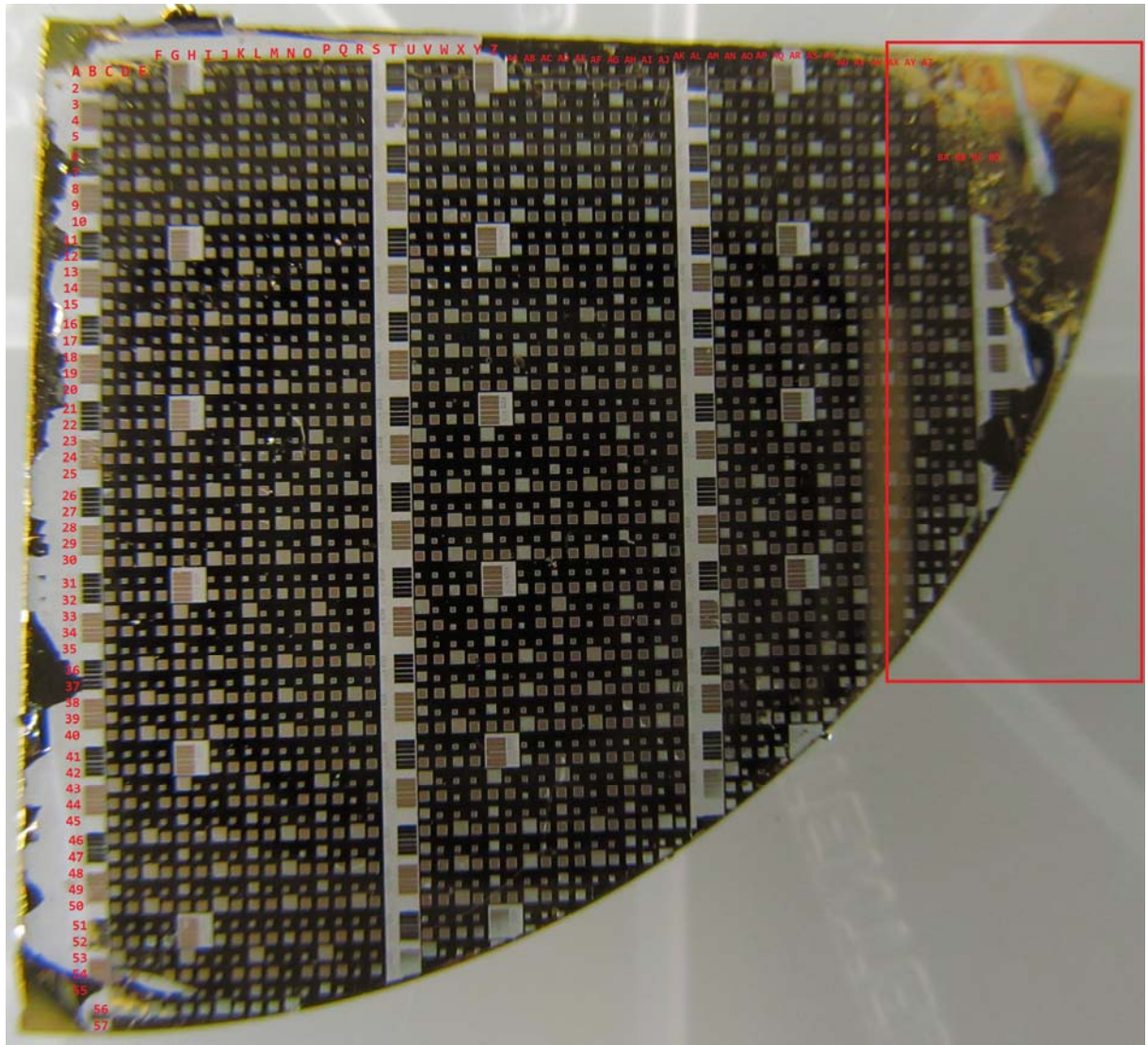


Figure 2.1.2.5 The $\text{In}_{0.17}\text{Al}_{0.83}\text{N}/\text{GaN}$ (DHS) PIN diodes (MD9330).

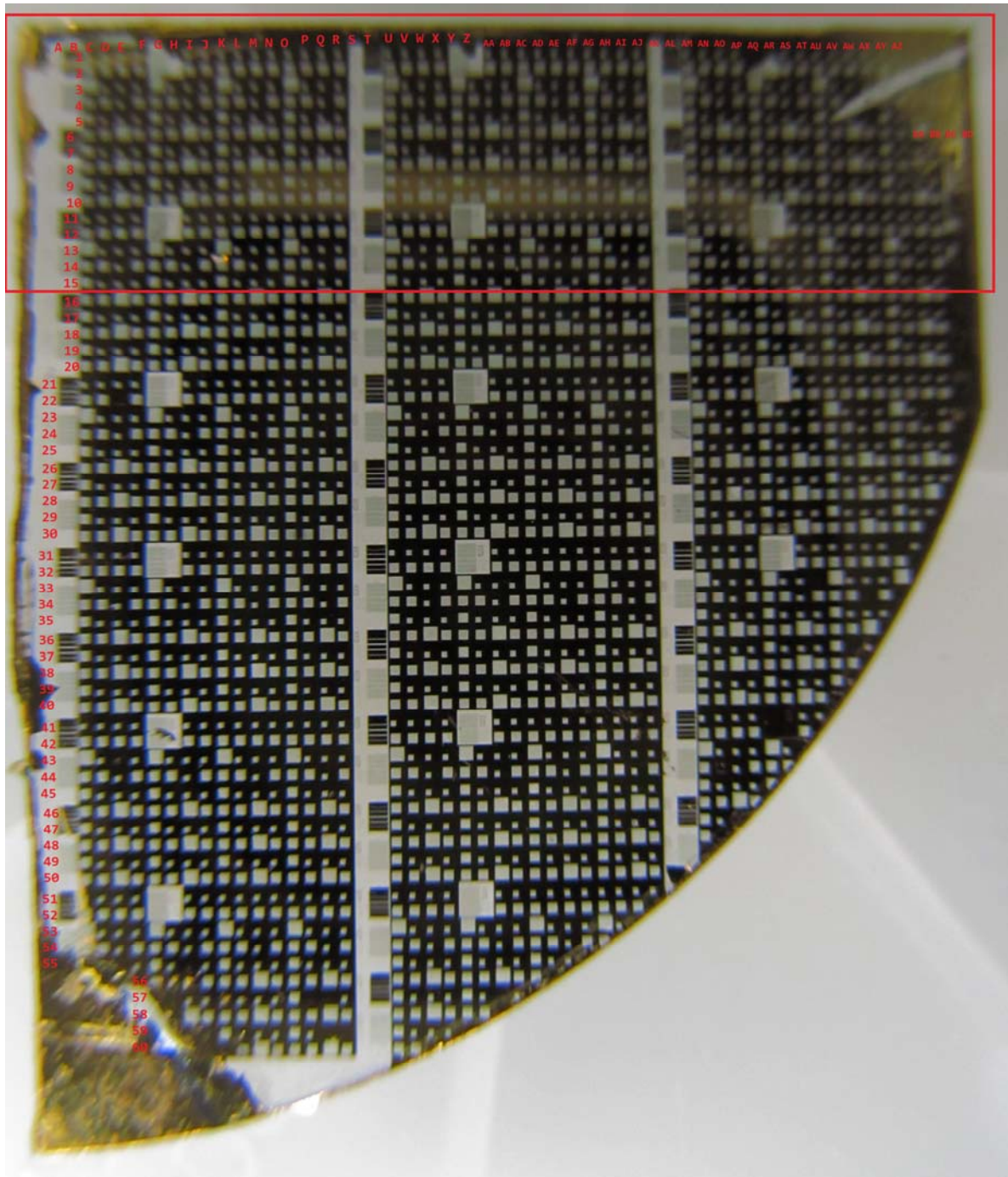


Figure 2.1.2.6 The $\text{In}_{0.20}\text{Al}_{0.80}\text{N}/\text{GaN}$ (DHS) PIN diodes (MD9331).

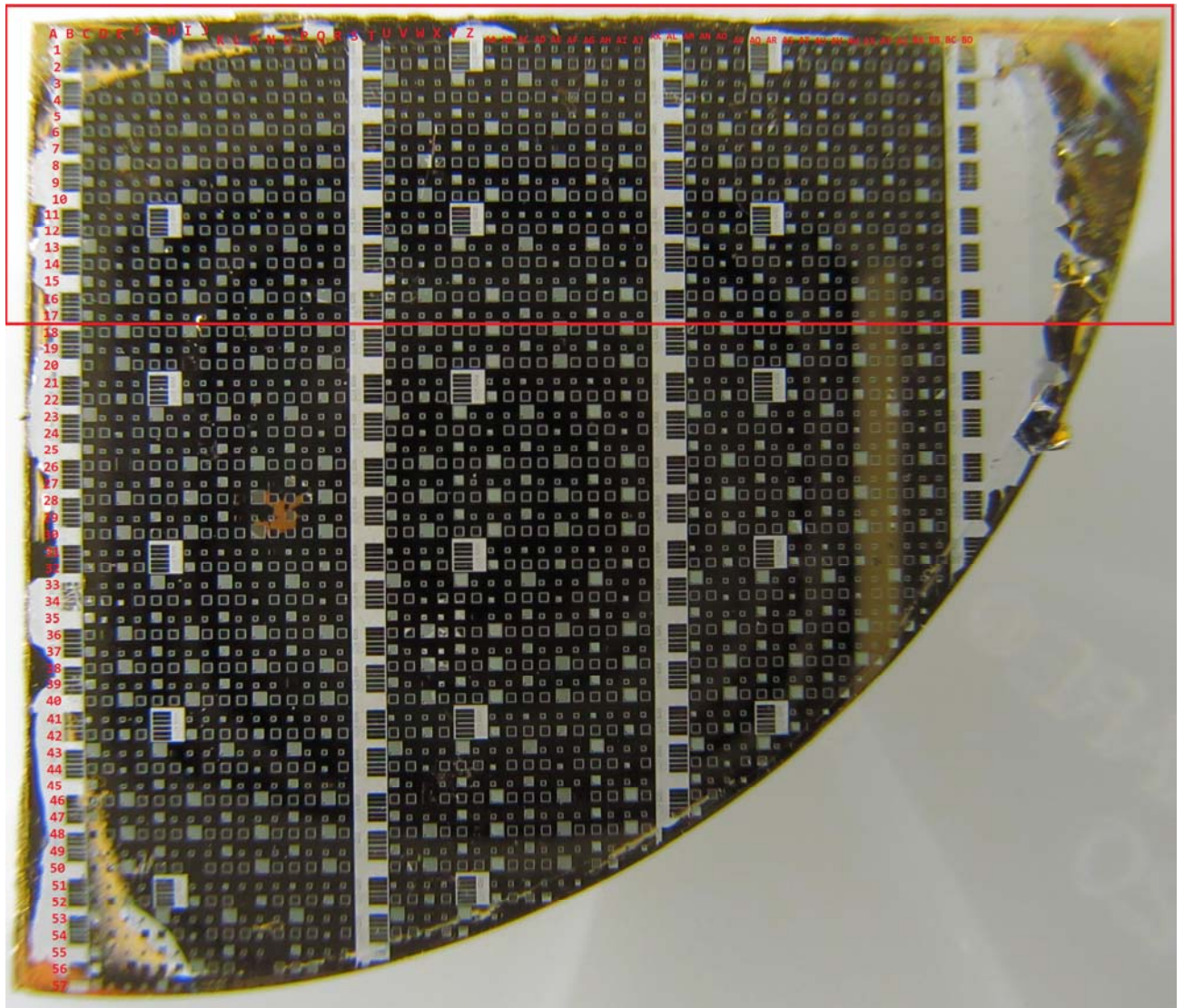


Figure 2.1.2.7 The $\text{In}_{0.22}\text{Al}_{0.78}\text{N}/\text{GaN}$ (DHS) PIN diodes (MD9332).

2.1.3

Sample structure (TEM, XRD)

The thickness for the DHS intermediate layer of the $\text{In}_{0.17}\text{Al}_{0.83}\text{N}/\text{GaN}$ (DHS) PIN diodes was determined using HRTEM. For all the other samples, thicknesses were determined from the XRD measurements performed.

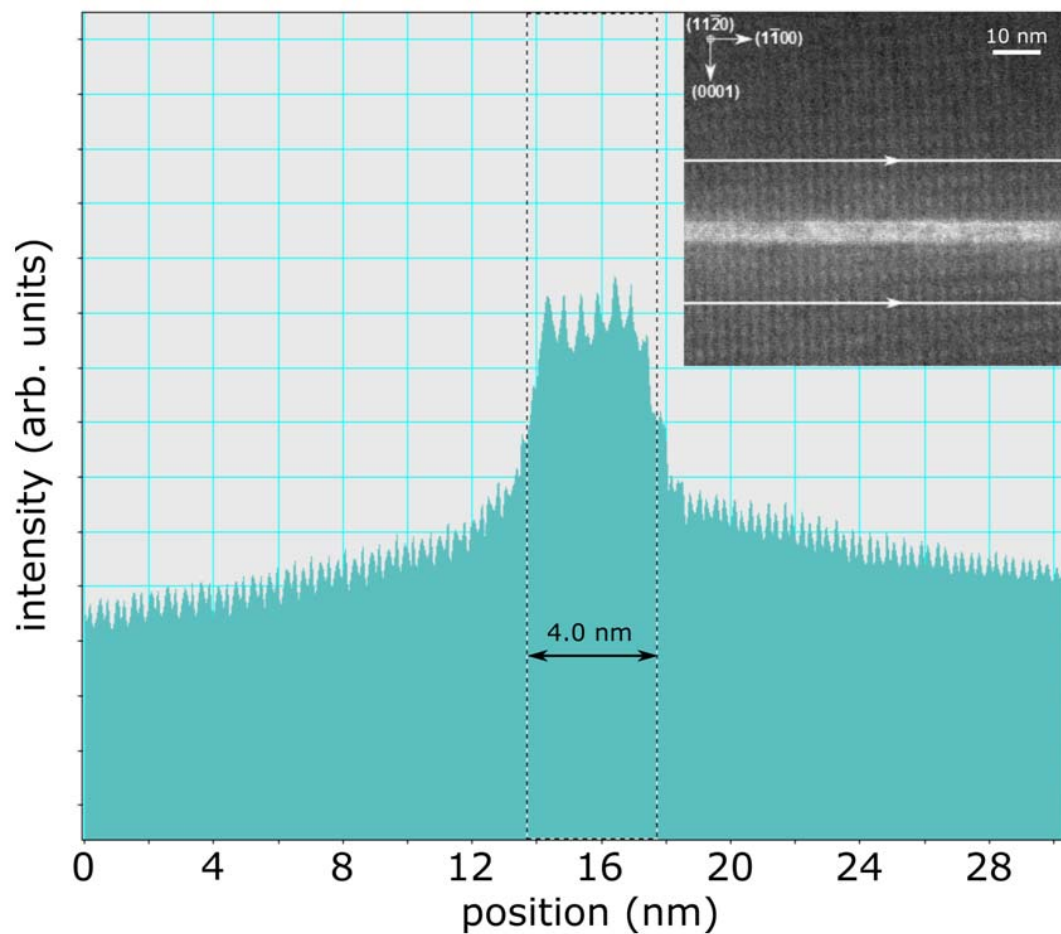


Figure 2.1.3.1 HRTEM image of the $\text{In}_{0.17}\text{Al}_{0.83}\text{N}$ layer in GaN matrix. The Linescan is along the growth direction ($1\bar{1}00$).

2.2

Contacts

2.2.1

Selected metals

Following the epitaxial heterostructure growth, PIN diodes were fabricated by standard lithography and metallization techniques using a Ni/Au (bottom/top) layer sequence for the p-contacts and Ti/Al/Ti/Au for the n-contacts. The CVP measurements were performed using 200x200 μm^2 p-contacts.

2.2.2

Parasitic Schottky Contacts

Even though efforts are generally made to have ohmic contacts, it is a common case that a parasitic Schottky contact behaviour is observed for at least one of the 2 contact types on either the p- or n-side of the sample. Such behaviour is examined on the TLM (rectangular shape) structures present in the sample. It is theoretically proven, in Chapter 3.2.5, that they should pose no obstructing factor for the CVP measurement as long as their resistance is well below the resistance of the diode in reverse bias; this was the case for every sample in this work.

2.3

Instrumentation setup & Measurement Procedure

For the experiments, in this part, the instrumentation of the laboratory for Material Growth and Optical Characterization, at the NTUA, was used.

2.3.1

Optical characterization by Modulation Spectroscopy

The ER signal can be expressed as [116]:

$$\frac{\Delta R}{R} = a(\varepsilon_1, \varepsilon_2) \cdot \Delta\varepsilon_1 + b(\varepsilon_1, \varepsilon_2) \cdot \Delta\varepsilon_2 \quad (2.3.1.1)$$

where ΔR is an AC signal and R a DC signal, with the AC signal amplitude being many orders of magnitude less than the DC signal, and the a and b are the Seraphin coefficients. The ε variables are the real and imaginary parts respectively of the unperturbed complex dielectric function and the $\Delta\varepsilon$ variables represent the change of the ε variables due to the external perturbation.

In Ref. [116] and also in Refs. [143] and [144], the ER signal is also expressed as:

$$\frac{\Delta R}{R} = C \cdot \left(\frac{h}{2 \cdot \pi} \cdot \Theta \right)^3 \cdot \text{Re} \left[e^{i \cdot \phi} \cdot (E - E_g + i\Gamma)^{-m} \right] \quad (2.3.1.2)$$

where C is an arbitrary real constant, h is Planck's constant, and ϕ is a phase angle that accounts for the influence of non-uniform electric fields, interferences, and electron-hole interaction effects. E is the energy of the photon, E_g is the band gap of the semiconductor, Γ is the broadening parameter, and m depends on the dimension of the critical point (CP) [118], being 2.5 for a 3-dimensional (3D), 3 for a two-dimensional (2D), 3.5 for an one-dimensional (1D) CP, and 2 for excitonic transitions [117].

A fact that has to be taken into account is that the actual signal is always a superposition of signals for all the band gaps and all the dimensions of the critical points [145]. What is measured, in the simplest case of a single band gap and a single CP dimension, is described by Eq. (2.3.1.3):

$$\frac{\Delta R}{R} = C \cdot \left(\frac{h}{2 \cdot \pi} \cdot \Theta \right)^3 \cdot \text{Re} \left[e^{i \cdot \phi} \cdot (E - E_g + i \cdot \Gamma)^{-m} \right] = ER_{\text{signal}} C_1 \quad (2.3.1.3)$$

where $\Theta \cdot h/(2\pi)$ is the electro-optical energy, ER_{signal} is the measured ER signal, and C_1 is an arbitrary constant. Omitting the constants, the signal of interest will be denoted as S:

$$S = \text{Re} \left[e^{i \cdot \phi} \cdot (E - E_g + i \cdot \Gamma)^{-m} \right] \quad (2.3.1.4)$$

which can be rewritten in the form of:

$$S = \left(|E - E_g + i \cdot \Gamma| \right)^{-m} \cdot \cos \left(\phi - m \cdot \arg(E - E_g + i \cdot \Gamma) \right) \quad (2.3.1.5)$$

and consequently in the form of:

$$S = \left[(E - E_g)^2 + \Gamma^2 \right]^{-\frac{m}{2}} \cdot \cos \left[\phi - m \cdot \arctan \left[\frac{\Gamma}{(E - E_g)} \right] \right] \quad (2.3.1.6)$$

consisting of two parts which will be denoted as the Argument (or A in abbreviated form) and the Absolute parts.

$$\text{Absolute}_{\text{part}} = \left[(E - E_g)^2 + \Gamma^2 \right]^{-\frac{m}{2}} \quad (2.3.1.7)$$

$$\text{Argument}_{\text{part}} = \cos \left(\phi - m \cdot \arctan \left(\frac{\Gamma}{(E - E_g)} \right) \right) \quad (2.3.1.8)$$

Typical plots of Eq. (2.3.1.7) deduced from the theoretical model by inserting the GaN values of $E_g=3.4\text{eV}$ and $\Gamma=15\text{meV}$ are presented in Fig. 2.3.1.1:

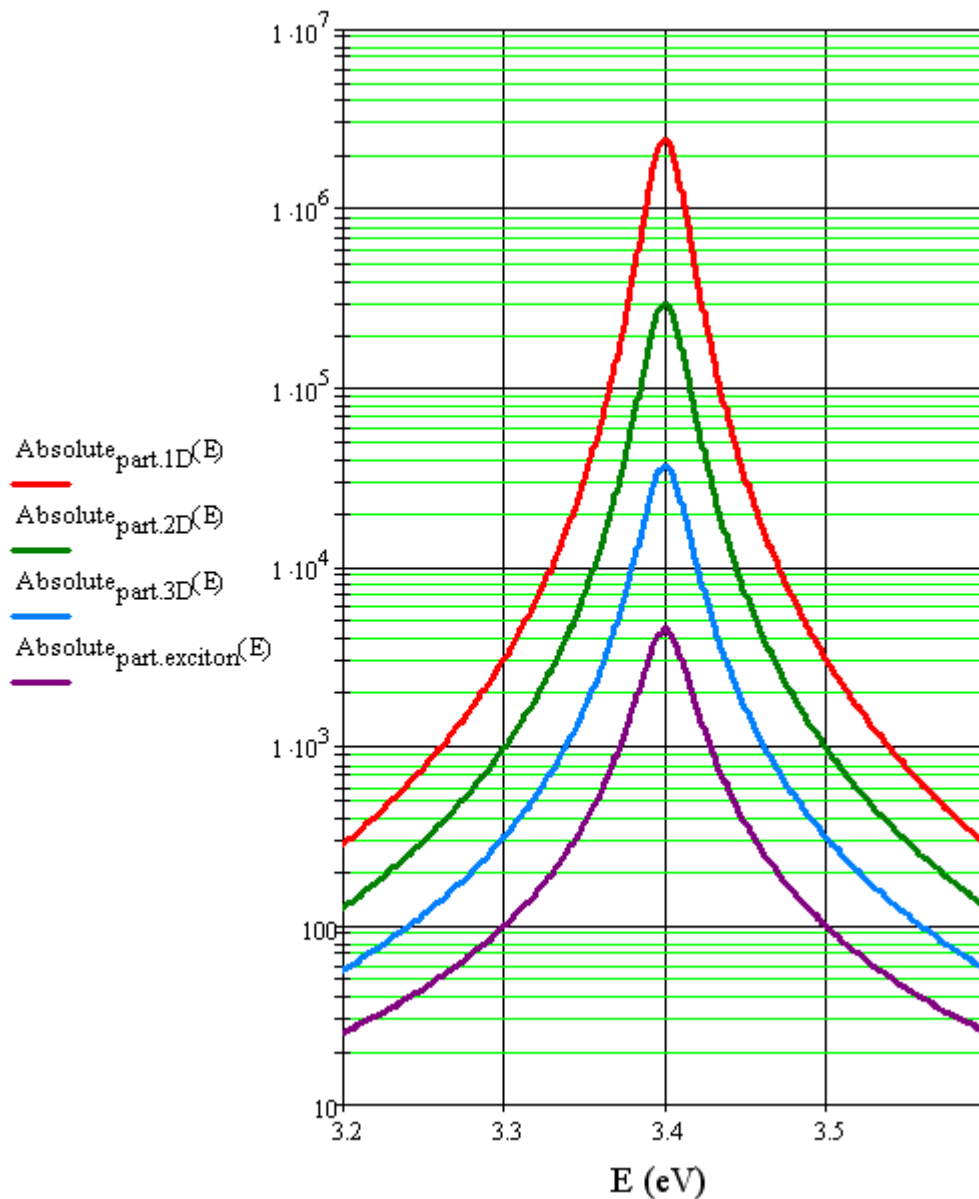


Figure 2.3.1.1 Theoretically calculated (absolute) part of the ER signal for 1D (red), 2D (green), 3D (blue) critical points and excitonic response (purple) using Eq. (2.3.1.7).

It is noted, that the absolute part is the one that causes the high values in the ER graphs, whereas the argument part is the one that causes the alternation of those high values. The absolute part is a function with maximum at E_g and is independent of φ . The argument part is a function with sharp alternating peaks, almost symmetrical at the vicinity of E_g . It also has to be noted, that the maximum and minimum peaks of the signal are in almost every case close to E_g , but not exactly E_g .

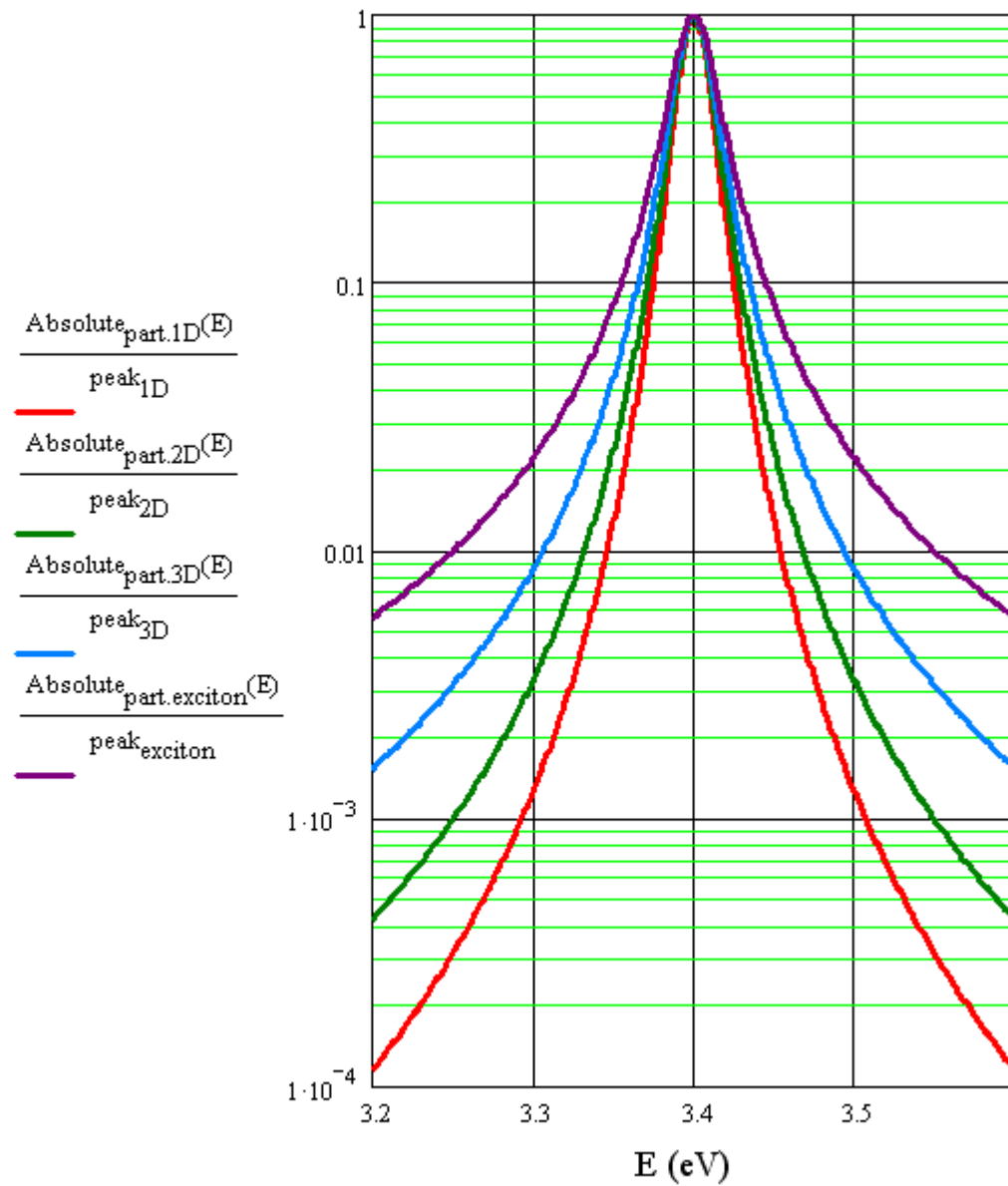


Figure 2.3.1.2

Theoretically calculated normalized (absolute) part of the ER signal for 1D (red), 2D (green), 3D (blue) critical points and excitonic response (purple) using Eq. (2.3.1.7).

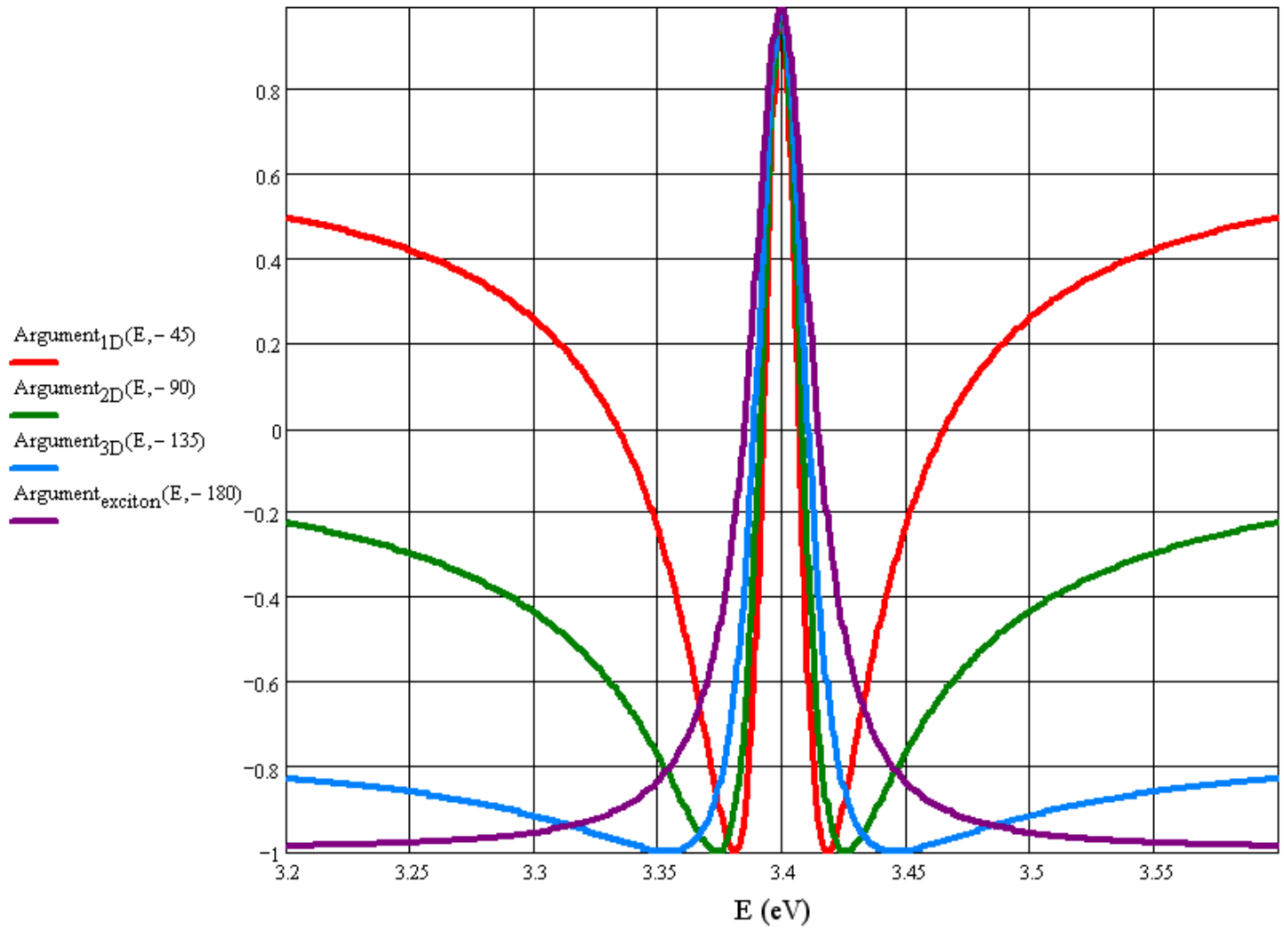


Figure 2.3.1.3

Comparison of the theoretically calculated (argument) part of the ER signal for 1D (red), 2D (green), and 3D (blue) critical points and excitonic response (purple) using Eq. (2.3.1.8) and -45, -90, -135 and -180 degrees for the phase angle, respectively.

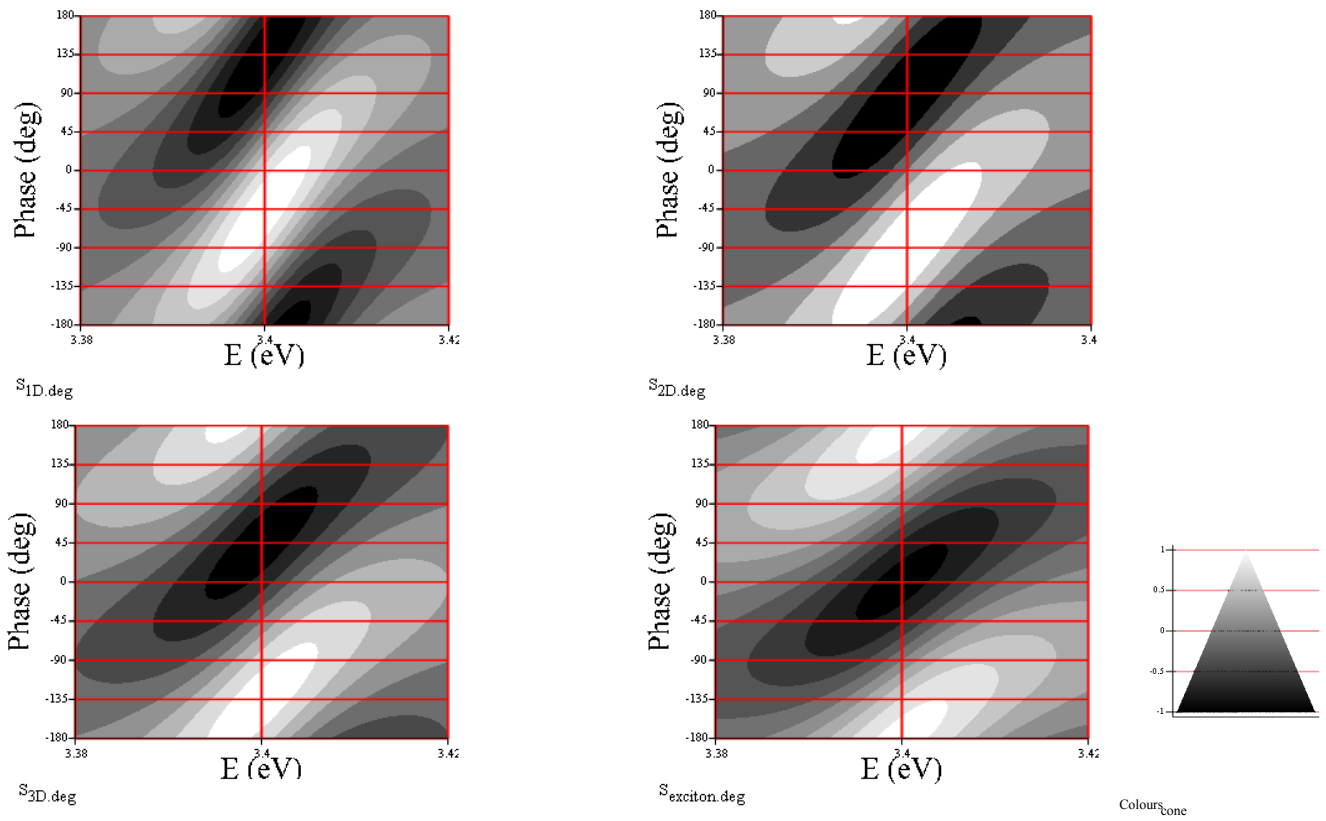


Figure 2.3.1.4

3D contour plots of $C \cdot \Delta R/R$, Eq. (2.3.1.6), for every possible dimension (1D, 2D, 3D), of the CP, and exciton-related response, as well as the colour legend in the form of a 3D-side-view cone as a separate graph.

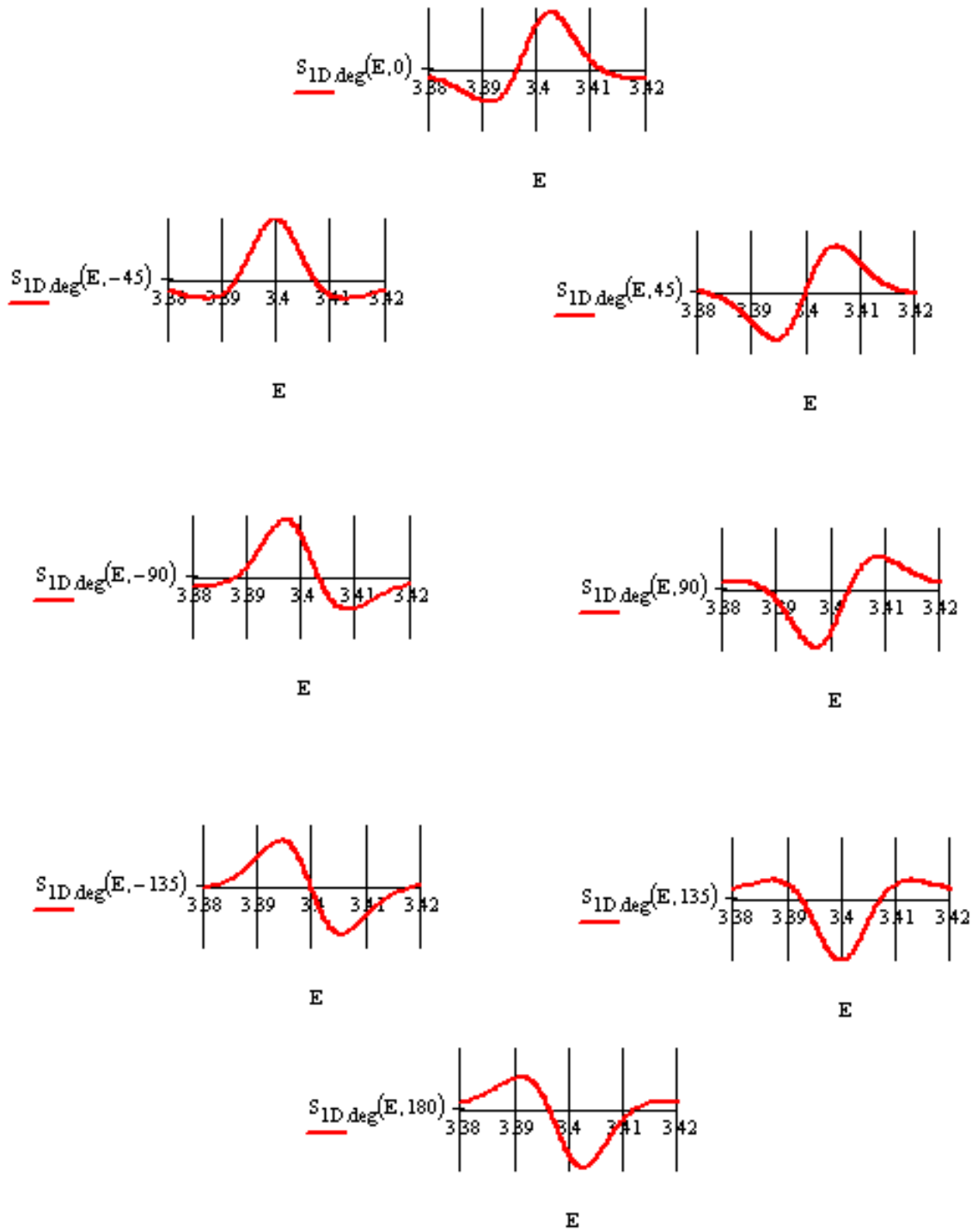


Figure 2.3.1.5 2D representation of the 3D graph of $C \cdot \Delta R/R$, Eq. (2.3.1.6), for 1D CP and successively increasing angles of the phase ϕ .

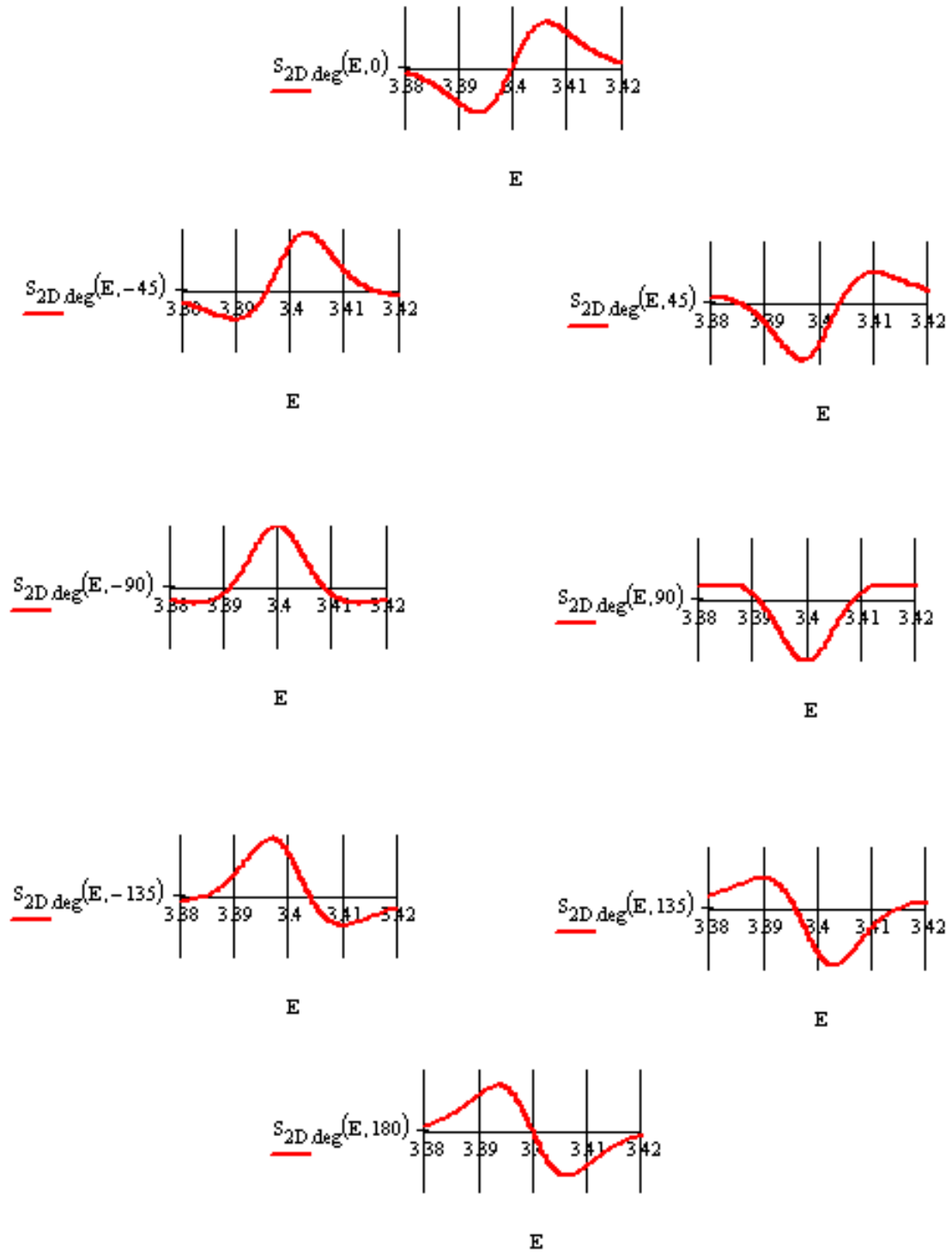


Figure 2.3.1.6 2D representation of the 3D graph of $C \cdot \Delta R/R$, Eq. (2.3.1.6), for 2D CP and successively increasing angles of the phase ϕ .

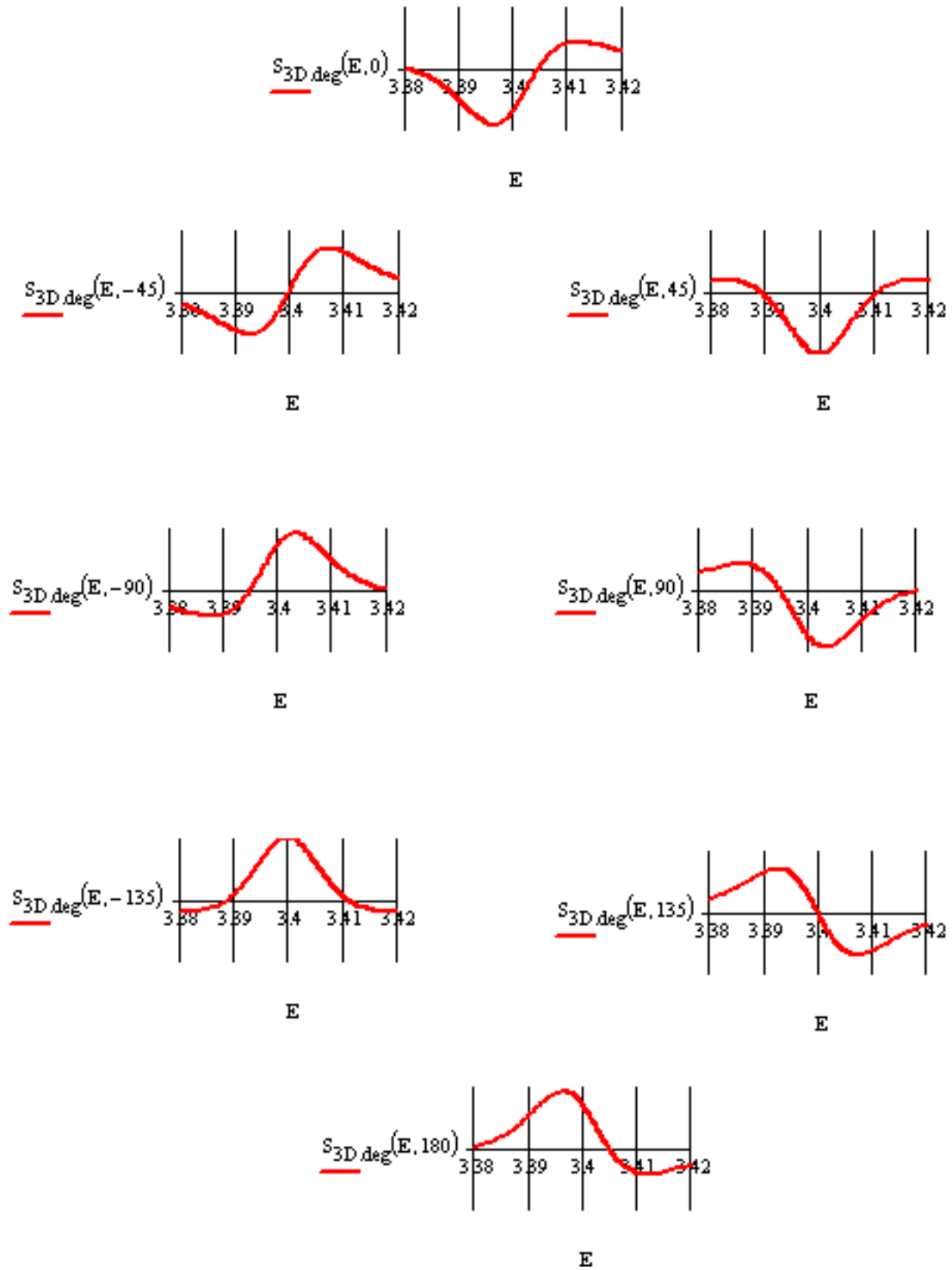


Figure 2.3.1.7 2D representation of the 3D graph of $C \cdot \Delta R / R$, Eq. (2.3.1.6), for 3D CP and successively increasing angles of the phase ϕ .

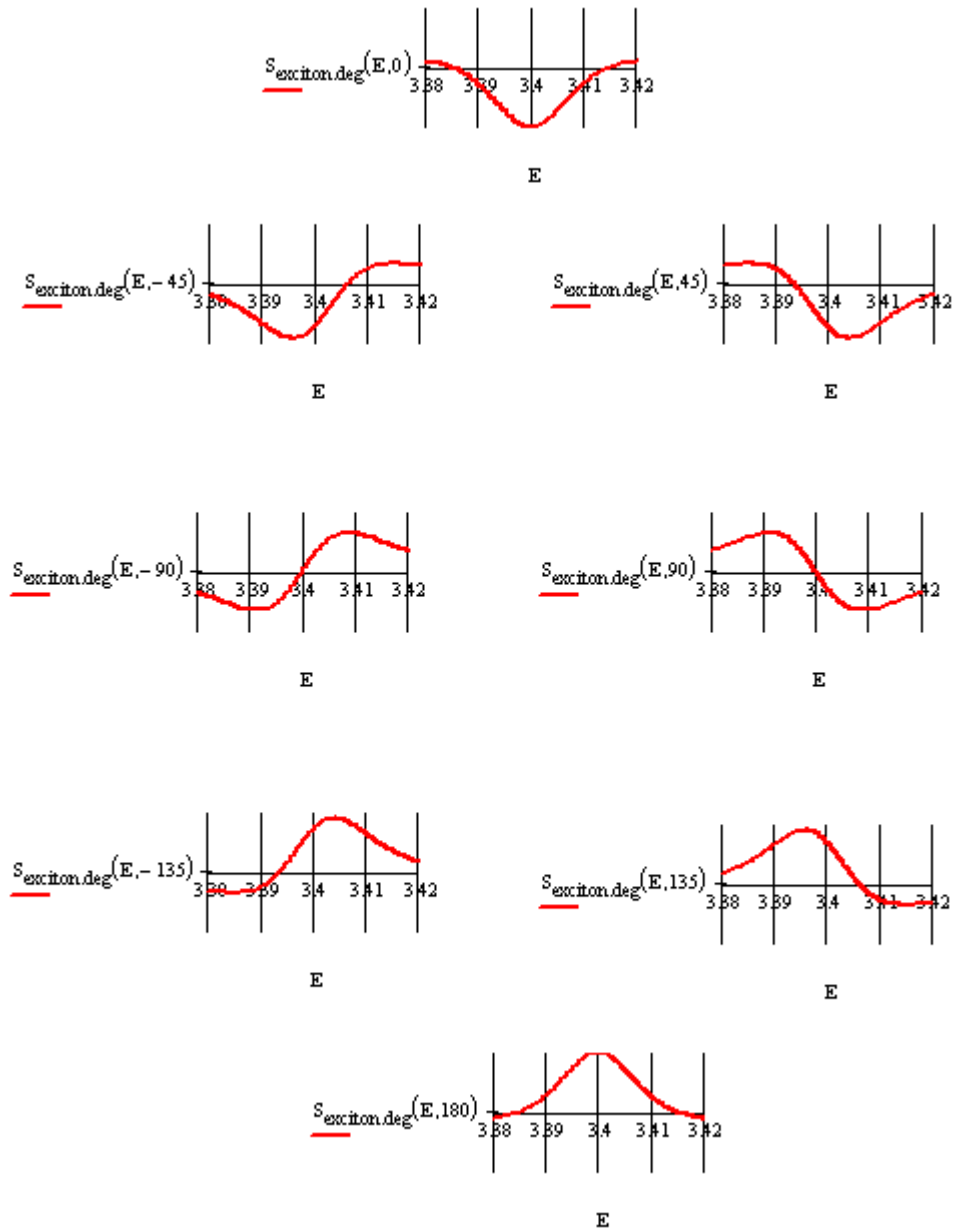


Figure 2.3.1.8 2D representation of the 3D graph of $C \cdot \Delta R/R$, Eq. (2.3.1.6), for the excitonic response and successively increasing angles of the phase φ .

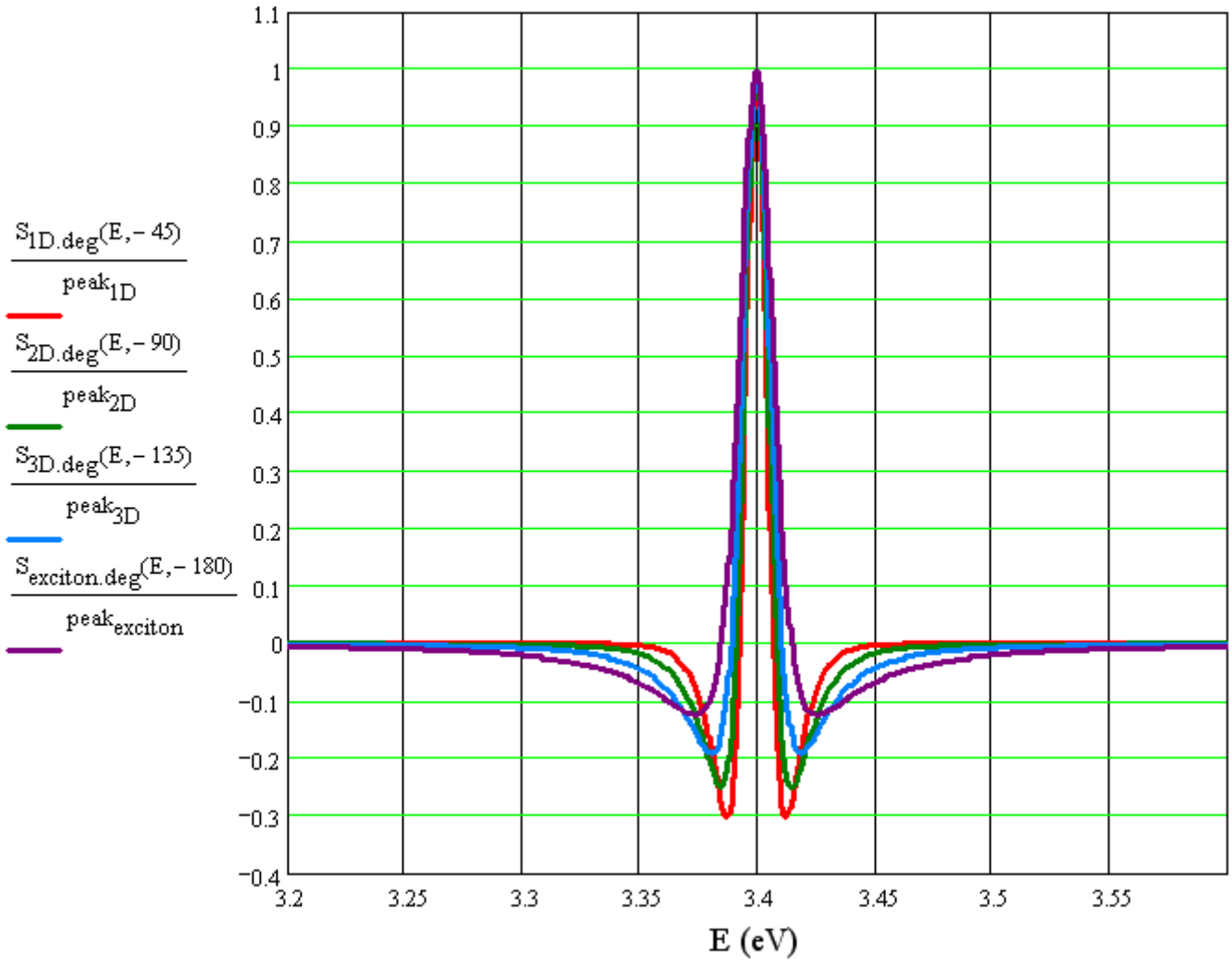


Figure 2.3.1.9

Comparison of the theoretically calculated normalized ER signal ($C \cdot \Delta R/R$) for 1D (red), 2D (green), and 3D (blue) critical points and excitonic response (purple) using Eq. (2.3.1.6) and -45, -90, -135 and -180 degrees for the phase angle, respectively.

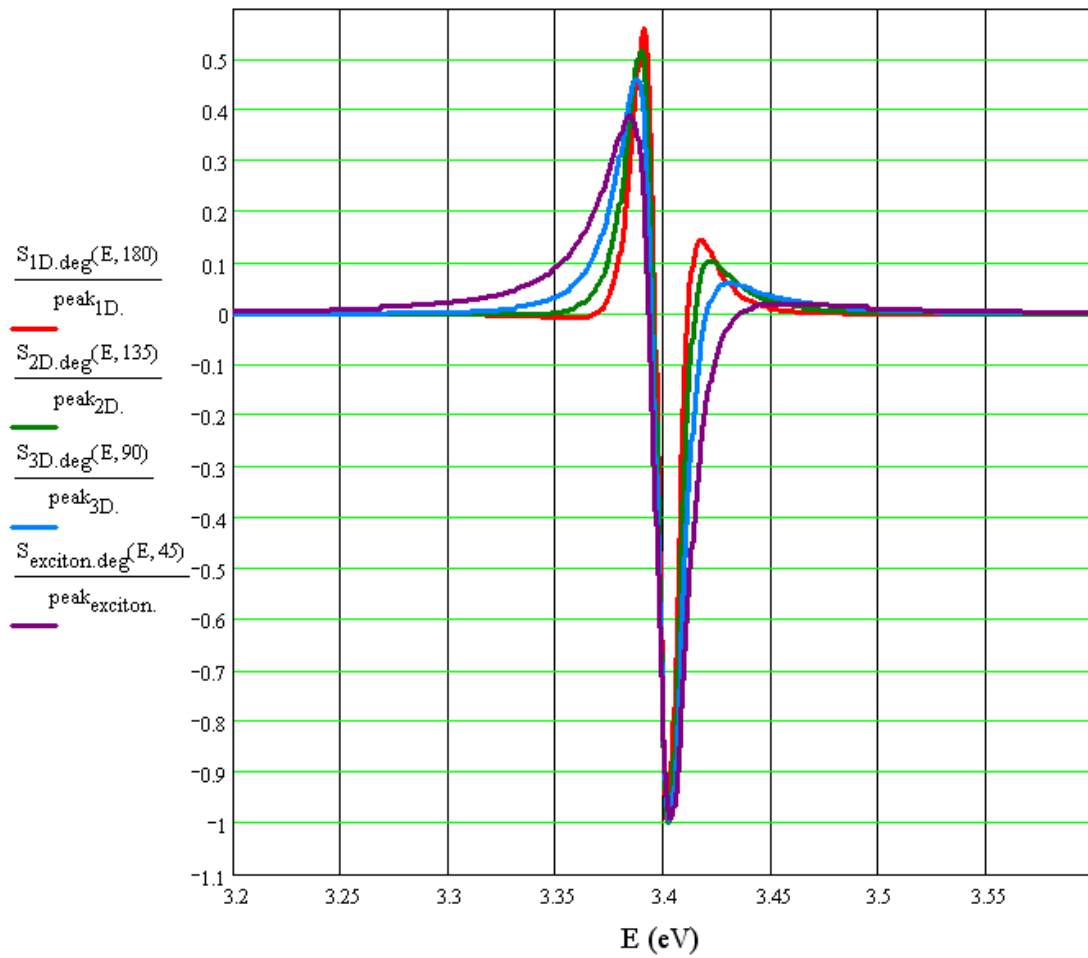


Figure 2.3.1.10 Comparison of the theoretically calculated normalized ER signal ($C \cdot \Delta R/R$) for 1D (red), 2D (green), and 3D (blue) critical points and excitonic response (purple) using Eq. (2.3.1.6) and 180, 135, 90 and 45 degrees for the phase angle, respectively.

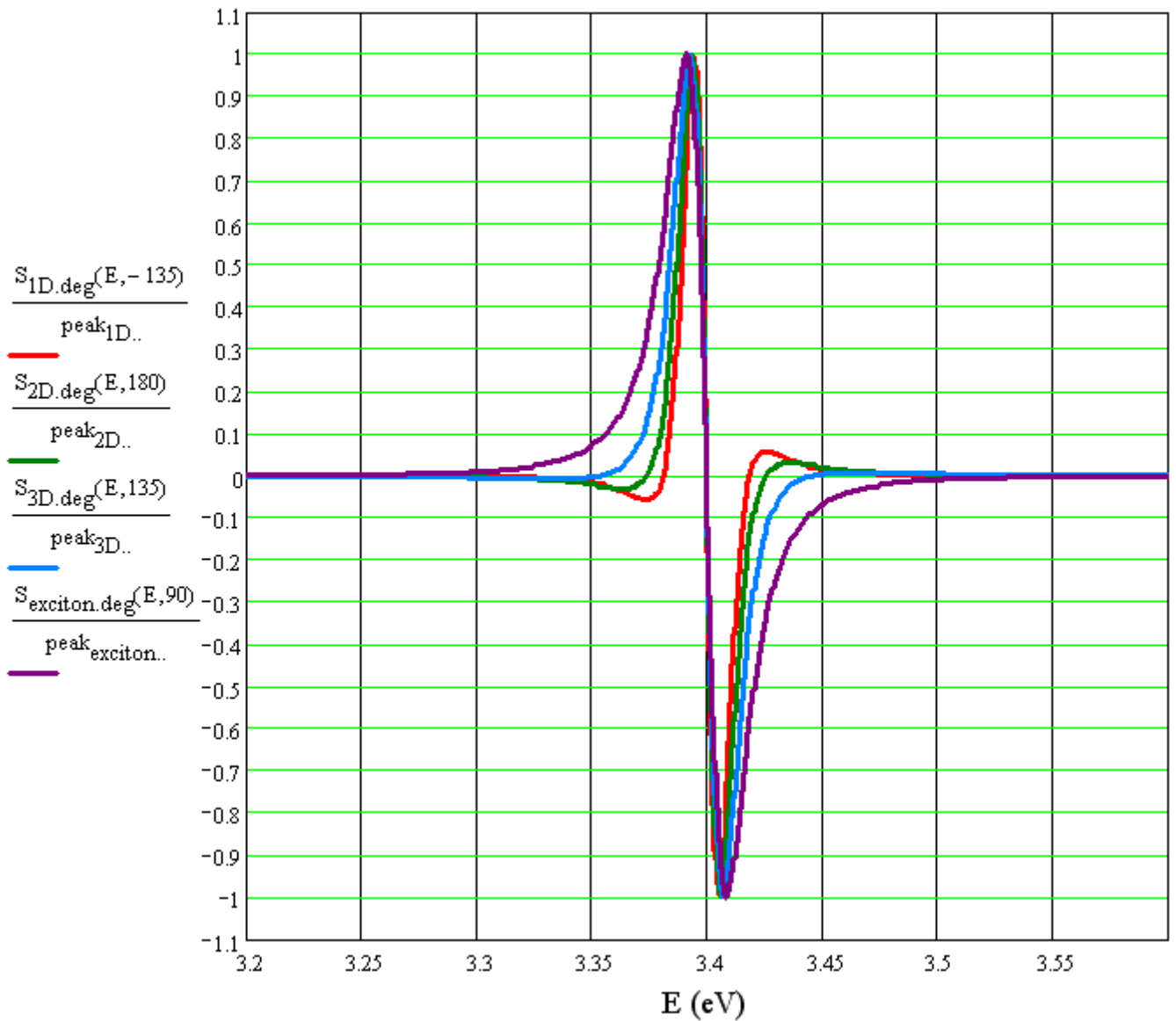


Figure 2.3.1.11 Comparison of the theoretically calculated normalized ER signal ($C \cdot \Delta R/R$) for 1D (red), 2D (green), and 3D (blue) critical points and excitonic response (purple) using Eq. (2.3.1.6) and -135, 180, 135 and 90 degrees for the phase angle, respectively.

2.3.1.1

Modulation Spectrometer (ER & PR)

The self-built experimental setup can be operated in the NUV-VIS-NIR range (180-1300 nm) in two different modes:

- 1) Modulation spectrometer for photo- and electroreflectance measurements and
- 2) Luminescence spectrometer for photo- and electroluminescence measurements.

The setup includes two lasers (Ar⁺-laser and Kr⁺-laser) utilized in photoreflectance and photoluminescence experiments. In Chapter 2.3.1.2, a detailed description of this setup is given.

2.3.1.2

ER instrumentation setup

In Fig. 2.3.1.2.1, a block diagram of the instrumentation setup is shown. The green and the black arrows denote light paths and electrical connections, respectively.

In electroreflectance experiments, the sample is perturbed by a pulsed electrical signal which can be square, triangle or sinus, provided by a function generator (Thurlby-Thander TG215, 2 MHz), thus exciting it and slightly changing its reflectance characteristics.

The light source is either a Tungsten Halogen (75 or 100 W) or a Xenon arc-lamp (XBO lamp, Oriel 6263, 75 W), depending on the scanned wavelength region (the halogen lamp used for VIS/NIR and the Xenon lamp for NUV/VIS). The incident light beam is monochromated (spectrally analyzed) by a first monochromator (CVI DK240 1/4 m Monochromator) and focused on the sample (on the area between its electrical contacts) by a focusing lens. The reflected light beam is focused on the entrance slit of a second monochromator (SPEX 1704 1 m Monochromator), filtered, and detected by a Si diode (or alternately an InGaAs diode) detector. The detector converts light to an electrical signal (a DC signal with a superimposed small AC signal). In particular, the reflectance is converted to a DC signal (R) and the reflectance-changes to a small AC signal (ΔR), which is superimposed to R . The reflectance (R) and the modulated reflectance (ΔR) signals are converted by an analog-to-digital converter (ADC card) and driven to PC for further processing, acquisition, and visualization. The R signal can be measured separately by a Multimeter (Mastech MY64). The modulated signal ΔR is filtered by a low-pass passive filter, which cuts out noise above 40kHz, and driven to a Lock-in amplifier (Stanford Research Systems SR530). It is then further filtered by a band-pass filter integrated into the Lock-in amplifier, which allows only the fundamental frequency of the reference signal to pass. In ER experiments, both the modulation and the reference signal are provided by a function generator. The modulation signal can be a

sinus, a triangle or a square pulse with an offset or not. The reference signal is a square pulse of the same fundamental frequency as the modulation signal. A typical Lock-in amplifier can amplify a signal 1000x smaller than the noise level. The amplified signal is driven to the appropriate ADC input. Following the analog-to-digital signal conversion, the $\Delta R/R$ ratio can be calculated for the selected photon wavelength at which the two monochromators are instantly set. The PC, except from calculating and monitoring the $\Delta R/R$ spectra in dependence of energy (eV), also controls the two monochromators that are wavelength-synchronized and advancing in 0.5nm intervals throughout the scanned region.

In series with the sample, a resistor less than one hundredth of the sample resistance may be placed in order to monitor the sample real-time current in a voltage divider setup. Thus, the sample and the resistor sharing the same current causes a voltage drop across the resistor. Consequently, by knowing the resistor value, this voltage can be converted into a current value. Most important, by monitoring the sample current in real-time, the experiment can be stopped, if the electrical contacts are displaced. The contact probes induce locally a compressive stress on the sample which may lead to small or large displacements, when the stress component parallel to the plane of the sample is smaller than the static friction. In this case, the load can become resistive or even an open or a short circuit.

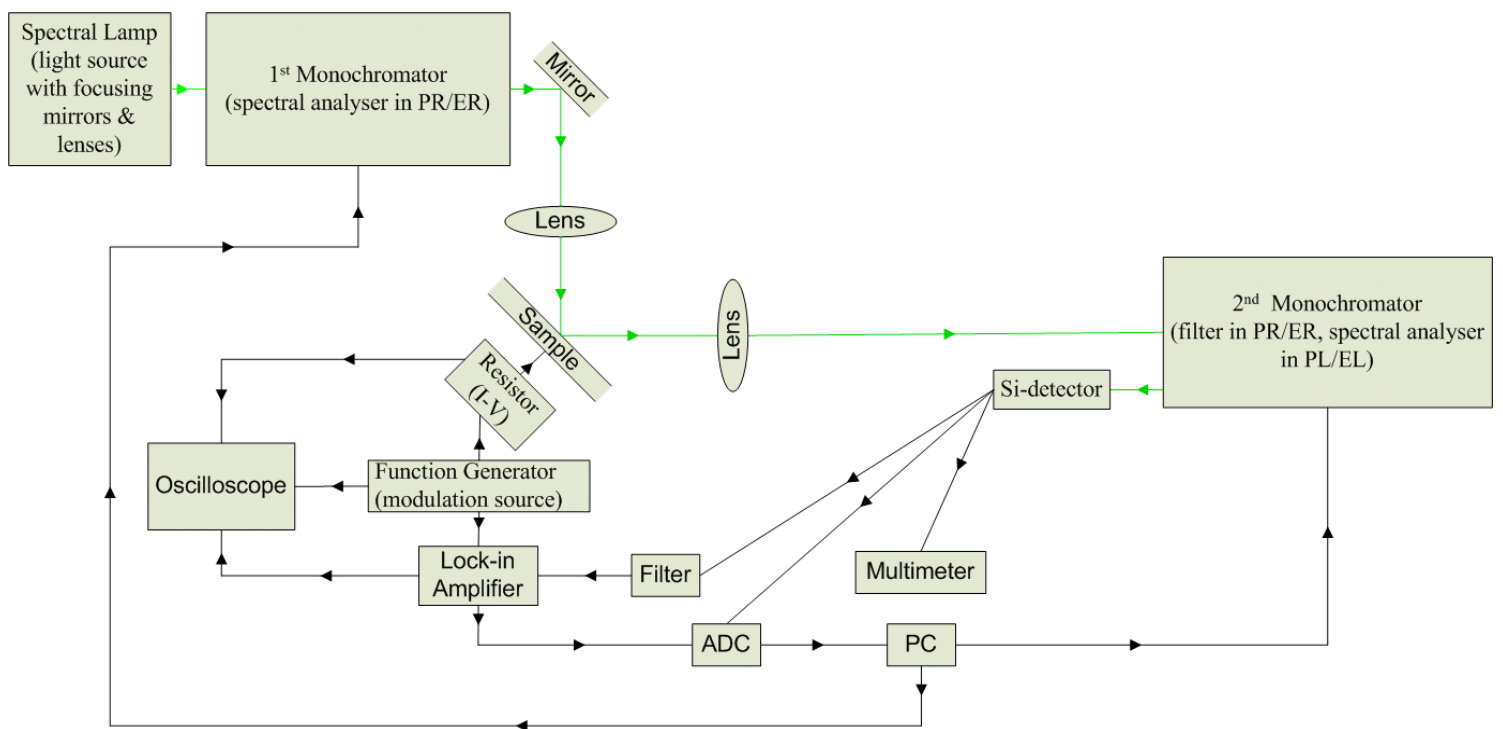
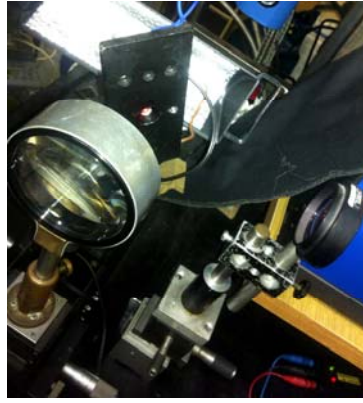


Figure 2.3.1.2.1 Block diagram of the ER instrumentation setup.



a)



b)

Figure 2.3.1.2.2 a) One of the resistors used for the real-time I-V display setup as described above and b) the InGaN/GaN PIN diode externally illuminated on the back side, while electrically contacted at the front side.

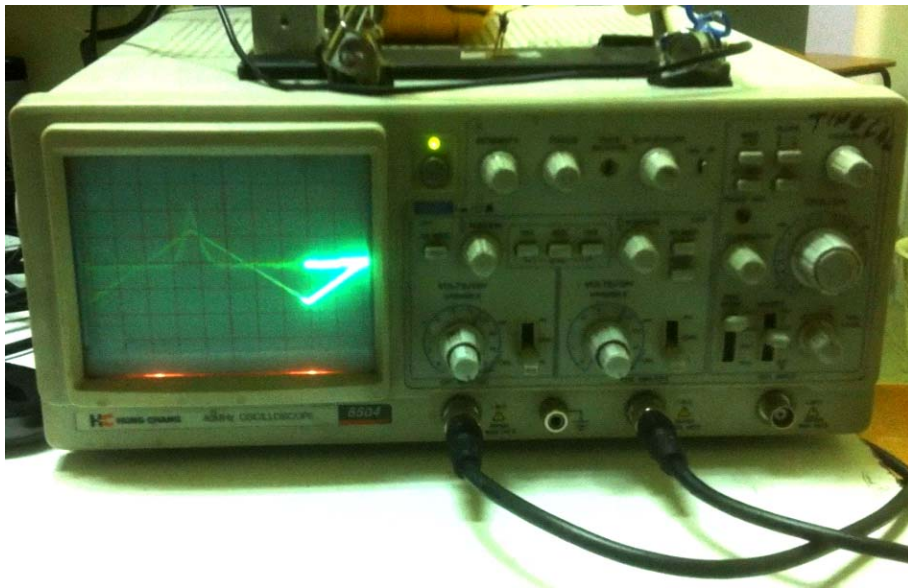
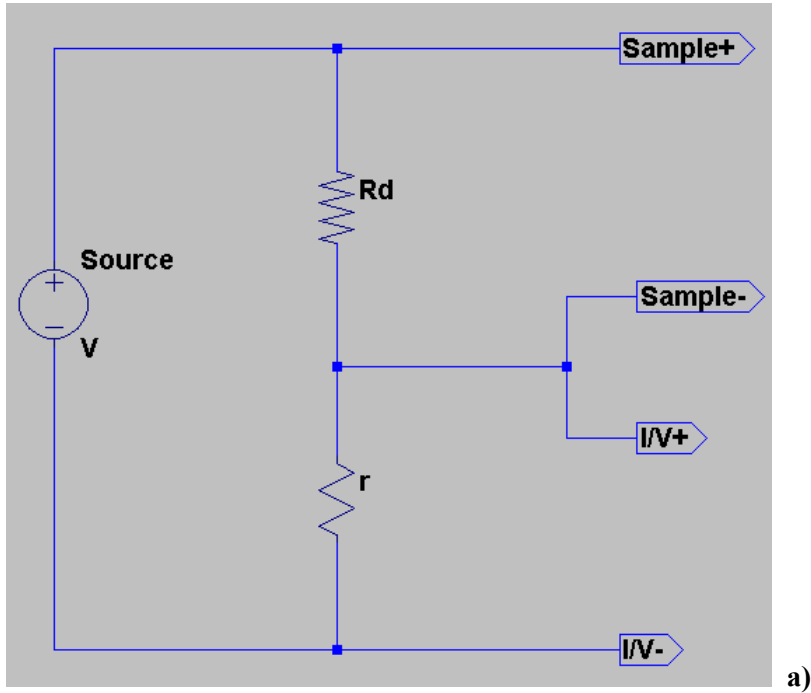


Figure 2.3.1.2.3

a) Voltage divider setup schematic for the real-time I(V) and b) real-time display of the I(V) of the InGaN/GaN PIN-diode: a triangle pulse generated by a function generator results in an exponential I(V) response of the sample resembling typical diode characteristics synchronous to the rising half period of the triangle signal and y-axis mirrored in the falling half period.

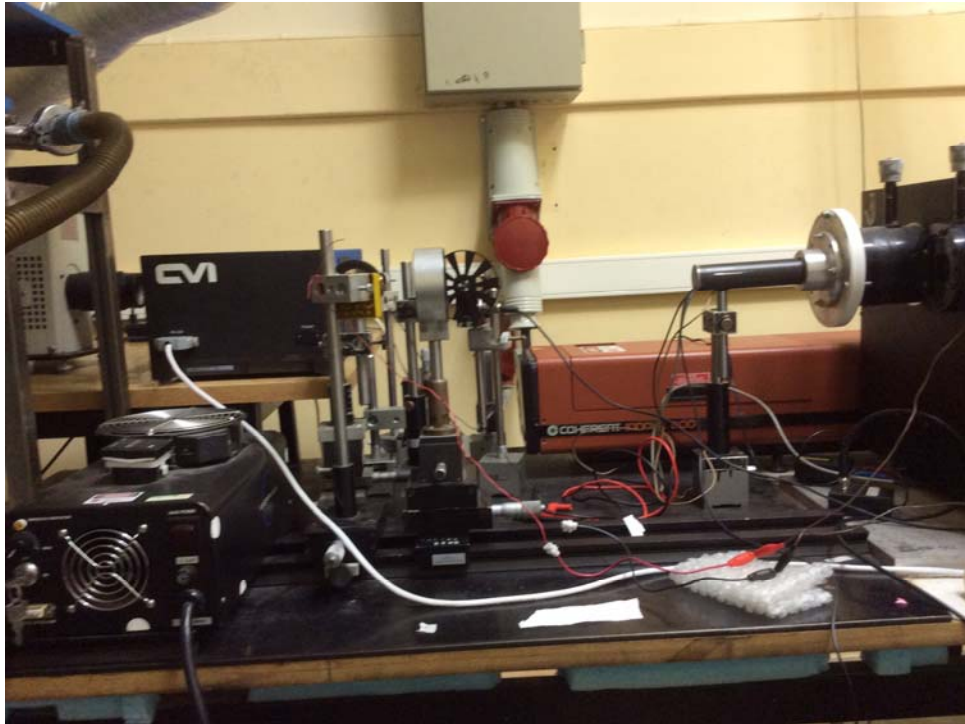


Figure 2.3.1.2.4 Experimental setup with Xe-lamp, Ar⁺- and Kr⁺- lasers, and monochromators in the incident and reflected beam path.

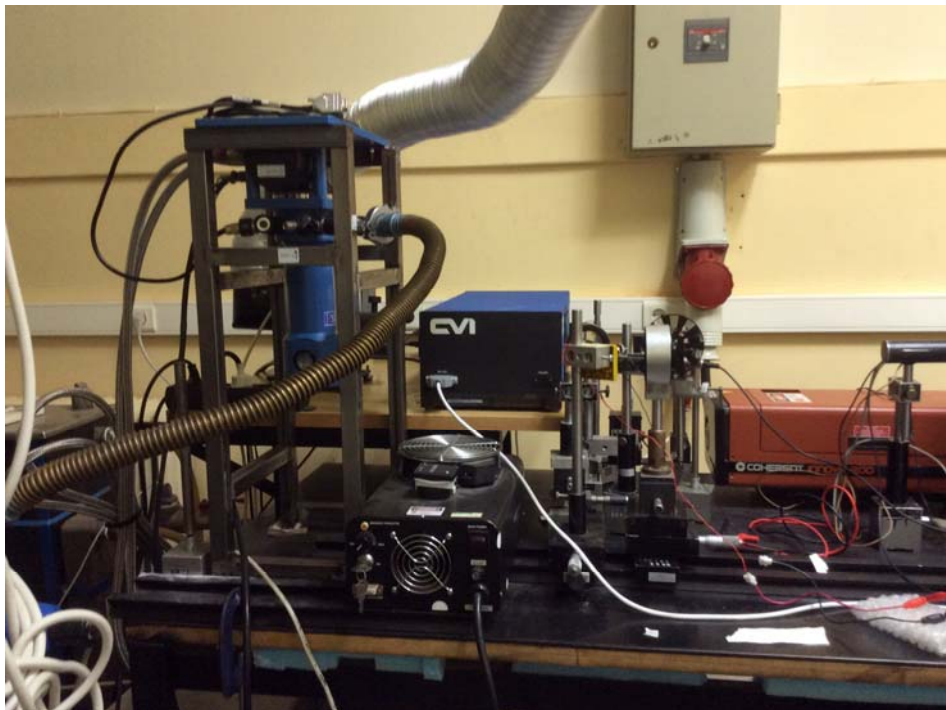


Figure 2.3.1.2.5 Experimental setup with low-temperature equipment.

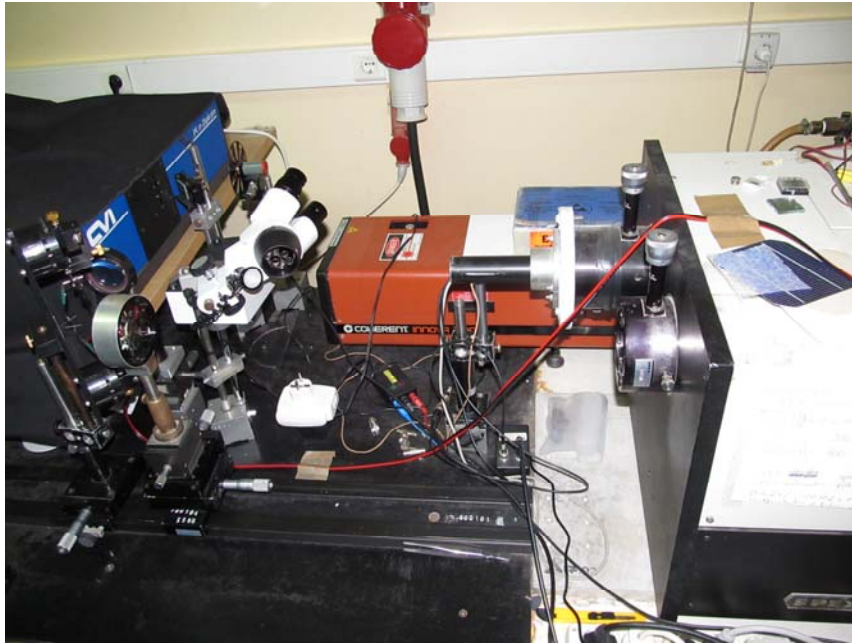


Figure 2.3.1.2.6 Final setup, including micropositioners and a light microscope for the metal probes pins accurate positioning.

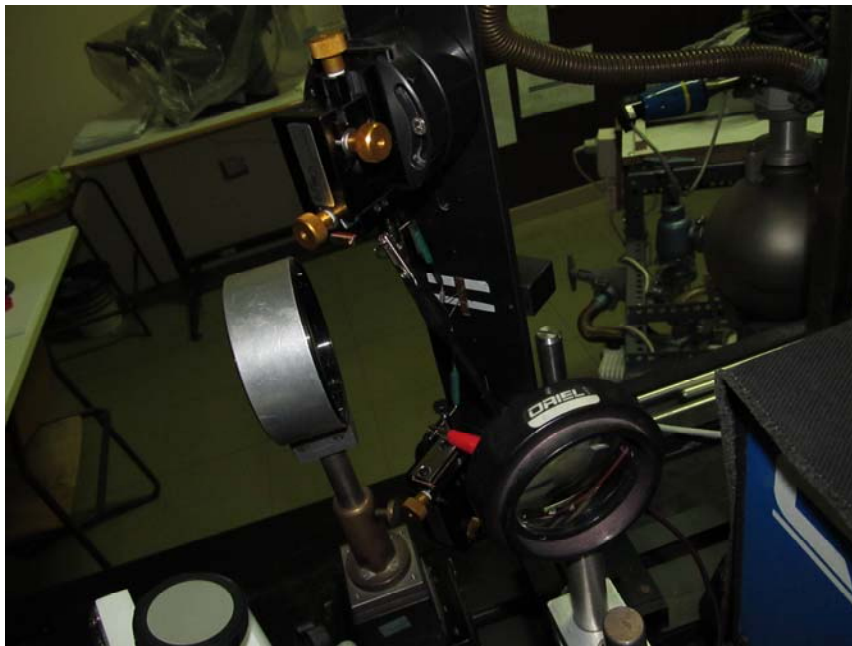


Figure 2.3.1.2.7 Final setup close view, of the micropositioners for the metal probe pins accurate positioning.



Figure 2.3.1.2.8 Final setup close view of the contacted diode exhibiting EL, also in the visible spectral range.

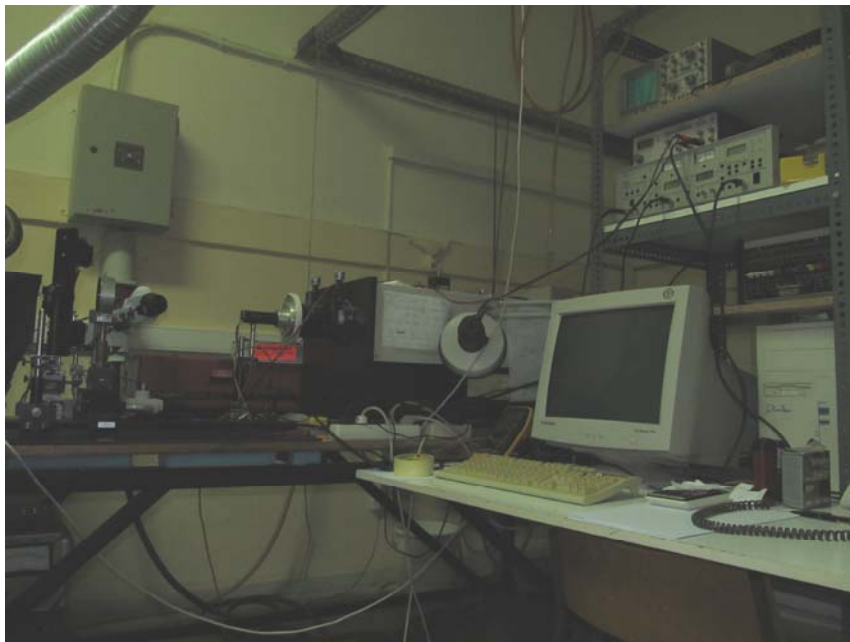


Figure 2.3.1.2.9 Overview of the ER and EL final setup including micropositioners and a light microscope for the metal probe pins accurate positioning.

2.3.1.3

ER instrumentation setup optimization

In order to maximize the sensitivity and performance of the instrumentation setup, an optimization process was conducted using the reference photovoltaic cell sample. The experiment parameters were optimized with respect to an initial set of parameters with detectable values of R and ΔR . In all cases, the signal monitor OUT of the rear panel of the Lock-in amplifier was used to monitor the locked-in and amplified signal of ΔR on an oscilloscope channel. It was sinusoidal independently of the modulation signal function being of square, triangle, or sinus functional form. Note that the reference signal is typically a 2Vp-p, square, zero-offset signal with frequency set equal to the signal fed to the sample.

2.3.1.4

Lock-in amplifier settings optimization

The following Lock-in amplifier parameters were optimized (**in bold:** the settings finally used).

Bandpass filter: **IN/OUT** (usable signal only in the IN setting)
Line: **IN/OUT** (indifferent)
Linex2: **IN/OUT** (indifferent)
Mode: **f/2f** (usable signal only in the f setting)
Trig: **Up/Sinus/Down**
Time Constant: **1s** optimum setting for inputs of 5-15Hz

(For smaller time constants, the lock-in failed to end up in a stable phase parameter, for greater time constants it just needed more time to end up in a stable phase parameter)

Post: 1/0.1/**NONE** (indifferent)
Selected output: **X/R**

(the absolute of X shape was recorded by choosing the R-output setting. Note that the R output of the Lock-in should not be confused with the R Reflectance abbreviation)

2.3.1.5

Passive filter optimization

A passive 40kHz low-pass Filter was investigated in view of a possible improvement of the signal. It was tested using the function generator. Its function was verified as a 40kHz low-pass Filter. It was observed to have a beneficial effect by cutting out the existing above 40kHz noise, thus improving the sinusoidal signal observed on the oscilloscope channel used for monitoring ΔR .

2.3.1.6

Function generator settings optimization

The function generator signal parameters were also investigated in order to define the optimum pulse width, function, frequency, and offset for the studied samples. The square function was found to be the optimum generator function. Additionally, it was observed that below a certain amplitude value, depending probably on the sample resistances and/or the Cut-off Voltage and/or the instrumentation sensitivities, no ΔR signal was present at the output. Above this amplitude-threshold, the ΔR signal increased with increasing amplitude resembling a sinusoidal signal shape with improved signal-to-noise ratio. Special care was taken to calculate the power consumption and avoid any unwanted heating of the sample by keeping a low power level. For each sample, a slightly different frequency was found to be optimal; for the sample of reference, it was 7Hz. Nevertheless, the 7Hz-10Hz range resulted in similar waveforms and signal qualities. Out of this range, there was a reduction of signal quality. The offset setting did not seem to affect the ΔR signal. It was set to 0V DC in order to decrease a possible heating of the sample.

2.3.1.7

Optics adjustments

The optics adjustment required manual optimization skills. It was always performed after a pre-scan following visual beam-path adjustment. Scan as a term is used to describe the measuring process of recording the signal for successive specific wavelengths and registering the optimum wavelength, where a reasonably high level of R signal is present. The numerous optics parameters which were optimized are given in Table 2.3.1.7.1.

Table 2.3.1.7.1 Optics optimization parameters

1.	Adjustment of the collimator of the spectral lamp
2.	Spectral lamp distance from the monochromator at the light source side
3.	Spectral lamp height
4.	Mirror distance at the exit of the monochromator at the light source side
5.	Mirror height and angle defining the incident beam-path
6	Distance, height, and angle of the focusing lens between the mirror and the sample
7	Angle of the sample (45° with respect to the incident beam path)
8	Height of the sample
9	Distance, height, and angle of the focusing lens between the sample and the entrance-slit of the monochromator at the detector side
10	Height of the focusing lens between the monochromator exit-slit and the detector

One has to take into consideration that in a multi-parametric system such as this, one often has to perform the optical adjustments more than once. A major change in one parameter usually means that a number of the other parameters have not still reached the optimum.

2.3.1.8

Holder & probes optimization

The probes had to be continually improved as to facilitate the positioning procedure and minimize the inevitable small scratching and piercing damages. Five main versions of the progressively optimized holder and probes were extracted.

The first version was an iron base, on top of which were situated 2 magnets used for electrical isolation, versatility, and low cost. On each magnet, a simple guitar tuner was glued and used as a sensitive lever having a 15:1 rotation ratio (15 turns of the knob for 1 turn of its rotating part) in order to take advantage of landing the probes smoothly on the sample and avoid any damage of the sample surface. On each lever, a thick electrical copper wire was glued. Copper was selected as a material of high conductivity and very good mechanical properties such as high stiffness to avoid accidental bending, but pliable enough to bend when needed. At one end of the copper wire, close to the lever, a long connector wire was added, while at the other end, a gold plated tip was soldered. Gold was selected for its high conductivity and maximum resistance to oxidation. This golden tip was further processed and sharpened in order to reduce the contact area and thus achieve a precise point contact.

The second version, used longer tips, also gold plated, so as to facilitate the positioning process and prevent the probes from obstructing the light beam path.

The third version, utilized an existing steel laboratory holder. It was installed at the same metal base by taking care to efficiently isolate it electrically and thus avoid short circuiting the two probes.

For the fourth version, the second version was further improved. The metal base was drilled so that the front side of the sample could be electrically accessed, while the back side was properly illuminated by focusing the incident light beam on it. This arrangement allowed thus a configuration as used in an ER measurement, completely unobstructed, since the probes were on the front side. This change was necessary because the PIN LED sample front side was nearly completely covered with a highly reflecting metal film. The penetration of the incident beam to the underlying GaN/InGaN layers is partially blocked and the useful ER signal is possibly several orders of magnitude lower than the reflection signal of the metal layer. Additionally, 2 stainless steel straight pins were used because of their relatively good conductivity, high hardness, and high resistance to oxidation. These longer pins facilitated the positioning. In fact, owing to these point pins, the holder positioning precision was advanced to a surprising level of about 100 μ m in diameter. Had the tip been sharper, it would have probably become susceptible to plastic deformation through bending when touching the surface of the sample.

The final holder version is shown in Fig. 2.3.1.2.8, incorporating 2 XYZ micropositioners and a 20x/40x Light Microscope for accurate pin probes positioning.

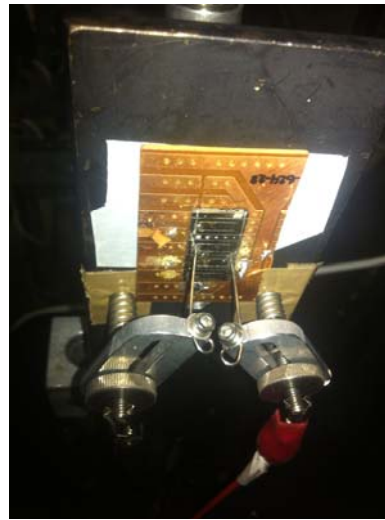
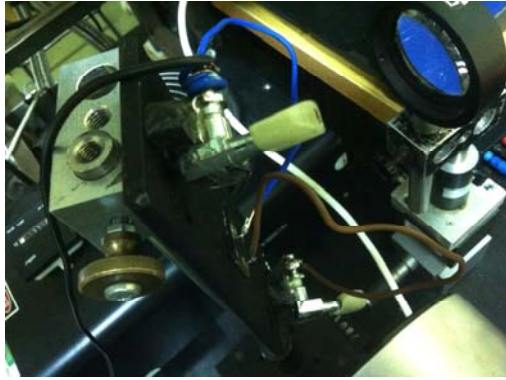


Figure 2.3.1.8.1 Successive holder improvements, using sharper probes and double-side access. The probes are positioned on the front side, while the light beam is focused at the back side through a hole drilled in the holder base.

2.3.1.9

Measurement procedure

Following the optics optimization process, the measurement procedure included only fine-tuning of a few parameters as for example the lock-in phase and sensitivity. This procedure is summarized in Table 2.3.1.9.1.

Table 2.3.1.9.1 ER measurement process steps

1. Pre-adjustment of the sample holder metal base orientation, as moving it later could compromise the probes positioning
2. Positioning of the electrical probes on the device under study
3. Measuring the sample forward and reverse resistance with the lights and beam off, since a sample, for example a photovoltaic cell, would add its own voltage and obstruct the resistance measurement. The scale used is noted, as the samples are not exclusively resistive and could exhibit a different resistance for different induced voltages.
4. A resistor of less than 1/100 of the minimum of the above resistances in series with the sample is inserted to determine its current shape in real-time. This voltage is displayed on an oscilloscope. If an exponential characteristic $I(V)$ is expected, it can thus be verified.
5. Its forward and reverse Cut-off Voltage is measured, with the lights and beam off. Additionally, if a photovoltaic sample is used, its voltage output is measured with a flashlight on and off to verify its positioning. Similarly, if an LED sample is used, it is temporarily turned on to verify its positioning
6. The optical systems are optimized as listed in Table 2
7. A pre-scan is conducted to identify the ΔR maximum. The sensitivity of the Lock-in amplifier is set a little more than the ΔR maximum
8. The remaining system parameters are optimized at the ΔR maximum and the corresponding wavelength is noted
9. A scan with a high number of accumulations is performed to improve the signal-to-noise ratio (SNR)
10. The Reflectance signal at the wavelength of maximum Reflectance is checked. It has to be the same as at the beginning of the experiment. The contact resistance is also checked in order to confirm the contacts stability; it should be the same as at the beginning of the experiment

2.3.1.10

ER reference sample

A CIGS ($\text{Cu}(\text{In,Ga})\text{Se}_2$) thin film solar cell (TFSC) developed by Prof. Dr. Martha-Christina Lux-Steiner's research work group at the Laboratory of Compound Semiconductors of the Department of Solar Energy Research of the Helmholtz Centre Berlin for Materials and Energy was used as a reference sample. The CIGS thin film solar cell with Al/Ni/Al:ZnO/i-ZnO/CdS/Cu(In,Ga)Se₂/Mo/glass configuration and successive layer sequence with thickness of p-type absorber Cu(In,Ga)Se₂: 2.5-3.0 μm , n-type CdS buffer: 30nm, intrinsic ZnO: 70 nm, n-type ZnO with Al dopant: 500 nm was used as Reference to test the experimental setup. The cell was designed in *substrate configuration*: the sun rays penetrate through the transparent n-type layers, e.g. the window layer (Al:ZnO/i-ZnO) and the ultra-thin buffer layer (CdS), before reaching the p-type absorber. Doped ZnO layers are typically used as transparent electrodes in all kinds of optoelectronic and photovoltaic devices as demonstrated in one of the author's recently published works [146] referred to *Electrochemically Deposited Highly Doped ZnO Bilayers on Ga-Rich Chalcopyrite Selenide for Cost-Effective Photovoltaic Device Technology*. Moreover, the Ni/Al grid functions as the cell negative front-contact whereas the Molybdenum layer as the positive back-contact. The dimensions of each cell are 0.5cm x 1cm. The present reference sample of 2cm x 1cm contained 4 cells.



Figure 2.3.1.10.1 Reference CIGS solar cell.

2.3.2

Electrical characterization by Capacitance-Voltage Profiling

Initially, capacitance measurements were conducted using the CpRp mode of an LCR instrument with an equivalent circuit of capacitor parallel to a resistor. The dependence of the capacitance on the applied voltage was attributed to the well known [68] phenomenon exploited by the technique of Capacitance-Voltage Profiling (CVP). A region where the capacitance was not strongly dependent on frequency had to be found by manually performing measurements on the 6 frequency points available: 100Hz, 120Hz, 1kHz, 10kHz, 20kHz and 100kHz. As stated in Chapter 3.2.7.3.2, the AC signal is kept to a minimum to retain the “small signal approximation”: 0.1V rms was used in this work. The DC signal is necessary to investigate the nonlinear dependence of the capacitance on voltage. Another important for the measurement, nonlinear factor, as mentioned in Chapter 3.2.2.2.1, is the naturally nonlinear reverse bias $I(V)$ which causes a nonlinear series and a nonlinear parallel resistance which, on their turn, have to be taken into account. The otherwise obligatory need of evaluating these resistances was successfully eliminated by introducing a new method for calculating the capacitance through the response of the device, as elucidated in Chapter 3.2.3.4. If an intrinsic region exists, such as in the case of PIN diodes or Schottky diodes incorporating an intrinsic semiconductor region between the doped semiconductor region and the Schottky metal contact, it just adds to the depletion region width as almost no carriers exist in that region. Intricacies of this method and the engineering behind it are analytically explained in Chapter 3.2. It has to be noted, that this work demanded knowledge combining Physics, Electronics Engineering, and Materials Science and Technology in almost every aspect of it, and also a greatly varying literature [1]-[165] to support such an attempt. A considerable amount of effort was invested in devising a method for accurate measurements of the capacitance and also in generalizing as much as possible all the exploited theories using as little assumptions as possible in both, when creating the equations and when considering the grown device individual, non-ideal characteristics. As shown in Chapter 3.2.11.2, this included the derivation of the general equations for any doping profile in order to theoretically simulate the CVP and explain phenomena related to nonlinear CVP curves. Various explanations have been given in the literature [20], [68], [147]. The prevailing factor for these phenomena is assumed to have been revealed in this work, as shown in Chapter 3.2.11.2. Distinction between the depletion region width and the x-axis position variable was made proving that except for the case of a Schottky diode, only the effective dopant concentration of the depletion region can be obtained from the CVP measurements, as explained in Chapter 3.2.8. Other methods such as Secondary-ion mass spectroscopy (SIMS) can be used, if an x-axis position profiling is necessary. Moreover, because of this theoretical fact, an assumption has to be made for the doping profile, as explained in Chapter 3.2.11.1.

Compared to ref. [148], a more generalized equation was derived for the calculation of E_{pol} (internal polarization field) by incorporating the term of unintentional doping. A change of E_{pol} by more than 5% is expected by omitting this term. The unintentional doping concentration of the intrinsic region is, in many cases, half of the donor doping concentration and thus cannot be neglected. Though it is very probable that almost random doping variations occur during growth between different doping regions, in lack of a better theoretical model, a constant doping profile was assumed, as described in Chapters 3.2.11.1-2.

2.3.2.1

CVP instrumentation setup

The instrumentation setup consists mainly of an LCR meter for the measurement of inductance (L), capacitance (C), and resistance (R). Most often, this type of instrument is limited to 2 component circuits. Though the manuals imply that 3 component circuits are more appropriate, an equivalent circuit of the device under investigation with more than 2 components is not supported, as explained in Chapters 3.2.1-2. Advanced electronics engineering knowledge and experience was necessary to introduce a method to measure the device under test (DUT) parameters and also correctly interpret the results, as explained in Chapters 3.2.1-3. This ultimately means that equivalent circuit analysis (equivalent network analysis) [149], [150] of a nonlinear voltage and frequency dependent device was an integral part of this work.

The complete CVP instrumentation setup is presented in Fig. 2.3.2.1.2. It consists of a Keysight E4980A-Option 001 LCR meter, 2 electrode pins micropositioners, a custom light blocking metal chamber, a 10x - 60x light microscope, a PC controlling the measurement and utilizing a custom program written in Labview environment (developed by PhD student Martin Guttman) and their interconnections. The wires might seem as a trivial component of the setup, however, the engineering reality is that they have an impedance response of their own and have to be checked prior to any measurement, especially in the MHz frequency range.

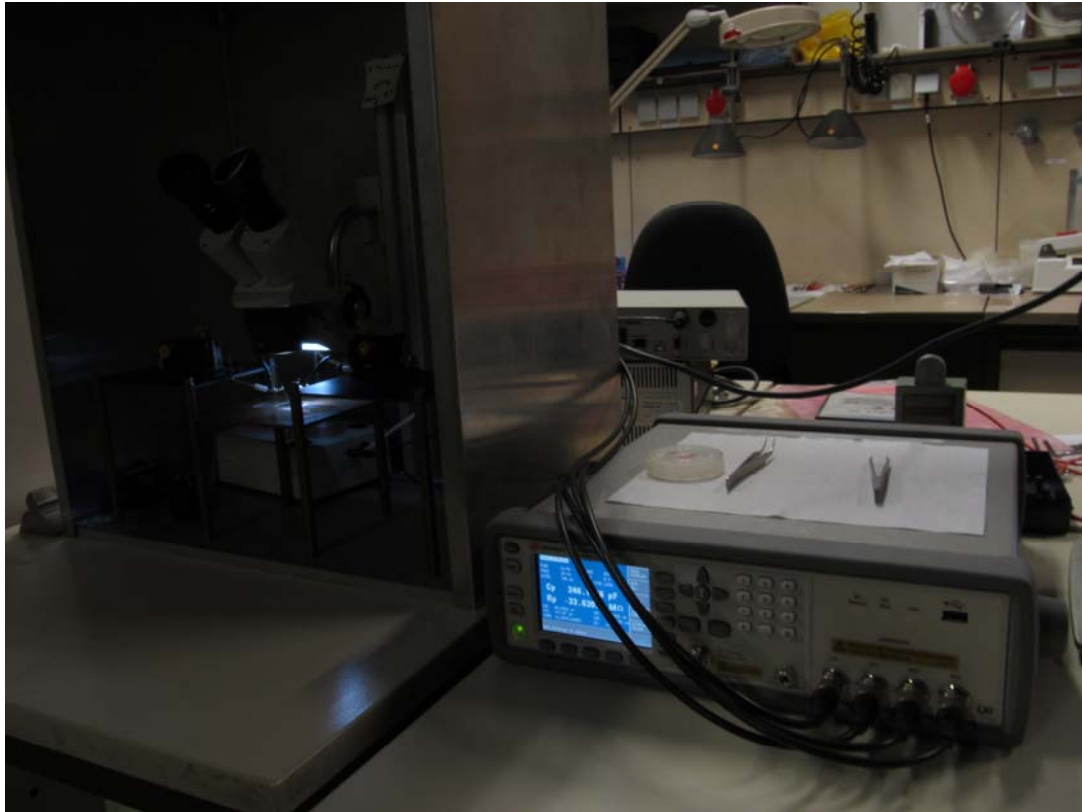
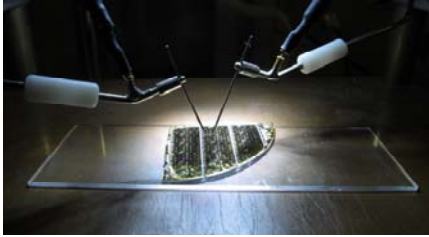


Figure 2.3.2.1.1 The LCR meter (right), the light microscope (left) and the micropositioners setup to accurately position the probe pins.



(Sample inside metal box with microscope and pins on micropositioners)

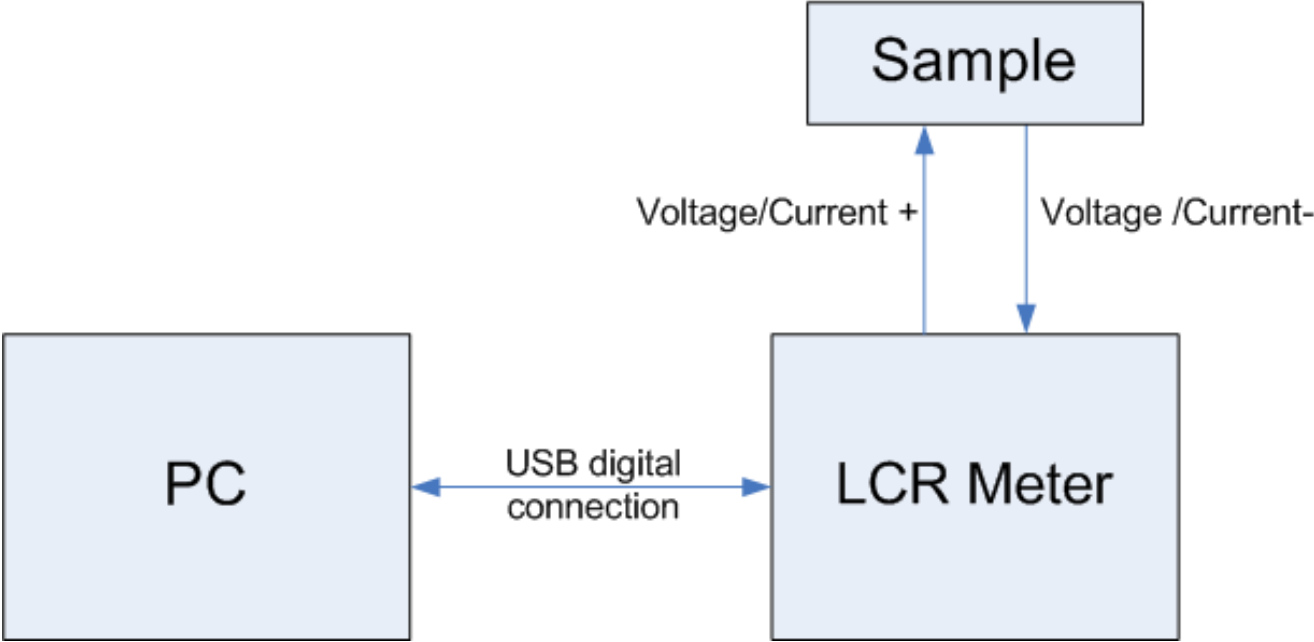


Figure 2.3.2.1.2 Block diagram of the CVP instrumentation setup and close view of the contacted sample.

2.3.2.2

CVP calibration procedure

Reference samples are generally used for verification, calibration, and comparison purposes and, in principle, ought to be as close as possible to the samples under investigation; they ought to have an as detailed as possible description in their documentation.

The CVP reference samples of this work would ideally be UVC PIN LEDs with a known doping profile and CVP characteristics. Since an ideal reference sample does not exist, an appropriate components circuit was devised, as explained in Chapter 2.3.2.2.

The need for the verification and rigorous improvement of the method for calculating the capacitance led to an astonishing relative error reduction by more than 2/3 in every devised components circuit, as noted in Chapter 2.3.2.2.

A discrete components circuit was used as calibration sample. The purpose for such a sample arises from the fact that one cannot dissect a real sample, isolate the capacitance, and measure it. For this reference sample, values close to the measured values were used. Measurements with the components isolated were performed to have an as close as possible estimate of the true values of the components as they were 5% tolerance components meaning that their true value is within the $\pm 5\%$ of the nominal value. This is only possible, because the accuracy of the measurement is usually greater than the tolerance of the resistors. The tolerance of the capacitor also was 5%. Moreover, every possible measurement method, when measuring the capacitor, showed the same value, which is a reasonable result, since it is the simplest case of a sample. The capacitor in series with the low resistance resistor (Fig. 3.2.1.1), the capacitor in parallel with the high resistance resistor (Fig. 3.2.1.2), and the complete series and parallel combination, as shown in Fig. 3.2.2.1, were measured to identify any present discrepancy of the methods.

Capacitance frequency measurement using discrete components

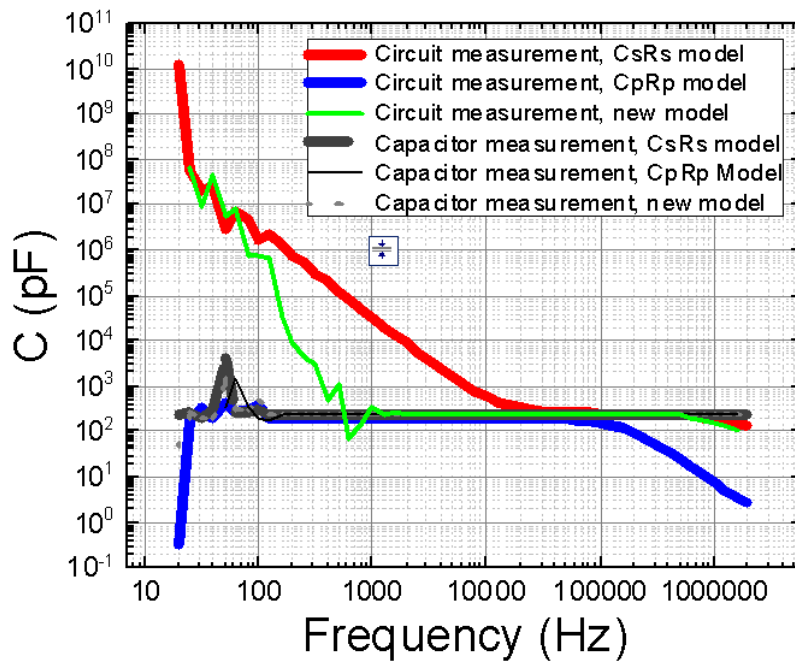


Figure 2.3.2.2.1 Comparison of the calculated capacitance by the use of the CsRs model (red line), CpRp model (blue line), and the new model (green line) with the value calculated with every method (grey lines) by isolating the capacitor. All models calculate the capacitance using the directly measured impedance and phase.

Capacitance frequency measurement using discrete components

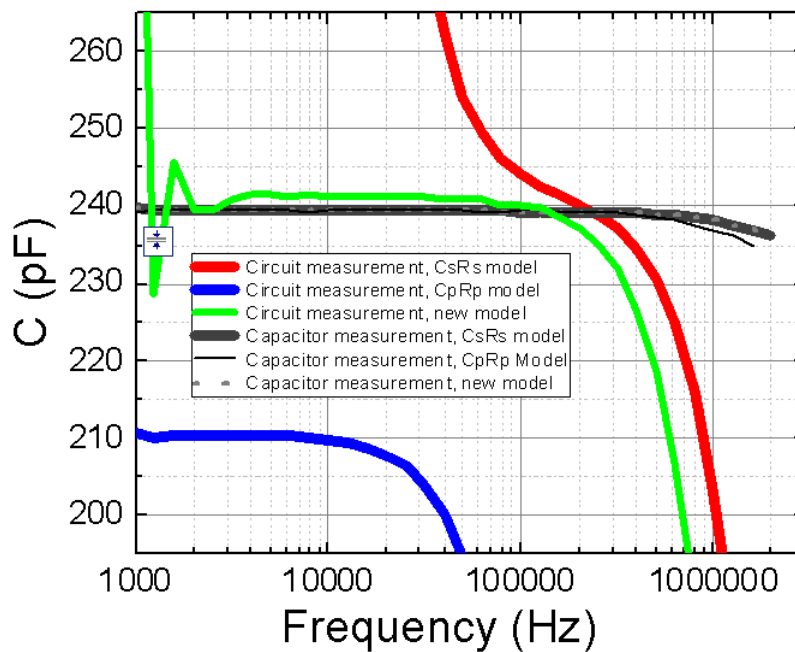


Figure 2.3.2.2.2 Comparison of the calculated capacitance (zoom-in).

Each equivalent circuit attempts to model the true circuit but new model is evidently closer. In this case, the true capacitor value seems to be approximately 240pF. The CsRs model is completely off whereas the CpRp model shows an approximately 14% deviation from the true value. The new model shows an approximate deviation of 0.8%. The nominal value was 245pF and the tolerance was 5%, which means that the true value lies within the 233-257pF range. The 240pF, which seems to be the true value, is well within this range.

It is very important to point out that the frequency of choice is in the constant range of the new model curve, different for different samples. For the samples of this work, an investigation for the choice of the optimal frequency was conducted, as presented in Chapter 3.2.7.4.

2.3.2.3

Measurement procedure (CVPT, ZfT, I-V)

The measurement procedure consists of conducting CVP but also preliminary and verification measurements as well as documenting the procedure. Documenting of the procedure includes photographing the quarter wafer sample (Figs. 2.1.2.3-7). The quarter wafer samples which typically consists of some thousands of diodes. Mapping them in a columns and rows configuration allows reproduction of the measurements as well as conducting more detailed investigation of specific diodes once they have been preliminarily evaluated and compared. Once the diodes of the examined quarter wafer samples have been mapped, impedance and phase frequency measurements (ZfT) and CVP utilizing also the phase response (CVPT) are conducted. ZfT measurements at the limits of the voltage range are used to verify that the theoretically predicted ZfT response is consistent with the equivalent circuit. In this work, 0 - -5V reverse bias and 200-280kHz were selected used as ranges as explained in Chapter 3.2.7.4.

CVP utilizing also the phase response (CVPT) follows as the main part of the measurement. It consists of three CVP measurements in different frequencies also recording the phase frequency response, as a complementary measurement of the impedance which is naturally recorded on each bias point. This allows a comparison between three frequencies to investigate any true frequency dependence in the used range. In this work, for the frequency range used, no real frequency dependence was observed though as explained in Chapter 3.2.2.3, plasmonic frequency dependence can easily be the result of an oversimplified equivalent circuit. It has to be noted that for every measurement, the frequency points are a geometric progression (the common ratio of choice usually being $10^{0.1}$), resulting in a logarithmic scale sampling. This is the typical method in electronics since most phenomena are logarithmically dependent on frequency. This also defines the frequencies used. The minimum frequency used

was 200kHz. The next 2 frequencies were the two next terms in the geometric progression using a 10 points per frequency decade frequency resolution ($10^{0.1}$ common ratio). This resolution was selected as an optimum solution between the two extremes of the frequencies being too close to distinguish any differences in the measured impedance and phase and being too far to accurately assign the response in the geometric mean frequency when calculating the frequency derivatives needed as explained in Chapter 3.2.3.4. These two frequency terms were thus 251.79kHz and 316.98kHz. Conveniently combining those three frequencies created 3 geometric mean frequencies. The combinations were the first and second frequency, their geometric mean being 224.40kHz, the first and the third, their geometric being 251.79kHz and finally the second and the third, with a geometric mean of 282.51kHz. The equations used for the effective calculation of the capacitance are presented in Chapter 3.2.3.4.

As explained in Chapter 2.3.2.3 ZfT was used a preliminary measurement but can also be used after the CVPT to verify the diode measured has suffered no degradation. Since in reverse bias the currents are very low, such a verification is only needed only when measuring the same diode in future measurements and the damage of the diode is solely due to the almost inevitable metal contact scratching due the pins piercing some of the metal layers when contacting. ZfT is an impedance measurement at a certain bias at different frequency points also recording the phase response, as explained in Chapters 2.3.2.3 and 3.2.3.4.

The current voltage (IV) characteristic can also be obtained if necessary as a preliminary and verification measurement to confirm the proper function of the diode measured. For the reverse bias used the SNR of the I(V) was somewhat low. Also the CVP complementarily measures the DC current at each DC voltage point and the AC voltage signal is almost always relatively low compared to the DC voltage so a graph almost identical to the I(V) is automatically obtained while performing the CVP measurement. Consequently, the ZfT was preferred as preliminary and verification method.

3

Results & Discussion

3.1

Electroreflectance & Electroluminescence Spectroscopy

3.1.1

ER Spectroscopy

3.1.1.1

Reference sample ER spectra & fitting

The measured ER spectrum of the reference CIGS TFSC presented in Fig. 3.1.1.1.1 was fitted in accordance with Eq. (2.3.1.3). The scanned energy (E) and the dimensions of the critical points (m) contributing to band energy were varied. The arbitrary constants of the multiplication (C_3) and the added offset (C_2) factors were also taken into consideration thus making the fitting a 2-variable (E, m) / 5-parameter ($\phi, E_g, \Gamma, C_2, C_3$) function.

Fitting for the 1D, 2D and 3D cases resulted in the calculated values of $\phi=12.7$ degrees, $E_g=1.51$ eV, $\Gamma=47.9$ meV. The best fitting curve was for the 3D CP approximation, as calculated and compared by the R squared coefficient of determination in the least-square fitting. It has to be noted that the 2D CP approximation differed only by 17.5% and the 1D by 35.6% from the 3D.

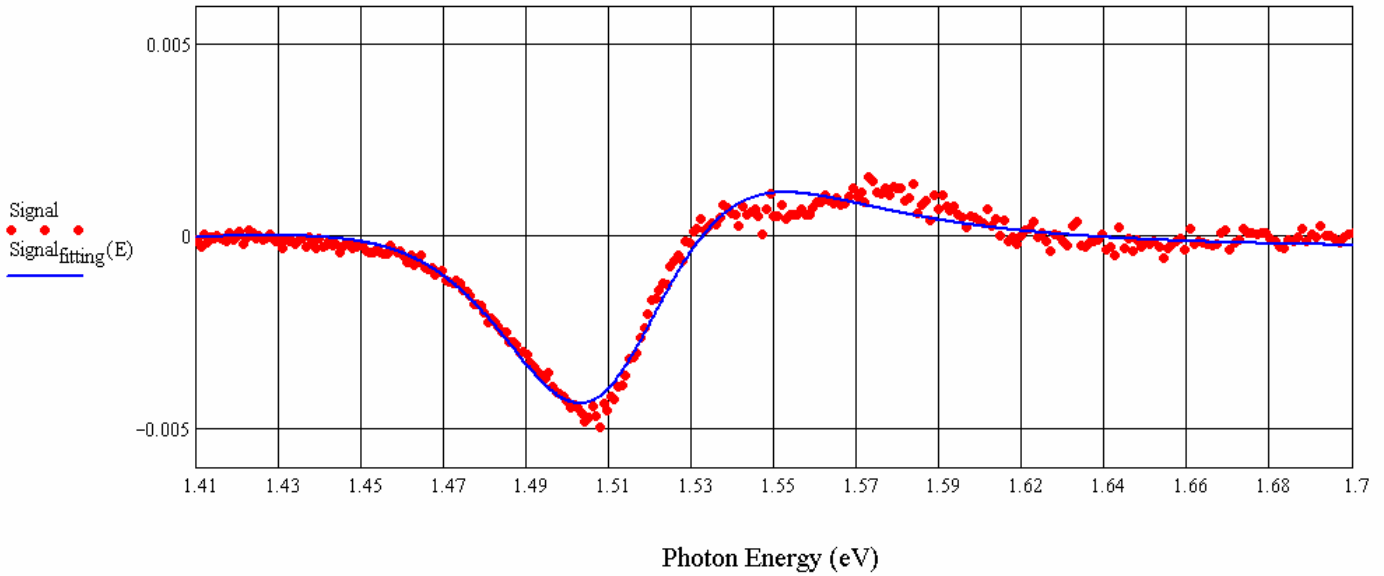


Figure 3.1.1.1.1 5-parameter fitting of the ER spectrum of a CIGS TFSC used as reference sample.

Removing the added offset factor, finding the minimum and maximum of the fitting curve, and introducing it to the simpler fitting as indicated by D. E. Aspnes [117], produced similar results.

In Fig. 3.1.1.1.2, the Reflectance (R) and ER ($\Delta R/R$) spectra of the CIGS thin film solar cell used as Reference sample, in this study, are presented.

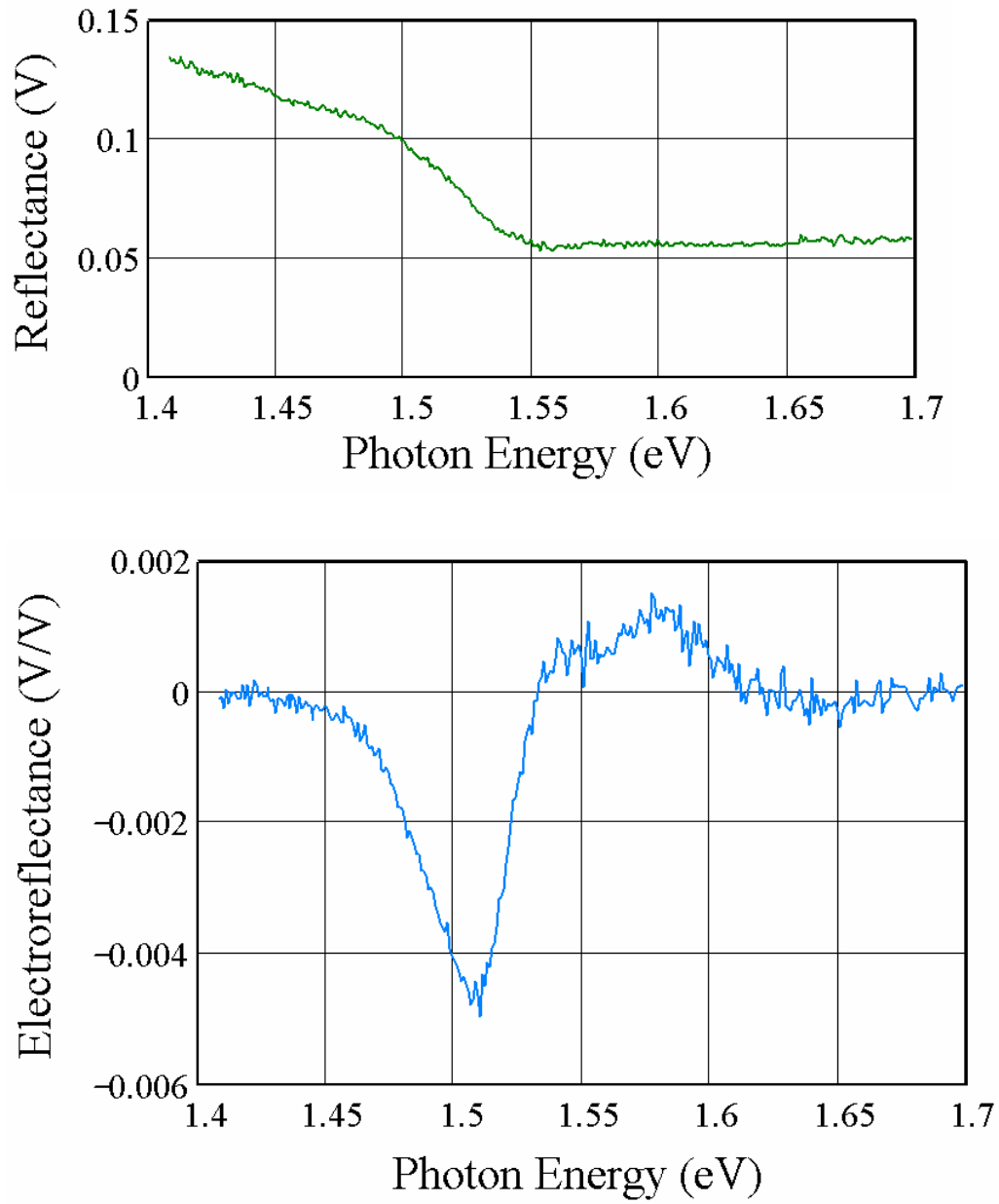


Figure 3.1.1.1.2 R and $\Delta R/R$ spectra of the CIGS TFSC reference sample.

3.1.1.2

GaN PIN diode ER spectra

In agreement with the theoretical model, as presented in Fig. 1.1.1.2.1, three distinct Energies are apparent in the ER measurement results (Fig. 3.1.1.2.1); E_a as a result of the VB of the heavy holes, E_b as a result of the VB of the light holes (LH) and E_c as a result of the split-off VB (SO) affected by the crystal field and spin orbit interactions.

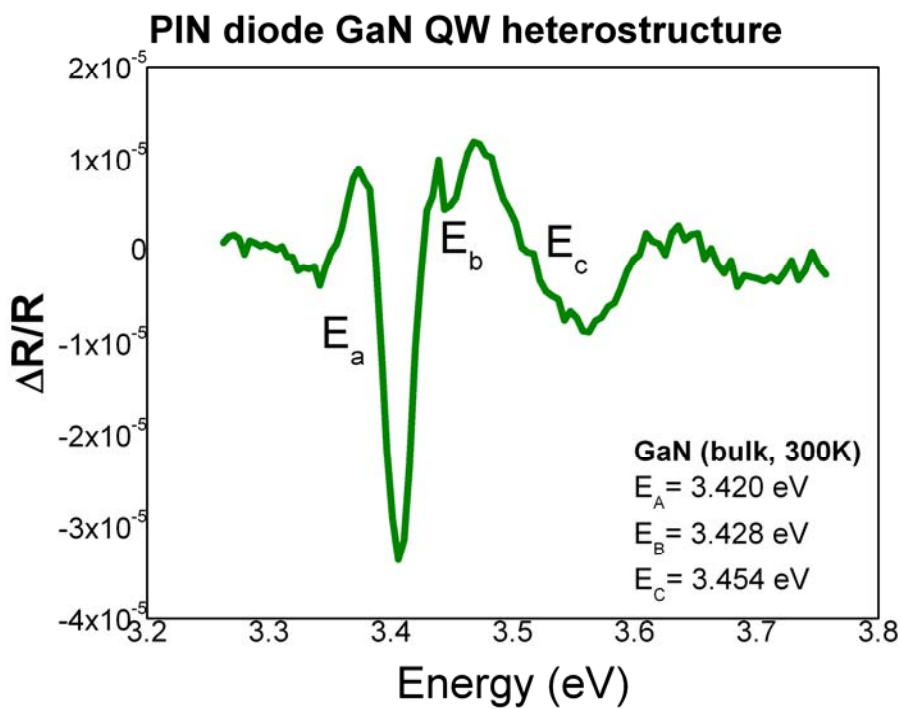


Figure 3.1.1.2.1 ER measurement, revealing three distinct energies, E_A , E_B and E_C as a result of the crystal field and spin orbit interactions within the WZ crystal structure.

3.1.1.3

InGaN/GaN PIN diode ER spectra

Similarly, in the InGaN/GaN sample, the E_a , E_b and E_c as a result of the crystal field and spin orbit interactions within the WZ crystal structure are also present. The E_a , E_b and E_c transitions of both, GaN and InGaN, are revealed, exactly in the energy range expected for the 0.055% Indium content (Fig. 1.1 [21]).

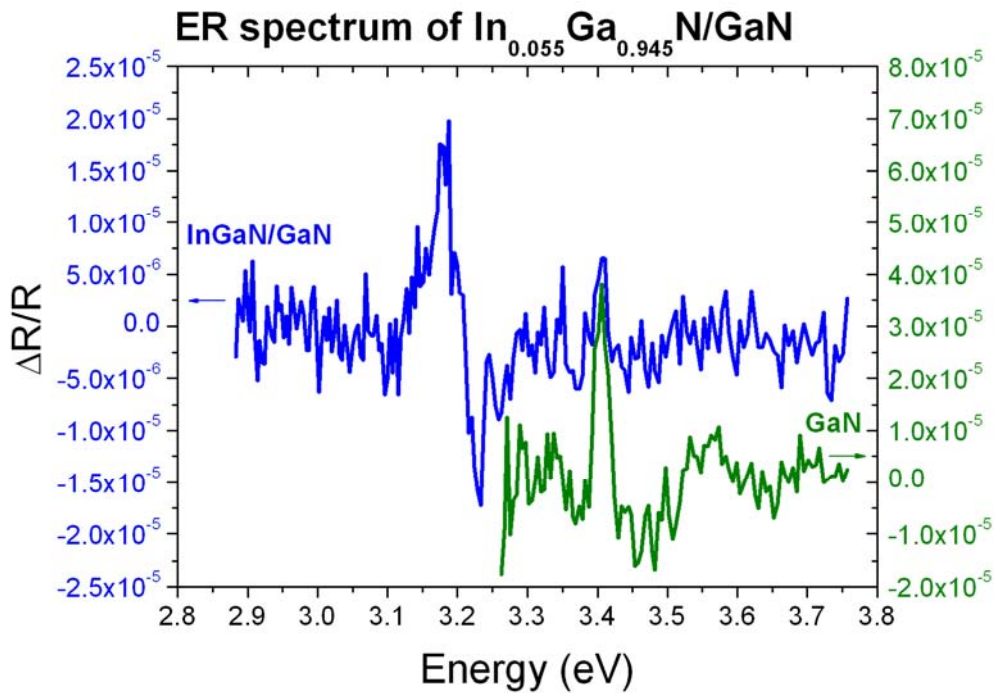


Figure 3.1.1.3.1 Comparison of the ER spectra of the GaN (no DHS) sample and the In_{0.055}Ga_{0.945}N/GaN sample.

In Fig. 3.1.1.3.1 the spectra of the InGaN/GaN QW heterostructure are compared to the spectra of the GaN reference sample. For evaluation purposes, an InGaN/GaN spectrum with a high intensity-to-noise ratio, as depicted in Fig. 3.1.1.3.2, was acquired.

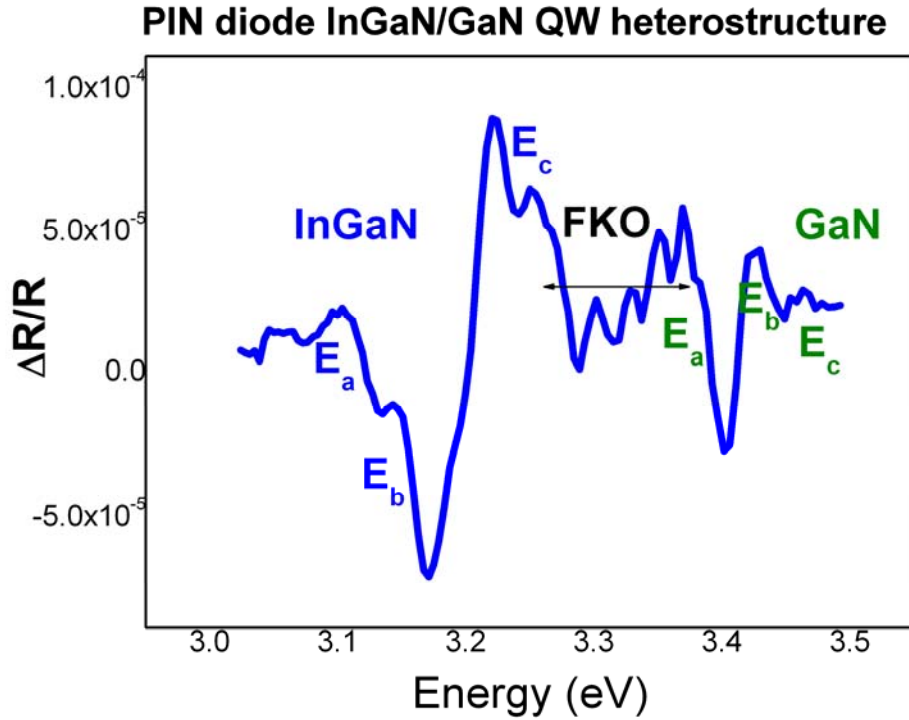


Figure 3.1.1.3.2 ER measurement revealing three distinct energies E_a , E_b and E_c as a result of the crystal field and spin orbit interactions within the WZ crystal structure for both GaN and $\text{In}_{0.055}\text{Ga}_{0.945}\text{N}$.

Considering the oscillations between $E_1 = 3.29\text{eV}$ and $E_2 = 3.60\text{eV}$ (Fig. 3.1.1.3.2-3), in principle, they could either be thickness interferences at energies below the band gap energy of GaN [55]-[63], [151]-[153], or Franz-Keldysh oscillations (FKOs) of InGaN stemming from barrier regions of the InGaN/GaN heterojunction [151], [152], [154]-[159].

In case of thickness interferences, the following Eq. (3.1.1.3.1) can be used to determine the thickness of the GaN layer, alternately the thickness of the GaN/InGaN/GaN layer region:

$$t = \frac{N \cdot \lambda_1 \cdot \lambda_2}{2 \cdot (\lambda_1 - \lambda_2) \cdot [n^2 - (\sin(\theta))^2]^{0.5}} \quad (3.1.1.3.1)$$

where t is the thickness of the film, λ_1 and λ_2 are the begin- and end-wavelengths of the spectral range referring to E_1 and E_2 respectively, $\lambda_1 > \lambda_2$, n is the refractive index of the film ($n_{\text{GaN}} = 2.82$ [160]), and θ is the angle between the incident beam and the

normal to the surface [153]. The calculation result of $t = 9.6 \mu\text{m}$ exceeds by one order of magnitude the GaN layer thickness of $0.9 \mu\text{m}$ (879 nm, Fig. 2.1.2.1).

The assumption of Franz-Keldysh Oscillations is then closely examined in accordance with published literature [151], [152], [154]-[159], [54], [161], [162].

The extrema of FKOs are given by [161]:

$$m \cdot \pi = \phi + \frac{4}{3} \cdot \left[\frac{(E_m - E_0)^2}{\frac{h}{2 \cdot \pi} \cdot \Theta} \right]^{\frac{3}{2}} \quad (3.1.1.3.2)$$

where $(h/(2\pi)) \cdot \Theta$ is the electro-optical energy, m is the index of the m -th extremum, ϕ is an arbitrary phase factor, and E_m is the photon energy of the m -th oscillation. Rearranging the terms of Eq. (3.1.1.3.2) results in

$$E_m = \left(\frac{h}{2 \cdot \pi} \cdot \Theta \right) \cdot \left[\frac{3}{4} \cdot \pi \cdot \left(m - \frac{1}{2} \right) \right]^{\frac{2}{3}} + E_0 \quad (3.1.1.3.3)$$

Inserting E_m in dependence of index n , introduced as a new variable defined by Eq. (3.1.1.3.4), results in a linear curve with intercept the E_a gap energy (fundamental energy gap E_0) for InGaN: $E_a = E_0 = 3.270 \pm 0.002 \text{ eV}$, (0.002 eV being the standard error of the linear regression, 0.04%).

$$n = \left[(m \cdot \pi - \phi) \cdot 0.75 \right]^{\frac{2}{3}} \quad (3.1.1.3.4)$$

Note that the bulk value of the fundamental gap energy in InGaN with 5.5% In is $E_g(\text{In}_{0.055}\text{Ga}_{0.945}\text{N}) = 3.150 \text{ eV}$ (Fig. 1.1) [21] and that the UV emission of InGaN (Fig. 3.1.2.2.1), at the high energy side of the EL spectrum (4.0V DC), was situated at 3.147 eV. The difference $\Delta E = 3.270 - 3.150 \text{ eV} = 0.120 \text{ eV}$ is originated by the band gap broadening of the InGaN/GaN QW heterostructure in accordance with Eq. (1.1.1.2.1).

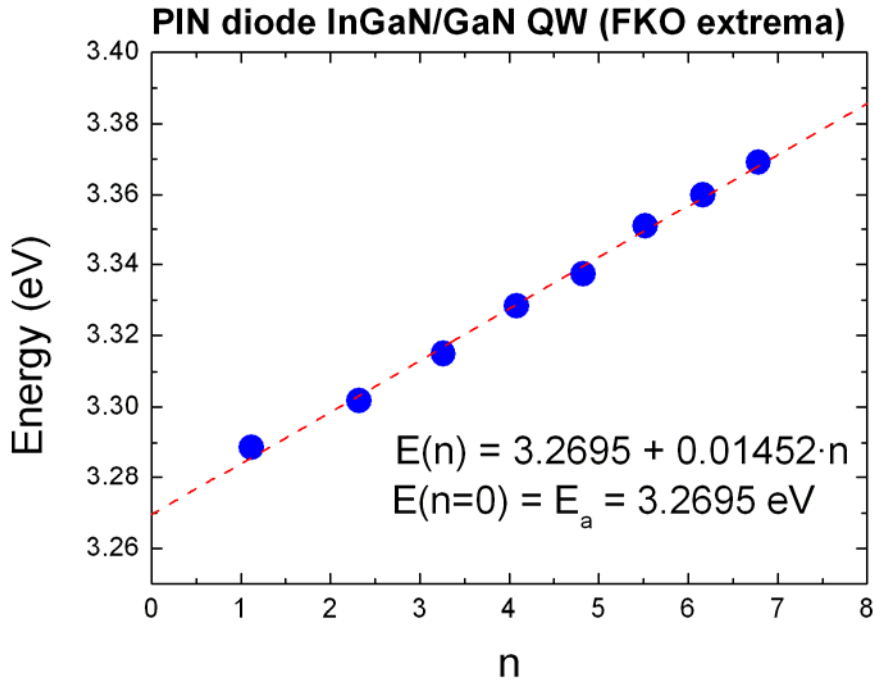


Figure 3.1.1.3.3 Linear fitting of the extrema between E_1 and E_2 for the InGaN Franz-Keldysh oscillations.

Rearranging the terms in Eq. (1.1.1.2.1) and setting $k=n\pi/d$, $n=1$, the QW width d can then be obtained with Eq. (3.1.1.3.5)

$$d = \frac{h}{\sqrt{8 \cdot m_e^* \cdot \Delta E}} \quad (3.1.1.3.5)$$

where $\Delta E = 0.120$ eV, m_e^* is the effective electron mass in $\text{In}_{0.055}\text{Ga}_{0.945}\text{N}$ set equal to $m_e^* = 0.20m_0$ in GaN [41], m_0 being the free electron rest mass $m_0 = 9.109 \cdot 10^{-31}$ kg, and $h = 6.626 \cdot 10^{-34}$ m²kg/s is Planck's constant. The calculation using Eq. (3.1.1.3.5) results in $d = 3.96$ nm which is in agreement with the thickness of the InGaN layer, Fig. 2.1.2.1, evaluated using XRD, as described in Chapter 2.1.1.1.

The slope of the linear curve $E_m(n)$ in Fig. 3.1.1.3.3 is the electro-optical energy $\hbar\Theta = 0.01452$ eV. The modulated field F of the InGaN/GaN QW heterostructure can be calculated using Eq. (3.1.1.3.6) [162]:

$$\left(\frac{h}{2 \cdot \pi} \cdot \Theta\right)^3 = \frac{q_e \cdot \frac{h}{2 \cdot \pi} \cdot F^2}{2 \cdot \mu_{\text{reduced}}} \quad (3.1.1.3.6)$$

where $q_e = 1.602 \cdot 10^{-19}$ C and $\mu_{\text{reduced}} = ((1/m_e^*) + (1/m_h^*))^{-1}$ are the elementary charge and the reduced interband mass in the direction of the field F , respectively. For the calculation, the effective mass of electrons and holes in GaN $m_e^* = 0.20m_0$ and $m_h^* = 0.80m_0$ [41] with $m_0 = 9.109 \cdot 10^{-31}$ kg, and $h = 6.626 \cdot 10^{-34}$ m²kg/s are inserted in Eq. (3.1.1.3.7).

$$F = \left[\frac{\left(\frac{h}{2 \cdot \pi} \cdot \Theta\right)^3 \cdot (2 \cdot \mu_{\text{reduced}})}{q_e \cdot \frac{h}{2 \cdot \pi}} \right]^{0.5} \quad (3.1.1.3.7)$$

Using Eq. (3.1.1.3.7), a value of $F = 0.04$ MV/cm is obtained. This value is two orders of magnitude lower than the value of the $\text{In}_{0.05}\text{Ga}_{0.945}\text{N}$ polarisation field $E_{\text{pol}} = -2.25$ MV/cm experimentally measured by CVP and one order of magnitude lower than the theoretically predicted value of $E_{\text{pol}} \approx 0.75$ MV/cm (Fig. 3.2.6.4.1). FKOs are usually related to surface/interfaces, thus barrier regions of heterojunctions, and, in this case, to the field existing at the InGaN/GaN interfaces, which is expected to be weaker than the (total) field E_{pol} .

In accordance with reference [162], the field F experienced by carriers with concentration N_{InGaN} and charge q_e across the InGaN/GaN heterojunction under application of an AC voltage $V_{\text{ac}} = 2$ V is given by

$$F^2 = \left(\frac{2 \cdot q_e \cdot N_{\text{InGaN}}}{\epsilon_{r_{\text{InGaN}}} \cdot \epsilon_0} \right) \cdot V_{\text{ac}} \quad (3.1.1.3.8)$$

$\epsilon_{r_{\text{InGaN}}} = 9.252$ [164] being the relative permittivity of the intrinsic InGaN layer and $\epsilon_0 = 8.854 \cdot 10^{-12}$ F/m the vacuum permittivity.

The carrier concentration N_{InGaN} can then be determined from Eq. (3.1.1.3.9) as:

$$N_{\text{InGaN}} = \frac{F^2 \cdot \epsilon_{r_{\text{InGaN}}} \cdot \epsilon_0}{2 \cdot q_e \cdot V_{ac}} \quad (3.1.1.3.9)$$

The calculation results in $N_{\text{InGaN}} = 1.64 \cdot 10^{15} \text{cm}^{-3}$, which is a reasonable value considering that the InGaN layer is unintentionally doped with dopant concentration typically in the range $10^{15} - 10^{16} \text{cm}^{-3}$ and that FKOs are generally seen only in this doping range [162].

3.1.1.4

InAlN/GaN PIN diode ER spectra

In the case of the InAlN/GaN samples no ER spectra were acquired. In agreement with [21] as presented in Fig. 1.1, it was to be expected that any reflectance information of InAlN spectra would be absorbed by GaN, as GaN has a much smaller band gap.

3.1.2

Electroluminescence

3.1.2.1

GaN PIN diode EL spectra

A very interesting result of the EL investigation was the vast change of the spectra by varying the DC voltage, retaining the AC voltage at 2Vp-p. A great change in the ratio of defect-related emission due to donor-acceptor pair recombination (DAP), in the visible range, to the UV emission was easily achieved using different forward biases. These results are presented for the GaN (no DHS) sample in Fig. 3.1.2.1.1. By increasing the DC voltage, an amplification of the UV component at higher photon energies was eminent as a result of the increase of the induced electric field.

The exact emission energies of the EL components in UV-VIS and VIS-NIR were obtained by fitting the EL spectra with Gaussians. In Fig. 3.1.2.1.2, the fitting of the EL spectrum of the GaN PIN diode operated at 2.4V DC and 2V AC is presented. The UV emission is composed of a high intensity component at the GaN fundamental gap energy $E_a(=E_0)=3.414\text{eV}$, with particularly narrow bandwidth (FWHM) of $\Gamma=0.054\text{eV}$, and a broader low intensity component at $E_{\text{DAP}}=3.299\text{ eV}$, $\Gamma=0.283\text{eV}$. Since on focus of this investigation is the deep UV emission component of the GaN PIN diode, a calibration of the emission spectra with respect to the sensitivity of the EL spectrometer, e.g. monochromator grating and Si diode detector, has not been considered. The intensity ratio of the UV-VIS to VIS-NIR components may thus be altered in case the spectrometer characteristics are taken into account.

**PIN diode MD9328
EL spectra of GaN QW heterostructure**

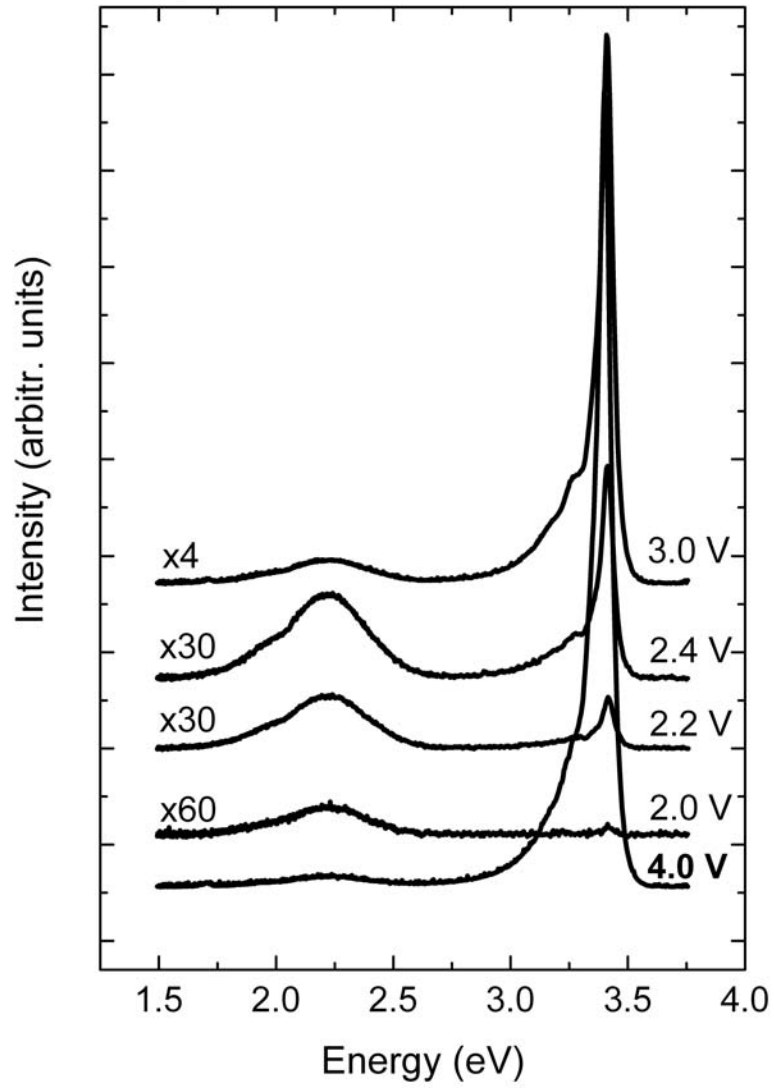


Figure 3.1.2.1.1 EL spectra of the GaN (no DHS) sample as a function of the DC voltage.

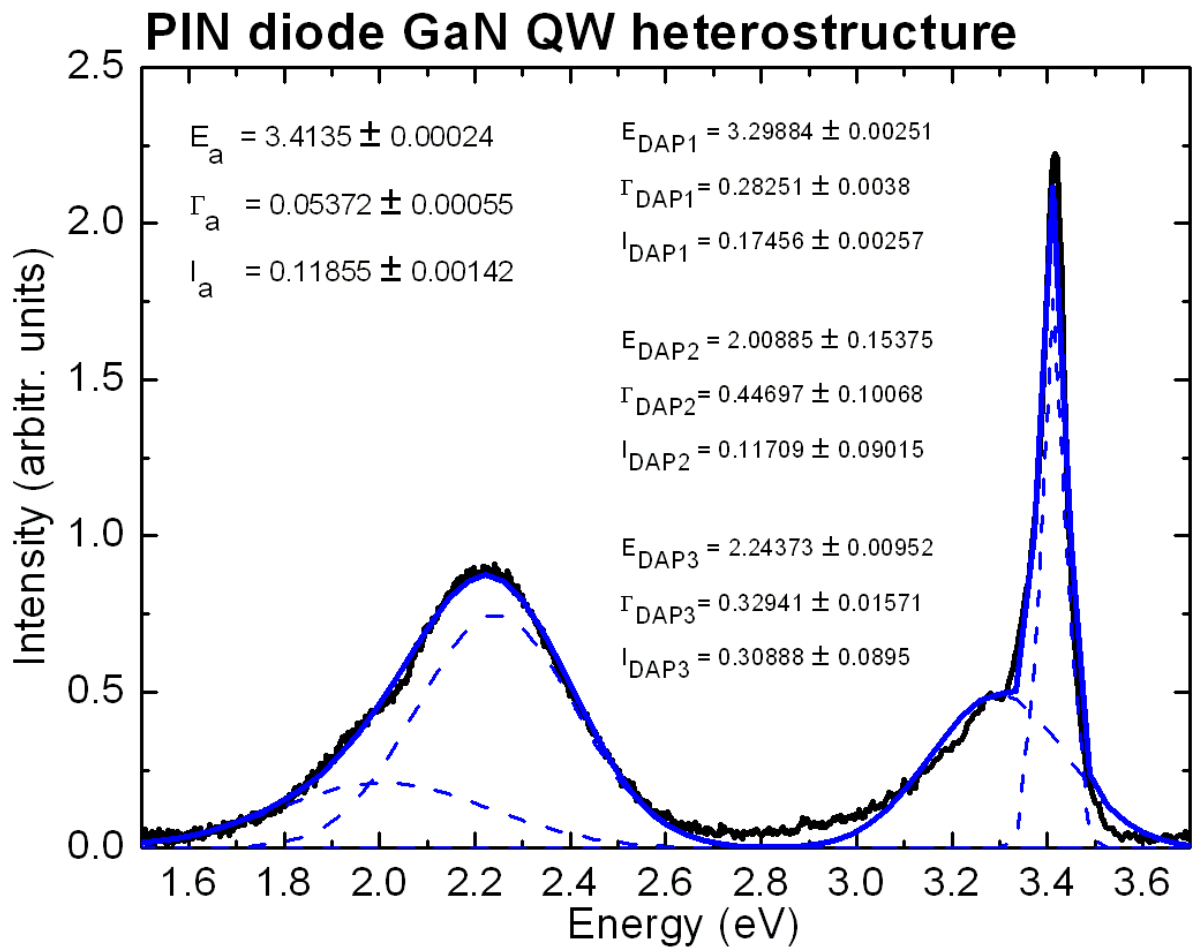


Figure 3.1.2.1.2 Fitting of the EL spectra of the GaN (no DHS) sample (2.4V DC, 2V AC) with Gaussians.

3.1.2.2

InGaN/GaN PIN diode EL spectra

Similarly to the GaN sample EL response, the InGaN sample showed the same behavior, only more complex, as a third peak, related to the $\text{In}_{0.055}\text{Ga}_{0.945}\text{N}$ band gap, in agreement with [21] as presented in Fig. 1.1 arose. Following the trend of the GaN UV component, this additional peak was also enhanced, compared to the defect-related emission as the DC voltage progressively increased.

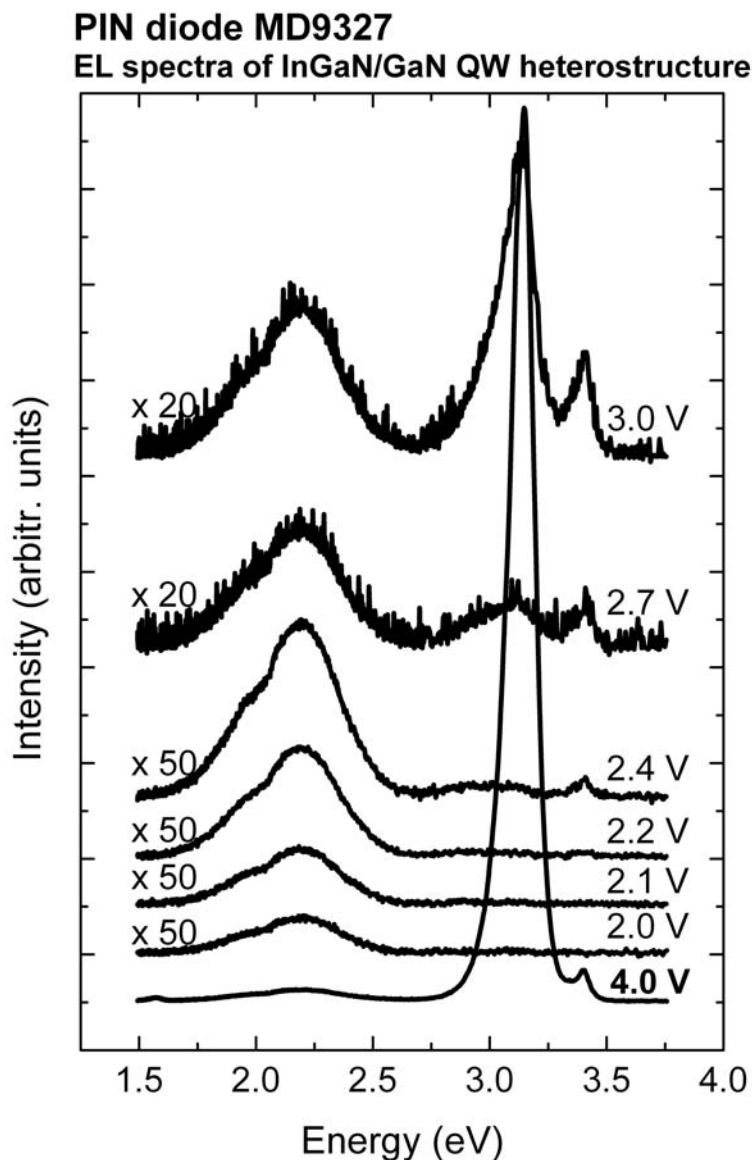


Figure 3.1.2.2.1 EL spectra of the $\text{In}_{0.055}\text{Ga}_{0.945}\text{N}/\text{GaN}$ sample as a function of the DC voltage.

3.1.2.3

InAlN/GaN PIN diode EL spectra

Again, similar to the ER spectra of Chapter 3.1.1.4, in the case of the InAlN/GaN samples no InAlN spectra were acquired. Nevertheless, the defect-related and the GaN UV emission, followed the same trend as in 3.1.2.1 and 3.1.2.2 to the change of the DC voltage shown in Figs. 3.1.2.3.1-3. In agreement with [21] as presented in Fig. 1.1, it was to be expected that any emission information of InAlN spectra would be greatly absorbed by GaN, as GaN has a much smaller band gap.

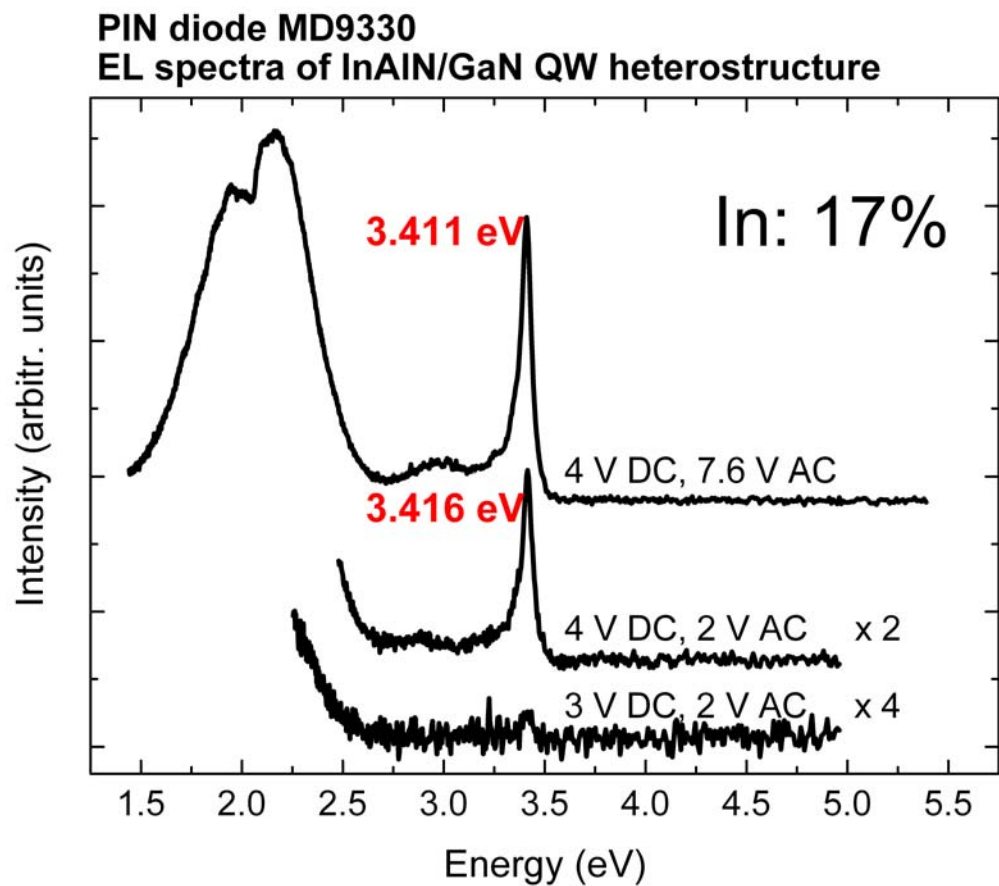


Figure 3.1.2.3.1 EL spectra of the $\text{In}_{0.17}\text{Al}_{0.83}\text{N}/\text{GaN}$ sample as a function of the DC voltage.

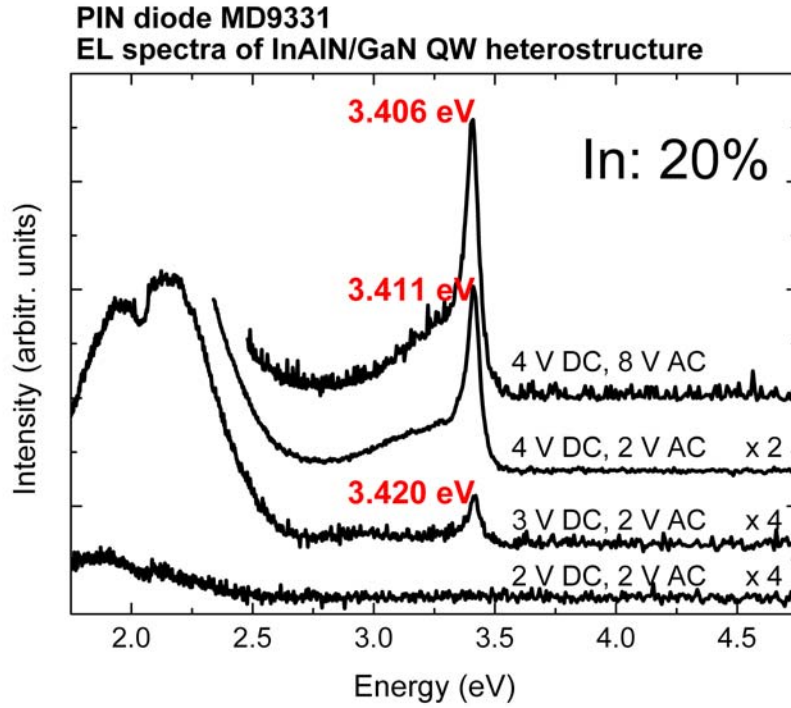


Figure 3.1.2.3.2 EL spectra of the $\text{In}_{0.20}\text{Al}_{0.80}\text{N}/\text{GaN}$ sample as a function of the DC voltage.

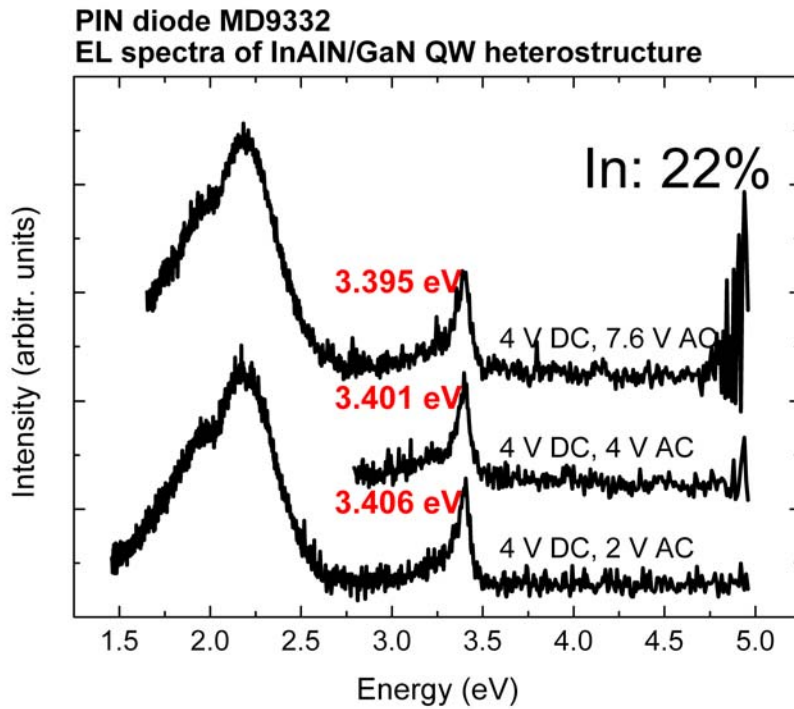


Figure 3.1.2.3.3 EL spectra of the $\text{In}_{0.22}\text{Al}_{0.78}\text{N}/\text{GaN}$ sample as a function of the DC voltage.

By comparison of the InAlN/GaN samples, at the same voltage, a red-shift with increasing Indium content is observed, as presented in Figs. 3.1.2.3.4-5.

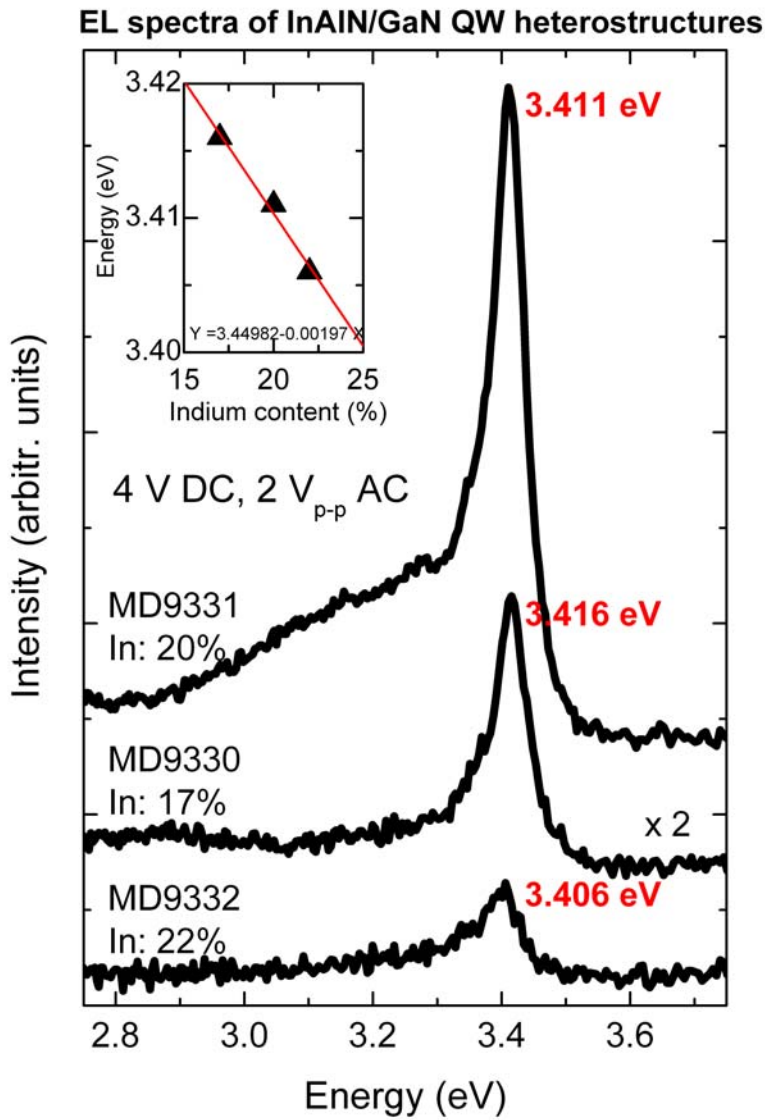


Figure 3.1.2.3.4 An EL spectra comparison between the InAlN/GaN samples for 4V DC and 2Vp-p AC.

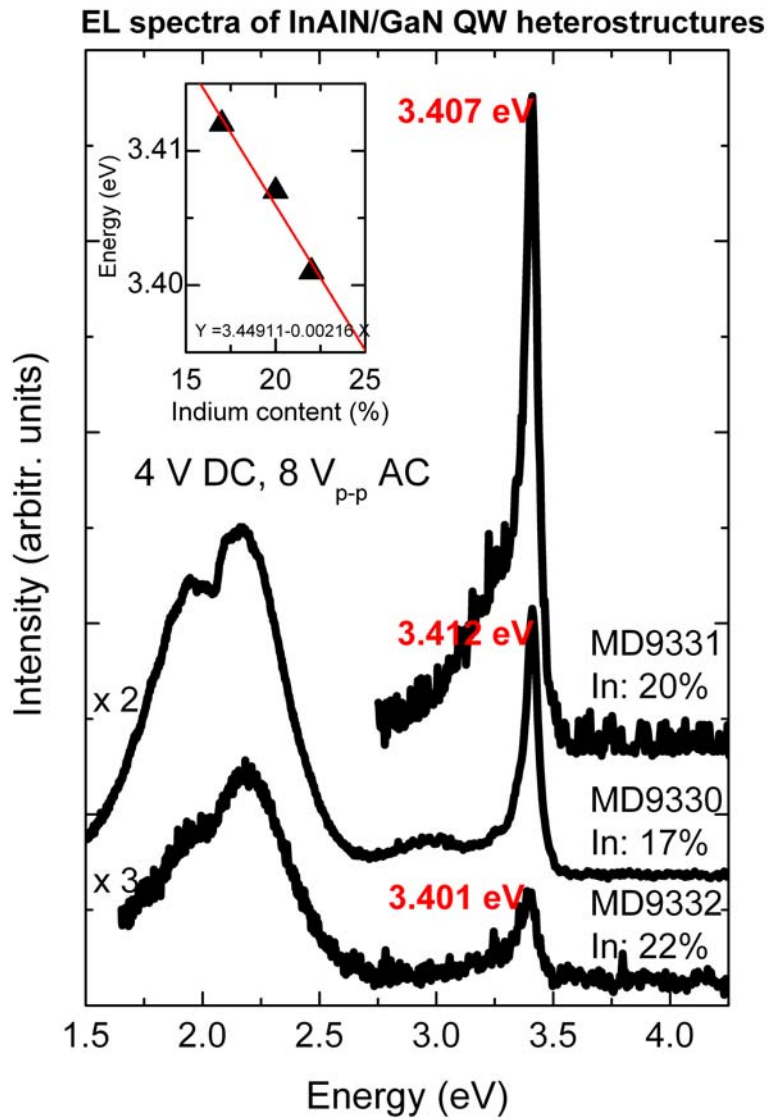


Figure 3.1.2.3.5 An EL spectra comparison between the InAlN/GaN samples for 4V DC and 8Vp-p AC.

3.2

Capacitance-Voltage Profiling

3.2.1

Conventional CVP diode equivalent circuit

As previously stated in Chapter 2.3.2, a two components option is the only one available in the modes supported by the LCR meter. Test measurements with circuits consisting of a capacitor, a series, and a parallel resistor of various values were performed in order to verify the validity of the capacitance evaluation method integrated in the LCR meter. Following that, it was profound that a new method incorporating an equivalent circuit with three components was necessary.

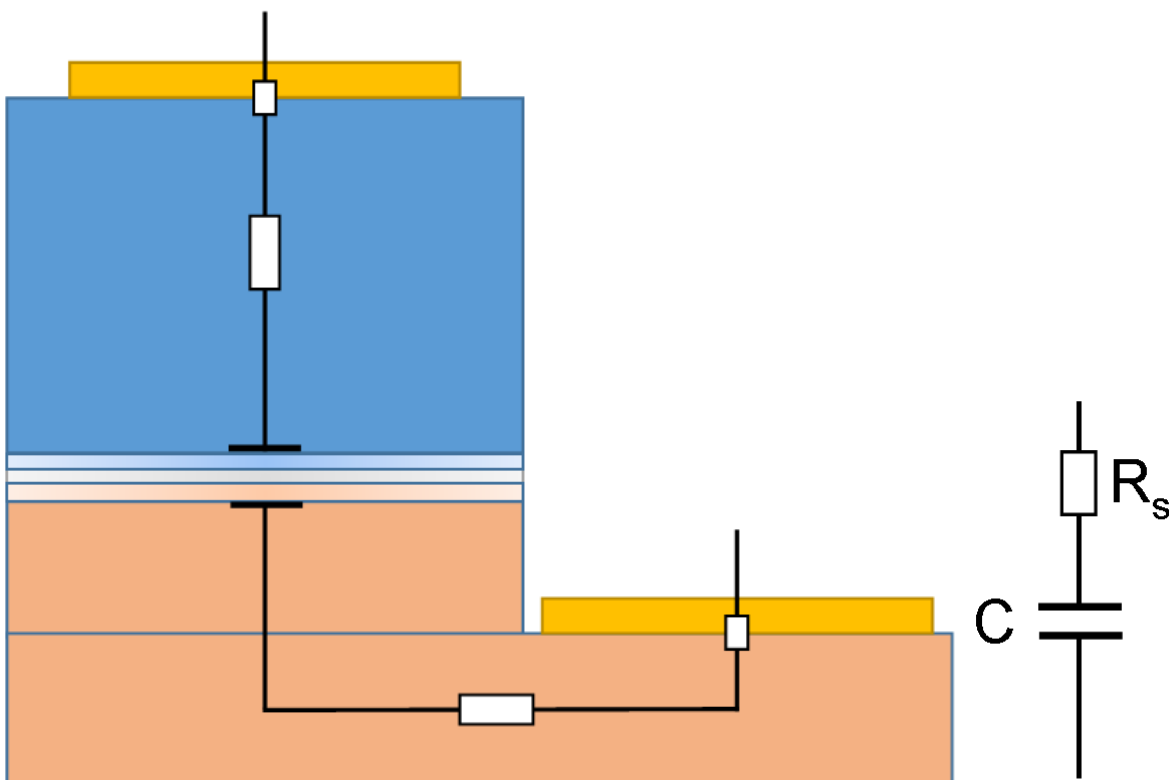


Figure 3.2.1.1 CsRs model equivalent circuit (right) and related sample structure (left).

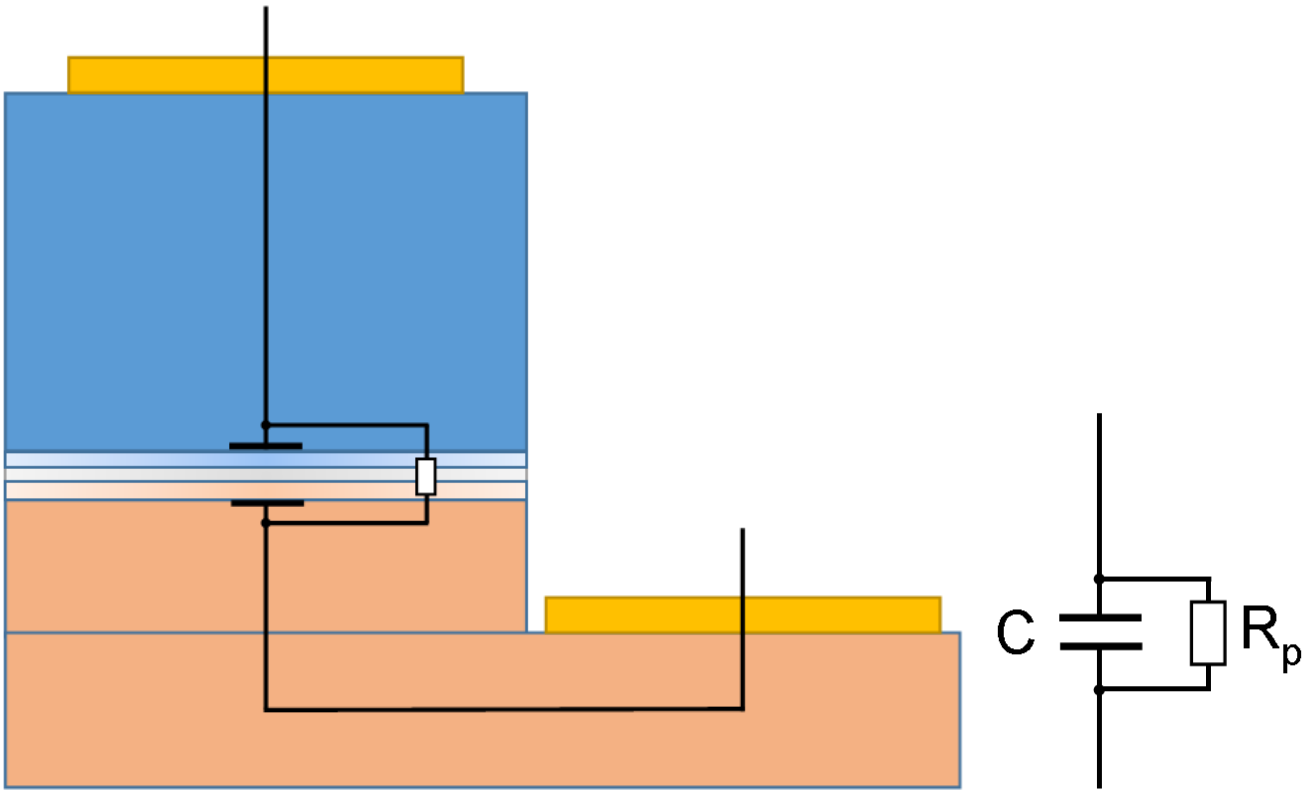


Figure 3.2.1.2 CpRp model equivalent circuit (right) and related sample structure (left).

3.2.2

Advanced CVP diode equivalent circuit

A more generalized equivalent circuit with three components relevant to the device structure was implemented. The simplest case possible was that of a circuit with a voltage dependent series resistor (1st component) in series with the parallel combination of a voltage dependent Capacitor (2nd component) and a voltage dependent resistor (3rd component). It was proven to be sufficient for most of the samples, the only exception being some cases with behaviour indicative of Electromagnetic interference at low frequencies. Since the frequency range used did not include frequencies lower than 100 Hz (Chapter 3.2.7.4), these cases could be discarded.

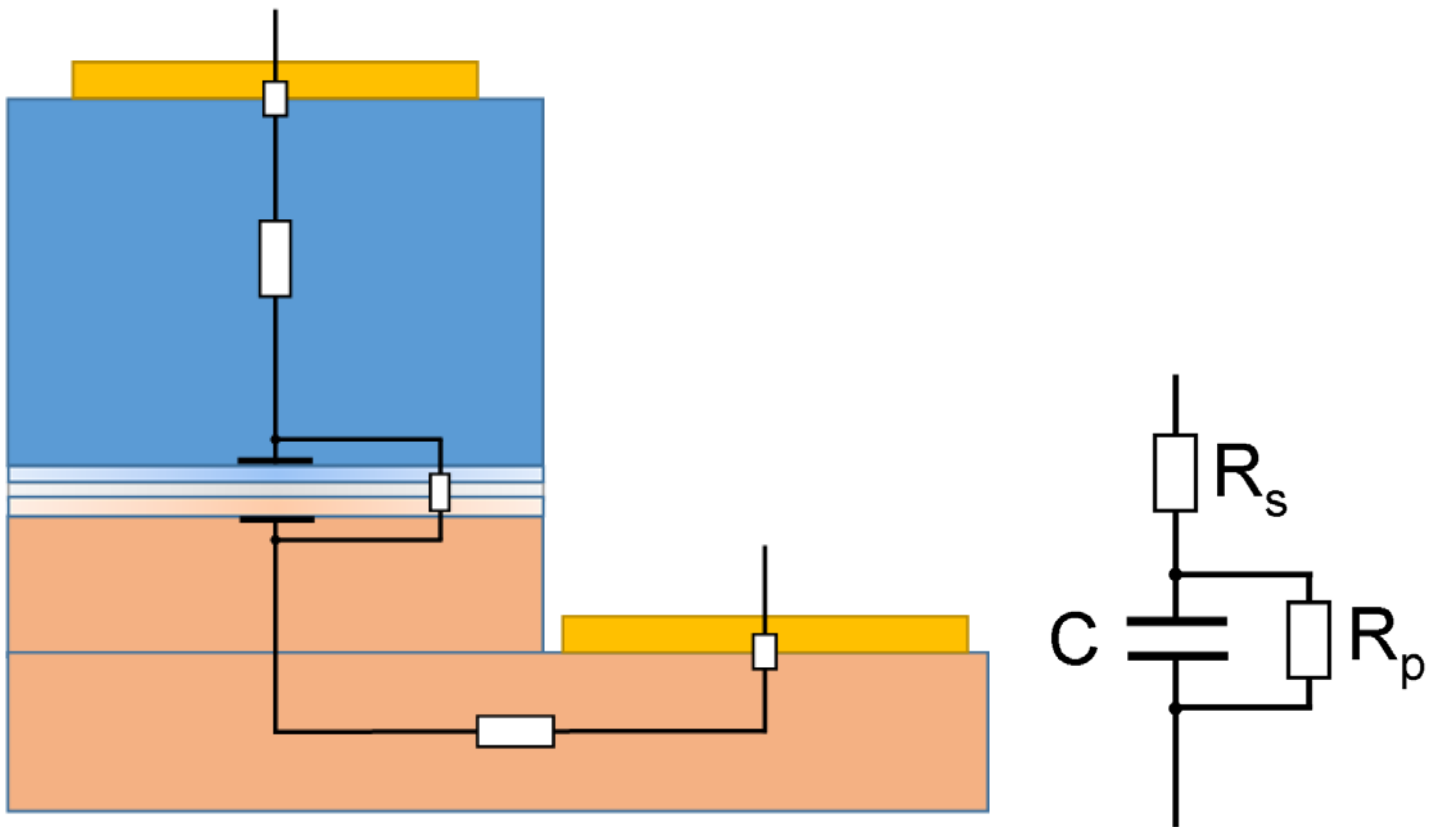


Figure 3.2.2.1 New model equivalent circuit with series and parallel resistors (right) and related sample structure (left).

3.2.2.1

Nonlinearities

The $I(V)$ of a diode in reverse bias is nonlinear, which is reflected on the series and parallel resistance being nonlinear functions of voltage. Also, the $C(V)$ of a diode is a nonlinear function.

3.2.2.2

Voltage dependence

As previously mentioned, the resistances as well as the capacitance are voltage dependent. In the calculations, this has to be dealt with extra care in addition to practical limitations.

3.2.2.2.1

$R(V)$

The dependence of the resistances on voltage is nonlinear in both forward and reverse bias. There exists a common misconception that the slope is almost constant at reverse bias, after approximately 5V, or at forward bias, after the Cut-off Voltage of the diode. This misconception arises from the fact that the $I(V)$ graph, in case of an infinite parallel resistance, is described, in the Shockley approximation, by an exponential function [67]. In a linear scale, e^x has an increasingly steeper slope, parts of which appear to be linear, though they are in fact exponential. The true nature of the absence of linearity is exposed only in a graph showing the derivative of the $I(V)$, which is also an exponential function. More than 20% change of the slope, in the range 0V - (-5V), could easily be misinterpreted and considered as a constant slope due to scaling.

3.2.2.2.2

C(V)

In principle, the CVP signal is the inverse of the square of the capacitance. Since the slope of the CVP signal is inversely proportional to the doping profile, it is linear for a constant doping and has a constant slope. In the most general case, the doping profile is unknown. Because of the unknown doping profile, it is not possible to derive an equation to calculate V_{bi} and E_{pol} as a function of the depletion region width, as explained analytically in Chapter 3.2.11.2. By comparison of the depletion region widths (w) of the (no DHS) GaN (left) and the (DHS) InGaN/GaN (right), it is apparent that a negative E_{pol} leads to the increase of w , as shown in Fig. 3.2.2.2.2.1. In accordance with Eq. (3.2.6.3.1), it is experimentally confirmed, that the InGaN/GaN sample clearly has a wider depletion region, as shown in Fig. 3.2.2.2.3. The depletion region width can be calculated from Eq. (3.2.2.2.1) using the capacitance experimental data. The dependence of the capacitance C and the $1/C^2$ on voltage are shown in Fig. 3.2.2.2.2 and Fig. 3.2.2.2.4, respectively.

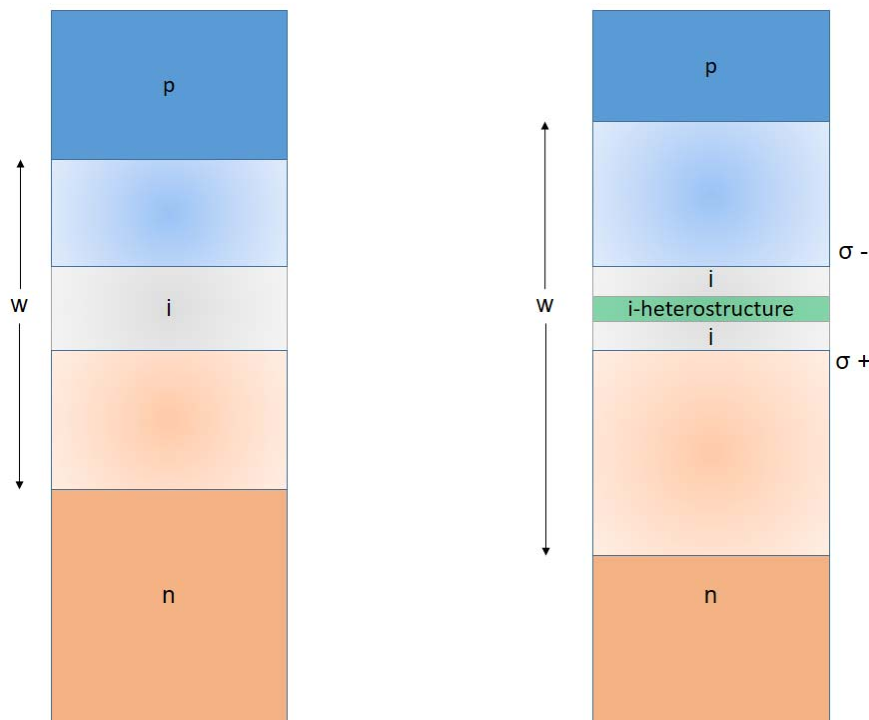


Figure 3.2.2.2.1 Comparison of the depletion region widths (w) of the (no DHS) GaN (left) and the (DHS) InGaN/GaN, a negative E_{pol} leads to the increase of the depletion region width w .

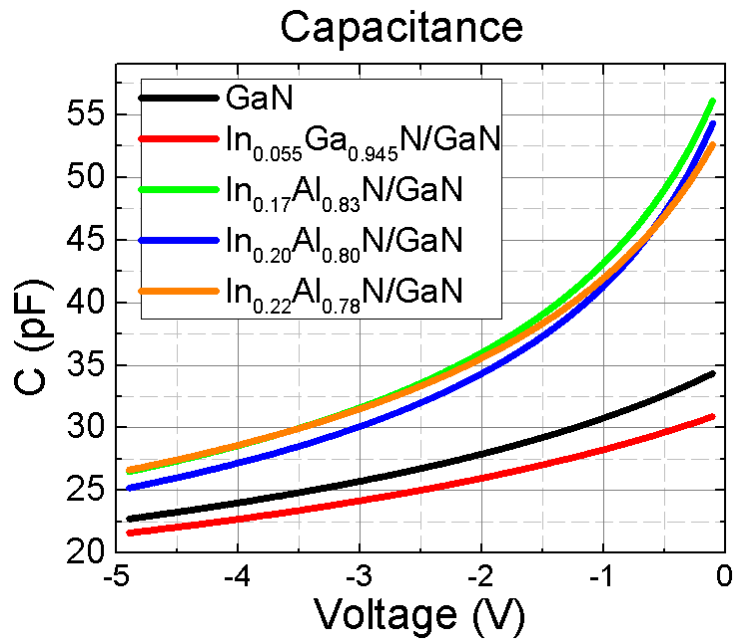


Figure 3.2.2.2.2.2 The capacitance as a function of voltage measured experimentally.

The depletion region width is conveniently calculated using Eq. (3.2.2.2.1) [68]

$$w = \frac{\varepsilon \cdot A}{C} \tag{3.2.2.2.1}$$

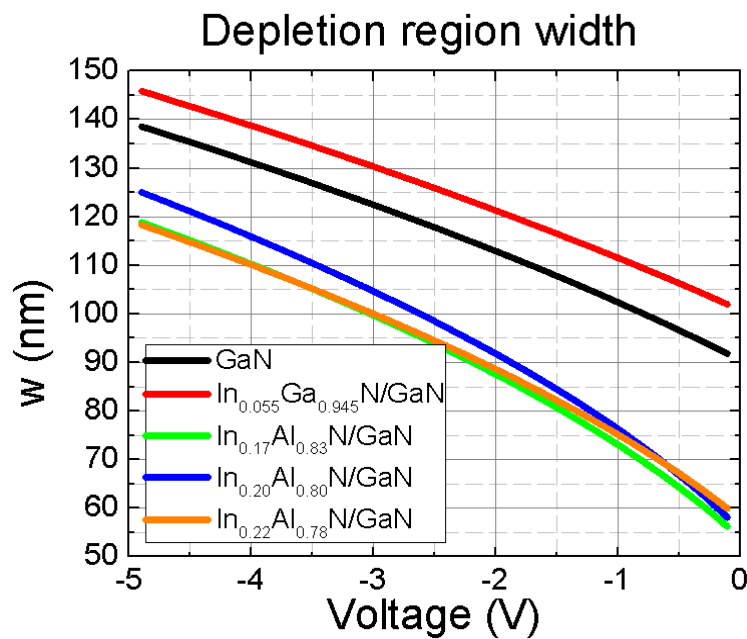


Figure 3.2.2.2.3 Depletion region width calculated using the experimentally measured capacitance.

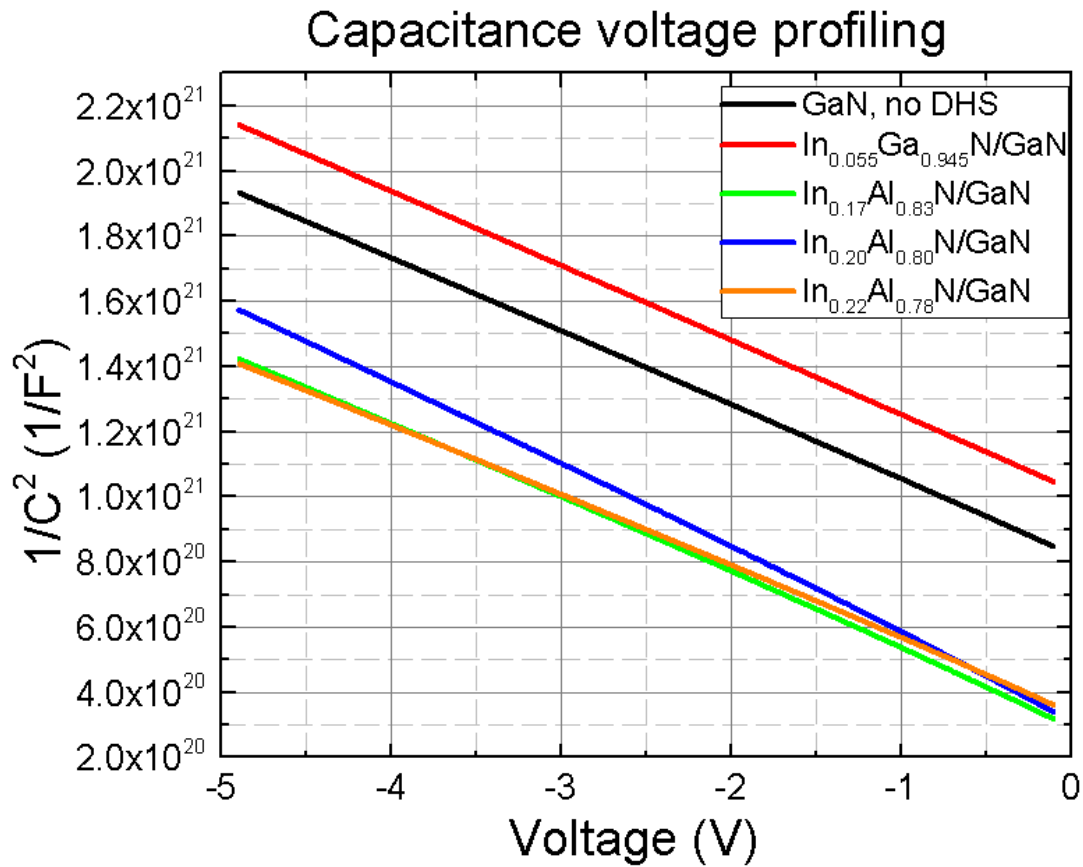


Figure 3.2.2.2.4 The typical $1/C^2(V)$ signal is linear for constant doping, as calculated using the experimentally measured capacitance.

Fig. 3.2.2.2.4 shows a close to linear behavior due to relatively low doping variation (see also Fig. 3.2.11.3.1). In principle, it is not necessary to have samples with the same doping profile, that is, the same slope, when using the analytical functions derived and presented in this work, as shown in Eq. (3.2.6.3.2) and Eq. (3.2.6.3.5).

3.2.2.3

Frequency dependence

As mentioned in Chapter 3.2.2.3, except from a possible frequency dependence of the capacitance and/or the resistances, a far greater plasmatic frequency dependence may be present, because of an insufficient equivalent circuit model. Moreover, the new method, which effectively bypasses the need for calculation of the resistances, if all components are frequency independent, further proves the independence of the capacitance on frequency, as explained in Chapter 3.2.2. If the capacitance is frequency dependent, then this dependence would be evidenced by using this method.

It has to be noted, that even though a frequency dependence would be evidenced, the capacitance values calculated would not be correct, because Eq. (3.2.3.4.9) was derived under the assumption that the resistances and the capacitance are not frequency dependent. Throughout the MD93 PIN diode series, no observable frequency dependence was present in the frequency range of 200kHz to 280kHz. Since the impedance of the capacitance is a strictly decreasing function, for lower frequencies such as 200Hz, the overall impedance may be over 4 orders of magnitude greater than that at 200kHz. This results in the SNR of the CVP being frequency dependent, since higher impedance causes lower currents, thus reducing the SNR to the point that any CVP measurement is often impossible below 50Hz. An optimum frequency range of 200kHz to 280kHz was used for the measurements.

3.2.2.4

Transient & steady state response

A frequency range where the measured group delay can have negative values is considered as being almost a steady state, as explained in Chapter 3.2.3.1.2.1. In the general case, transient phenomena, such as switching in the LCR meter internal circuits during the current and voltage measurement procedures, can alter the measurement. Measuring more than 2 properties, e.g. impedance, phase, and DC voltage, simultaneously is impossible with the used instrument. Nevertheless, various properties (DC and AC currents and voltages, and phase shift) need to be simultaneously measured and recorded. Due to limitations of the instrument measurement procedures, two properties are measured and recorded at once and the next ones slightly later. Taking into consideration that the DC and AC components may be of a completely different order of magnitude and thus need a different scale, the measurement of two properties at a time is from an engineering point of view more practical. There exist better electrical engineering options, however, there are not a common practice; the common practice is to reduce the elements needed, thus reduce the production cost.

3.2.3

Advanced method for accurate CVP

The oversimplified circuit used by the LCR meter is a two component equivalent circuit consisting of a resistor and capacitor either in series or in parallel. If a complex structure resulting in a very complicated equivalent circuit exists in the sample under investigation, advanced electronics and materials engineering is necessary. After thorough testing of the available samples, it was sufficient to increase the equivalent circuit components by one, thus have a capacitance in parallel with a resistance and this parallel combination having a resistance in series. It has to be noted, that the frequency range used has to be selected taking into consideration the limitations of the instrument which quite often render impossible the AC current measurement at frequencies below 200Hz due to a very low SNR and some frequency calibration incapacibilities of the instrument over 1.6MHz. For the samples under investigation, typical values of AC current, AC voltage, and impedance at 200Hz were 10nA rms, 0.1V rms, and 10M Ω , respectively.

3.2.3.1

Using directly measured properties

In most modern electronic systems, the property directly measured is the voltage versus time. This is the case also in the LCR instrument, where the voltage is directly measured and the current is calculated as the voltage drop across an internal resistor for each current scale. Each scale should have a resistance well below the resistance of the device under test (DUT), in order for the voltage drop across the scale resistance to be significantly smaller than the voltage drop on the DUT. A sinusoidal voltage at a selected frequency is very often used to investigate the AC properties of the DUT. It has to be noted that it should be checked, whether it is a true sinus function, as a signal resembling a sinus (e.g. a sinus to the power of three) would mean extra Fourier frequency components. This would in every case distort the measurement results.

3.2.3.1.1

Impedance

The calculated impedance of the DUT, in the steady state condition, allows the investigation of properties not directly measured. The impedance is defined as the ratio of the AC voltage to AC current. It is a complex-valued function represented by its amplitude and phase components as are the AC current and voltage. In order to calculate the capacitance, several of the directly measured properties need to be considered. This creates a calculation environment which propagates errors at each level of calculation. For example, when calculating the current, the tolerance of the internal scale resistor needs to be taken into account. The inherent error of adding a resistor is present, even though its value is many orders of magnitude less than the impedance of the DUT. Though reference samples are used to identify possible deviations from the accuracies presented in the user manuals of the instruments, a considerable amount of effort has to be invested, if one has to overcome the cases of not well documented instrumentation, insufficient product support, and practical limitations. Calibration of the LCR meter, in order to accurately measure the impedance, often leads to controversies. For example, in the frequency range of 200Hz to 1MHz, the impedance ranges from typical values of 10M Ω to 10k Ω by three orders of magnitude; calibration at each measurement point, without interrupting the measurement, is not possible, even though it would be necessary to calibrate at least once per order of impedance magnitude in order to increase the accuracy of the measurement. Interrupting the measurement is also not recommended as it induces transient effects.

3.2.3.1.2

Phase

Another important property directly measured is the phase over the used frequency range, that is, the phase response. The phase response, combined with the impedance response is used to calculate the capacitance. It is defined as the time delay of the current in the event of a voltage input multiplied by the frequency and expressed in radians. The frequency output of the signal generator was verified using an oscilloscope.

3.2.3.1.2.1

Group delay

Group delay is defined as the negative of the slope of the phase response. An important check is, whether the calculated group delay is negative or not. A negative delay is plasmatic as the output cannot precede the input. This should not be confused with the case of a negative phase, as the voltage input could be preceding the current output in a periodical meaning, e.g. converting 350 degrees to -10 degrees. Nevertheless, a calculated negative group delay can occur both in theoretical calculations and experiment. This can be explained as follows: At a frequency where the group delay is negative, the steady-state condition no longer holds [163]. Nevertheless, assuming a steady-state condition and calculating the capacitance does not induce a significant error, even if the group delay is negative.

3.2.3.2

Contacts mapping

Accurate mapping of the surface, even if the sample has no contacts, is essential in reproducing measurements and results. It is very often the case that documentation of the exact area or contacts used is completely absent or inadequately reported using notations such as "middle part", "centre", "upper", etc. This is absolutely insufficient, because it creates uncertainties about the measurements and the samples. Since the samples used had a contact grid, a column and row notation was used after taking a photo of the sample. Very often the samples have thousands of contacts and various structures such as TLM (Transmission Line Measurement), transparent, semi-transparent, non transparent types. A more systematic approach can easily reveal systematic incidents. Figs. 2.1.2.3-7 present such a mapping and Fig. 3.2.6.3.3 reveals such a trend of radial increase of dopant concentration.

3.2.3.3

Labview program

Due to the lack of compatible software to control the instrument through the PC, a custom program had to be created even though environments for creating a compatible program existed. Labview was chosen as the programming environment.

3.2.3.4

Advanced method equations

Instead of using the LCR instrument built-in method for the capacitance measurement, a new method was gradually developed in order to overcome incapacibilities of the built-in methods (Chapter 2.3.2.2). The equivalent circuit used is depicted in Fig. 3.2.2.1. The Fourier transform of this circuit is used, which is the conventional practice, when handling circuits that include more types of passive elements than only resistors. The impedance Z_C of the capacitor C is given in dependence of the angular frequency ω :

$$Z_C(\omega) = \frac{1}{i \cdot \omega \cdot C} \quad (3.2.3.4.1)$$

The impedance Z of the overall circuit is given by:

$$Z = R_s + \frac{1}{\frac{1}{R_p} + \frac{1}{Z_C}} \quad (3.2.3.4.2)$$

where R_s is the series and R_p the parallel resistance.

The measured impedance is the absolute value of the complex impedance:

$$Z_{\text{measured}}(\omega) = |Z(i \cdot \omega)| \quad (3.2.3.4.3)$$

The overall impedance can also be written in the form of:

$$Z = Z_{\text{measured}} \cdot e^{i \cdot \arg(Z)} \quad (3.2.3.4.4)$$

The phase is given by:

$$\phi = \arg(Z) \quad (3.2.3.4.5)$$

and the Group delay given by:

$$\text{GroupDelay}(\omega) = -\frac{d}{d\omega} \phi(\omega) \quad (3.2.3.4.6)$$

The overall impedance is now a complex-valued function represented in:

$$Z(\omega) = \left(R_S + \frac{\frac{1}{R_p}}{\frac{1}{R_p^2} + \omega^2 \cdot C^2} \right) + i \cdot \left[\frac{-(\omega \cdot C)}{\frac{1}{R_p^2} + \omega^2 \cdot C^2} \right] \quad (3.2.3.4.7)$$

Converting ω to $2\pi f$ and f to 10^L ($L = \log(f)$) and rearranging the terms of Eq. (3.2.3.4.7) results in:

$$\frac{-(10^L)}{2 \cdot \pi \cdot \text{Im}(Z(L))} = \frac{1}{4 \cdot \pi^2 \cdot C \cdot R_p^2} + C \cdot (10^{2 \cdot L}) \quad (3.2.3.4.8)$$

Eliminating the resistance terms using the first order derivative of the above equation results in the final equation for the calculation of the capacitance in the new method, as shown in Eq. (3.2.3.4.9):

$$C = \frac{\frac{d}{dL} \left(\frac{-10^L}{2 \cdot \pi \cdot \text{Im}(Z(L))} \right)}{\frac{d}{dL} (10^{2 \cdot L})} \quad (3.2.3.4.9)$$

In this equation, the Imaginary part is conveniently calculated through:

$$\text{Im}(Z) = |Z| \cdot \sin(\phi) \quad (3.2.3.4.10)$$

The need for calculating the resistances has been successfully eliminated and directly measured properties are used, without the need to evaluate the resistances first and then solve the overall impedance function with respect to C . This new model (three components circuit, Fig. 3.2.2.1) and new method for calculating the capacitance (Eq. (3.2.3.4.9)) using directly measured properties ($Z = V_{AC}/I_{AC}$, ϕ), reduces the relative error by a factor of 3 compared to the simplified models (Figs. 3.2.1.1-2), as explained in Chapter 2.3.2.2.

3.2.4

Parasitic Schottky contacts impedance

The ideal behaviour of metal contacts at the metal-semiconductor interface of diodes is purely ohmic. The TLM structures on the samples are just a doped semiconductor material (either p or n) between two metal contacts. After performing I(V) measurements on the TLM structures, a Schottky contact behaviour was confirmed. This was observed on every sample, for at least one of the two semiconductor type structures (either p-TLM or n-TLM). Additionally, they were confirmed to have a capacitance. This capacitance was maximally one order of magnitude different than that related to the depletion region. Nevertheless, the impact of this Capacitance on the overall measurement is negligible, as described in Chapter 3.2.5.

3.2.5

Theoretical verification of CVP linearity

A theoretical model was proposed using values as close as possible to the measurements including attributes such as the nonlinear voltage dependence of the capacitance. Moreover, the voltage dependence of the resistances was modelled and the series and parallel resistances were added, as shown in Fig. 3.2.2.1. The most challenging property of the circuit is its voltage divider nature, which means that the capacitance and the resistances of the diode are dependent on the voltage drop across them and not on the voltage applied to the contacts, as the contacts have a parasitic voltage drop of their own. The nonlinearity of the Schottky contacts was not necessary to be modelled as it was always 3 orders of magnitude lower than the overall impedance of the diode, the diode being always in reverse bias. All these contributions have no eminent effect on the linearity of the CVP signal (in the constant doping approximation) of the equivalent circuit. It has to be noted, that even for these few approximated circuit elements, the equations were so complicated that most of the times appropriate mathematical programming was necessary in order to calculate the properties in a reasonable amount of time.

3.2.6

Calculation of the Polarization Fields

One of the biggest uncertainties for calculating E_{pol} with Eq. (3.2.6.3.5) and V_{bi} with Eq. (3.2.6.3.2), is the relative permittivity. Values referred in [97] and [164], for example, have a variation of approximately $\pm 13\%$, which is greater than the error of the CVP measurement. The use of the LCR meter for the voltage measurement of the instructed (by the program) voltage and TEM measurements for the thicknesses introduce relative errors well beyond the relative permittivity variation. It also has to be noted, that deviation from the constant doping profile is present.

3.2.6.1

Measurements analysis

For the determination of E_{pol} selecting diodes with a doping profile with the least variation in dopant concentration is the only prerequisite, as described in Chapter 3.2.6.3. For the selected contacts in MD93 PIN diode series, an approximate 15% variation in dopant concentration within the 5V range of the CVP was evidenced, as shown in Fig. 3.2.11.3.1.

3.2.6.2

Theoretical values & equations

Theoretical values for E_{pol} were calculated using piezoelectric polarization constants and theoretical models, as presented in [1], [2], [97], [164], and [165]. Note that even using the same lattice, deformation, and strain constants, different E_{pol} values can be calculated due to various models. With the Indium content of the nitride material systems as a variable, Ref. [164] uses linear interpolation between the lattice, deformation, and strain constants, and then calculates the piezoelectric polarization resulting into a fraction of 2nd degree polynomials. Ref. [97] calculates the piezoelectric polarization for InN, AlN, and GaN using a linear interpolation between the lattice constants and then interpolates using a bowing parameter, ultimately resulting into a 2nd degree polynomial of the Indium content. These works used linear interpolation for the spontaneous polarization constants. For comparison purposes, the same relative permittivities were used for the calculation of the values depicted in Figs. 3.2.6.2.1-3.

Since the polarization fields are determined using CVP, additional emphasis has to be given in the definition of the positive electric field direction. The forward bias is defined as positive and the growth direction (normal to the c-plane) is considered relative to the voltage polarity as the sample, in principle, could be placed in any direction relative to the applied voltage. An overall sign change in Eqs. (3.2.6.2.2-6) had to be made with respect to Refs. [1], [2] [97], [164], and [165], in order to keep the forward bias being defined as positive.

The interpolation between the corresponding values of the binary materials of any given property Y was calculated using [97]:

$$Y_{\text{In}_x\text{A}_{1-x}\text{N}} = Y_{\text{InN}} \cdot x + Y_{\text{AN}} \cdot (1 - x) + b \cdot x \cdot (1 - x) \quad (3.2.6.2.1)$$

where the Y terms are any given property, for example the relative permittivity, x is the Indium content, N is nitrogen, A is In, Ga or Al, and b is an optional bowing parameter. For b=0, the interpolation is linear.

The theoretical E_{pol} for the binary materials is calculated with:

$$E_{\text{pol}_{\text{AN}}} = \frac{1}{\epsilon_0 \cdot (\epsilon_{r_{\text{AN}}} - 1)} \cdot \left[(p_{\text{sp}_{\text{AN}}} + p_{\text{pz}_{\text{AN}}}) - (p_{\text{sp}_{\text{GaN}}} + p_{\text{pz}_{\text{GaN}}}) \right] \quad (3.2.6.2.2)$$

where p_{sp} and p_{pz} denote the spontaneous and piezoelectric polarization, respectively, and ϵ_0 and ϵ_r are the vacuum and relative permittivity, respectively.

$$p_{\text{sp}_{\text{AN}}} = 2 \cdot \left(\frac{\alpha_{\text{GaN}}}{\alpha_{\text{AN}}} - 1 \right) \cdot \left(e_{31_{\text{AN}}} - e_{33_{\text{AN}}} \cdot \frac{C_{13_{\text{AN}}}}{C_{33_{\text{AN}}}} \right) \quad (3.2.6.2.3)$$

where C are the elastic stiffness constants, e are the piezoelectric coefficients, and α are the respective lattice constants. For the ternary material systems, $\text{In}_x\text{Ga}_{1-x}\text{N}$ and $\text{In}_x\text{Al}_{1-x}\text{N}$, as commented above, E_{pol} is calculated either by:

$$E_{\text{pol}_{\text{In}_x\text{A}_{1-x}\text{N}}} = E_{\text{pol}_{\text{InN}}} \cdot x + E_{\text{pol}_{\text{AN}}} \cdot (1 - x) + b \cdot x \cdot (1 - x) \quad (3.2.6.2.4)$$

or

$$E_{\text{pol}_{\text{In}_x\text{A}_{1-x}\text{N}}} = \frac{1}{\epsilon_0 \cdot (\epsilon_{r_{\text{In}_x\text{A}_{1-x}\text{N}}} - 1)} \cdot \left[(p_{\text{sp}_{\text{In}_x\text{A}_{1-x}\text{N}}} + p_{\text{pz}_{\text{In}_x\text{A}_{1-x}\text{N}}}) - (p_{\text{sp}_{\text{GaN}}} + p_{\text{pz}_{\text{GaN}}}) \right] \quad (3.2.6.2.5)$$

where

$$p_{sp_{\text{In}_x\text{Al}_{1-x}\text{N}}} = 2 \cdot \left(\frac{\alpha_{\text{GaN}}}{\alpha_{\text{In}_x\text{Al}_{1-x}\text{N}}} - 1 \right) \cdot \left(e_{31_{\text{In}_x\text{Al}_{1-x}\text{N}}} - e_{33_{\text{In}_x\text{Al}_{1-x}\text{N}}} \cdot \frac{c_{13_{\text{In}_x\text{Al}_{1-x}\text{N}}}}{c_{33_{\text{In}_x\text{Al}_{1-x}\text{N}}}} \right) \quad (3.2.6.2.6)$$

The calculation results are presented in three graphs as follows: One using Eq. (3.2.6.2.5) ($b=0$) and values from [164], one using Eq. (3.2.6.2.5) ($b=0$) and complementary values from [2] and [165], and one using Eq. (3.2.6.2.4) and values from [97] and the bowing parameters therein. For comparison purposes, all approaches use the same relative permittivities values from [164]. A comparison between all the theoretically calculated E_{pol} curves is included in Fig. 3.2.6.4.1 for $\text{In}_x\text{Al}_{1-x}\text{N}/\text{GaN}$ and in Fig. 3.2.6.4.2 for $\text{In}_x\text{Ga}_{1-x}\text{N}/\text{GaN}$.

In_xAl_{1-x}N/GaN Internal Polarization fields

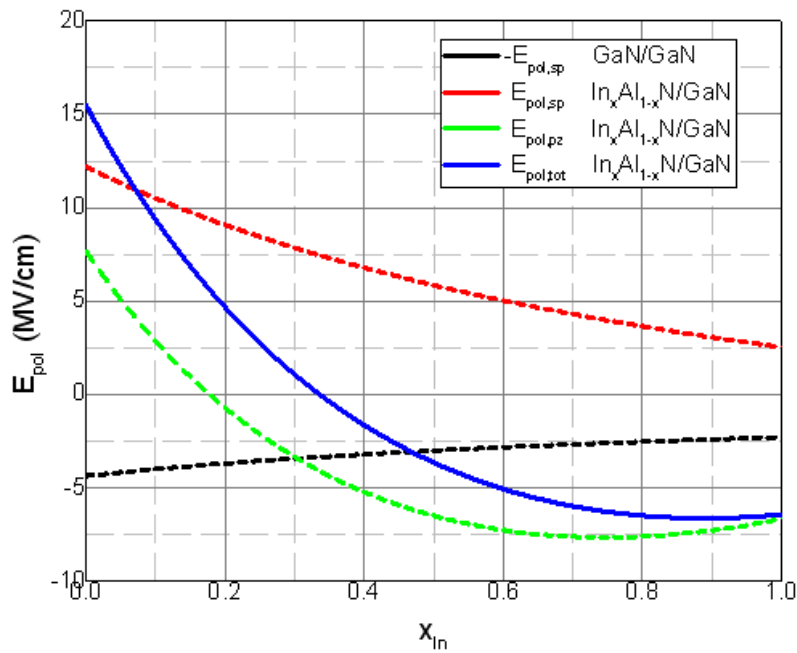


Figure 3.2.6.2.1 Theoretically calculated E_{pol} (blue) and its components for In_xAl_{1-x}N/GaN using Eq. (3.2.6.2.5) ($b=0$) and values from [164].

In_xGa_{1-x}N/GaN Internal Polarization fields

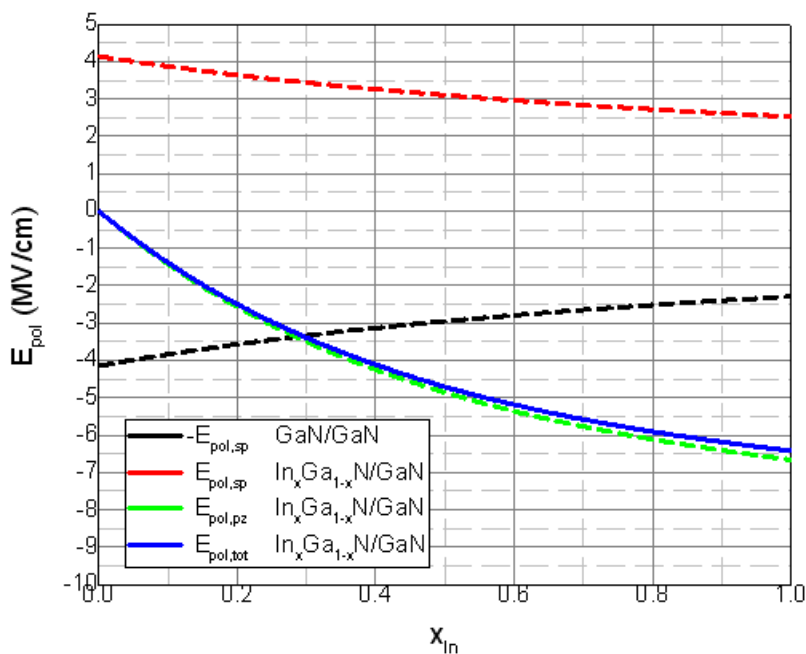


Figure 3.2.6.2.2 Theoretically calculated E_{pol} (blue) and its components for In_xGa_{1-x}N/GaN using Eq. (3.2.6.2.5) ($b=0$) and values from [164].

In_xAl_{1-x}N/GaN Internal Polarization fields

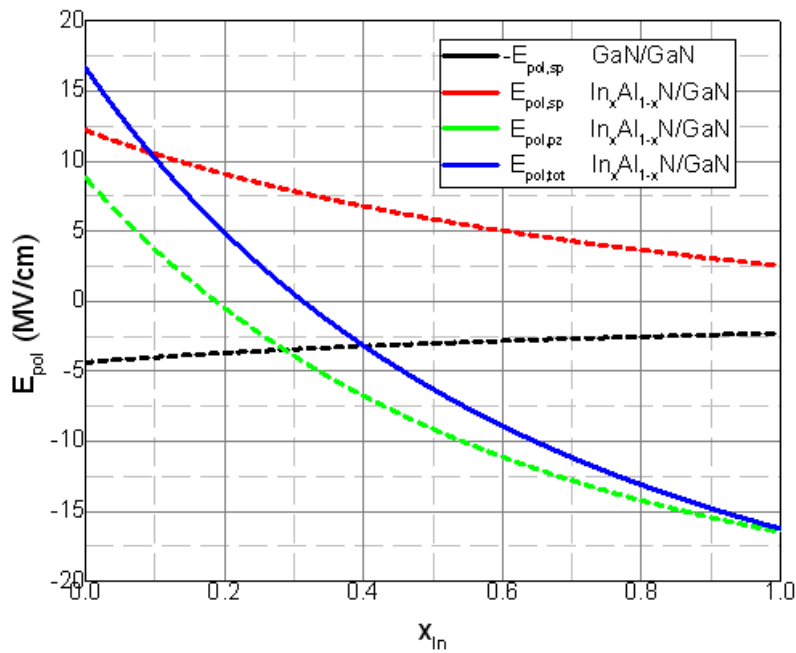


Figure 3.2.6.2.3 Theoretically calculated E_{pol} (blue) and its components for $In_xAl_{1-x}N/GaN$ using Eq. (3.2.6.2.5) ($b=0$) and complementary values from [2] and [165].

In_xGa_{1-x}N/GaN Internal Polarization fields

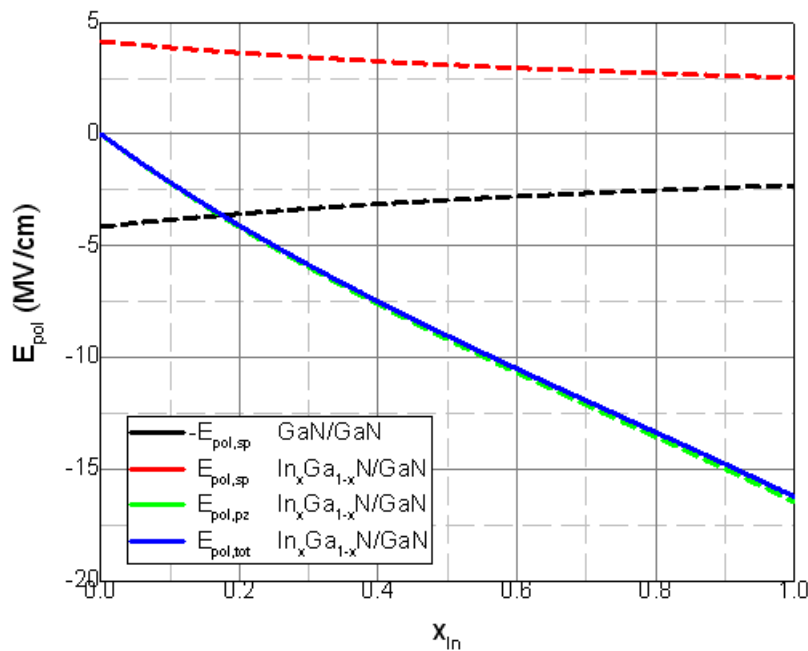


Figure 3.2.6.2.4 Theoretically calculated E_{pol} (blue) and its components for $In_xGa_{1-x}N/GaN$ using Eq. (3.2.6.2.5) ($b=0$) and complementary values from [2] and [165].

In_xAl_{1-x}N/GaN Internal Polarization fields

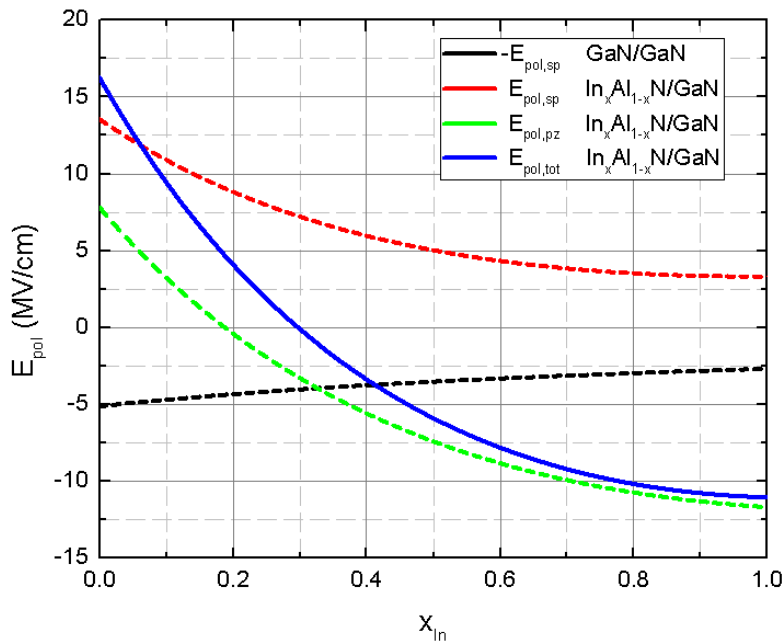


Figure 3.2.6.2.5 Theoretically calculated E_{pol} (blue) and its components for In_xAl_{1-x}N/GaN using Eq. (3.2.6.2.4) and values from [97] and the bowing parameters therein.

In_xGa_{1-x}N/GaN Internal Polarization fields

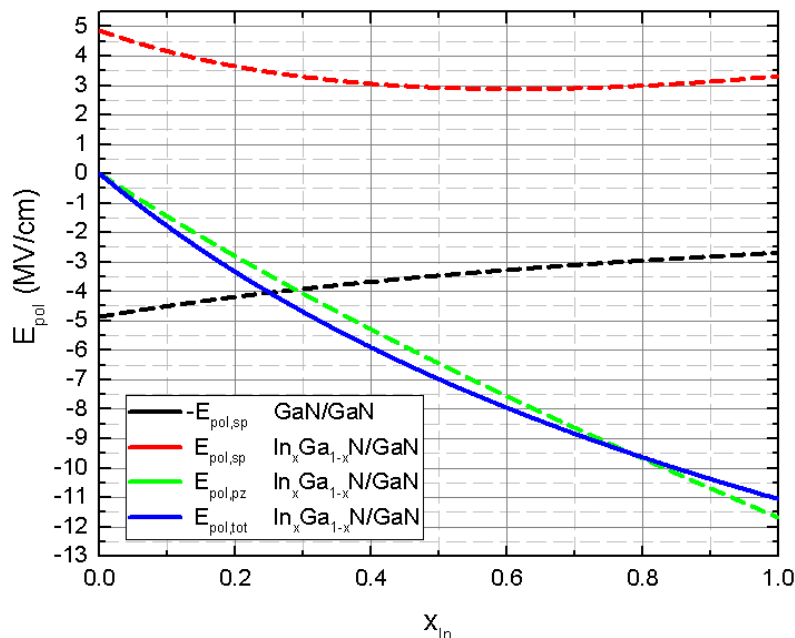


Figure 3.2.6.2.6 Theoretically calculated E_{pol} (blue) for In_xGa_{1-x}N/GaN and its components using Eq. (3.2.6.2.4) and values from [97] and the bowing parameters therein.

3.2.6.3

Experimental values & equations

For the constant doping approximation, Eq. (3.2.6.3.1) [148] can be used:

$$w^2 = d_u^2 + \frac{2 \cdot \epsilon}{q} \cdot \left(\frac{1}{N_A} + \frac{1}{N_D} \right) \cdot (V_{bi} - E_{pol} \cdot d_{DHS} - V) \quad (3.2.6.3.1)$$

where V_{bi} is the built-in potential, d_u is the total thickness of the intrinsic layers, d_{DHS} the thickness of the middle intrinsic layer in the case of a DHS, $\epsilon = \epsilon_0 \cdot \epsilon_r$, q is the elementary charge, N_A and N_D are the acceptor and donor dopant concentrations, respectively, and V is the induced voltage.

Solving Eq. (3.2.6.3.1) for $E_{pol}=0$, in the case of the GaN sample, where no piezoelectric polarization is present, assuming a non zero intrinsic doping, and incorporating the temperature term, which is present in [68], results in Eq. (3.2.6.3.2) for V_{bi} . Note that in Eq. (3.2.6.3.1), a negative E_{pol} increases w .

$$V_{bi} = \left[\frac{d_u^2}{\epsilon^2 \cdot A^2 \cdot \frac{d}{dV} \left(\frac{1}{C(V)^2} \right)} \right] \cdot \left(1 + \frac{N_i}{N_A} - \frac{N_i}{N_D} - \frac{N_i^2}{N_A \cdot N_D} \right) - \frac{\left(\frac{1}{C(V)^2} \right)}{\frac{d}{dV} \left(\frac{1}{C(V)^2} \right)} + V + \frac{2 \cdot k_B \cdot T}{q} \quad (3.2.6.3.2)$$

N_i is the unintentional dopant concentration for the intrinsic layers, A is the p-contact area (effectively being the diode surface area), k_B is the Boltzmann constant, and T is the temperature in Kelvin. Eq. (3.2.6.3.2) is derived through a constant doping approximation, utilizing Eq. (3.2.6.3.3-4):

$$\Phi(x) = -\frac{q}{\epsilon} \cdot \int_0^x \int_0^r N(u) du dr \quad (3.2.6.3.3)$$

$$V_{bi} = \Phi(w) \quad (3.2.6.3.4)$$

where Φ is the potential, x is the length direction across the layer sequency, N is the dopant concentration as a function of x , and u and r are integration variables and Eq. (3.2.6.3.4). Following a similar approach, E_{pol} is calculated by:

$$E_{pol} = \frac{1}{d_{DHS}} \left[V_{bi} - \frac{d_u^2}{\varepsilon^2 \cdot A^2 \cdot \frac{d}{dV} \left(\frac{1}{C(V)^2} \right)} \cdot \left(1 + \frac{N_i}{N_A} - \frac{N_i}{N_D} - \frac{N_i^2}{N_A \cdot N_D} \right) + \frac{\left(\frac{1}{C(V)^2} \right)}{\frac{d}{dV} \left(\frac{1}{C(V)^2} \right)} - V - \frac{2 \cdot k_B \cdot T}{q} \right] \quad (3.2.6.3.5)$$

Note that the terms of Eq. (3.2.6.3.5) now refer to the DHS samples and that only V_{bi} refers to and includes all the necessary terms of the GaN sample, as shown in Eq. (3.2.6.3.2).

Calculating using Eq. (3.2.6.3.2) and Eq. (3.2.6.3.5) resulted in slightly voltage dependent V_{bi} and E_{pol} . Since all equations are derived close to equilibrium, thus at 0V [68], the V_{bi} and E_{pol} values at 0V (which is the y-axis intercept of the linear fitting in Figs. 3.2.6.3.1-2) were selected as the calculated values for V_{bi} and E_{pol} . The entire voltage range and this dependence are shown in Figs. 3.2.6.3.1-2.

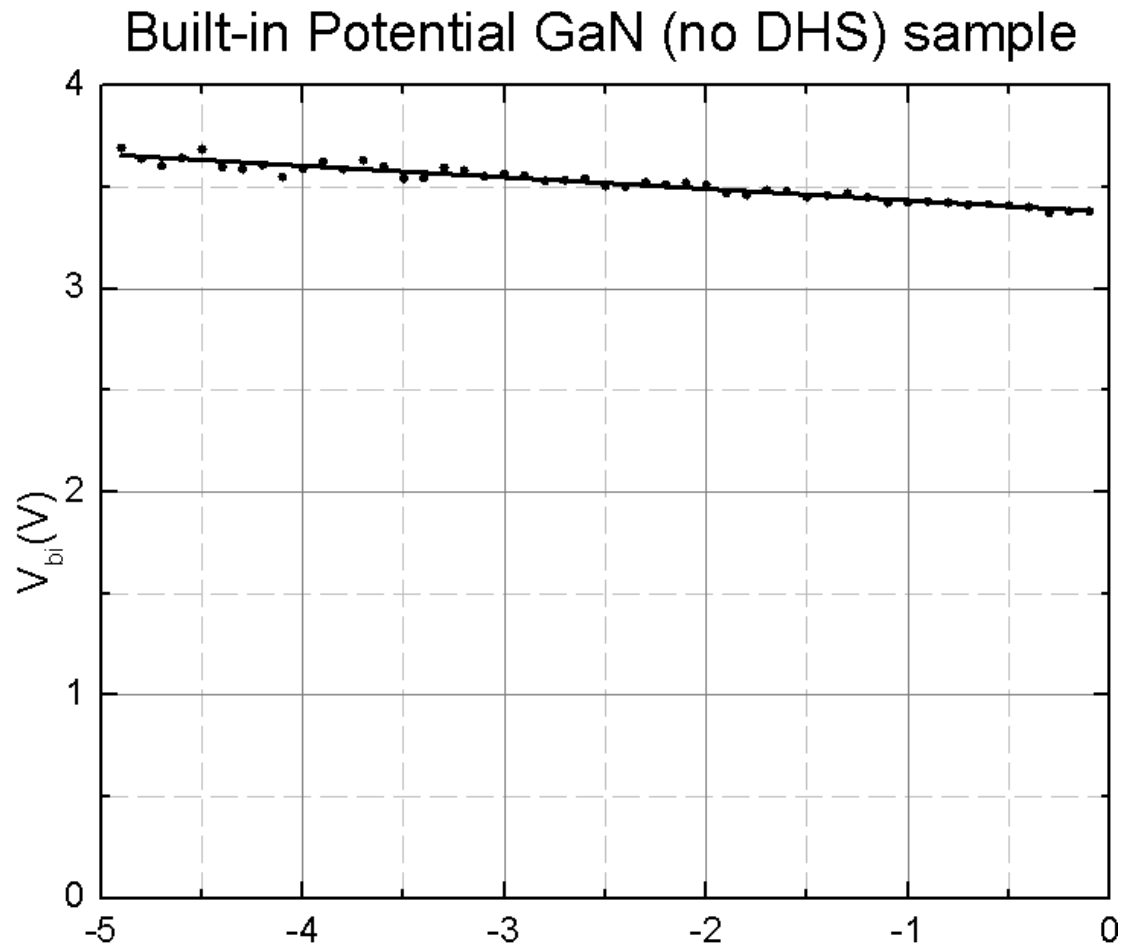


Figure 3.2.6.3.1 Calculation of V_{bi} , using Eq. (3.2.6.3.2) and selection of the value that refers to 0V.

Polarization field

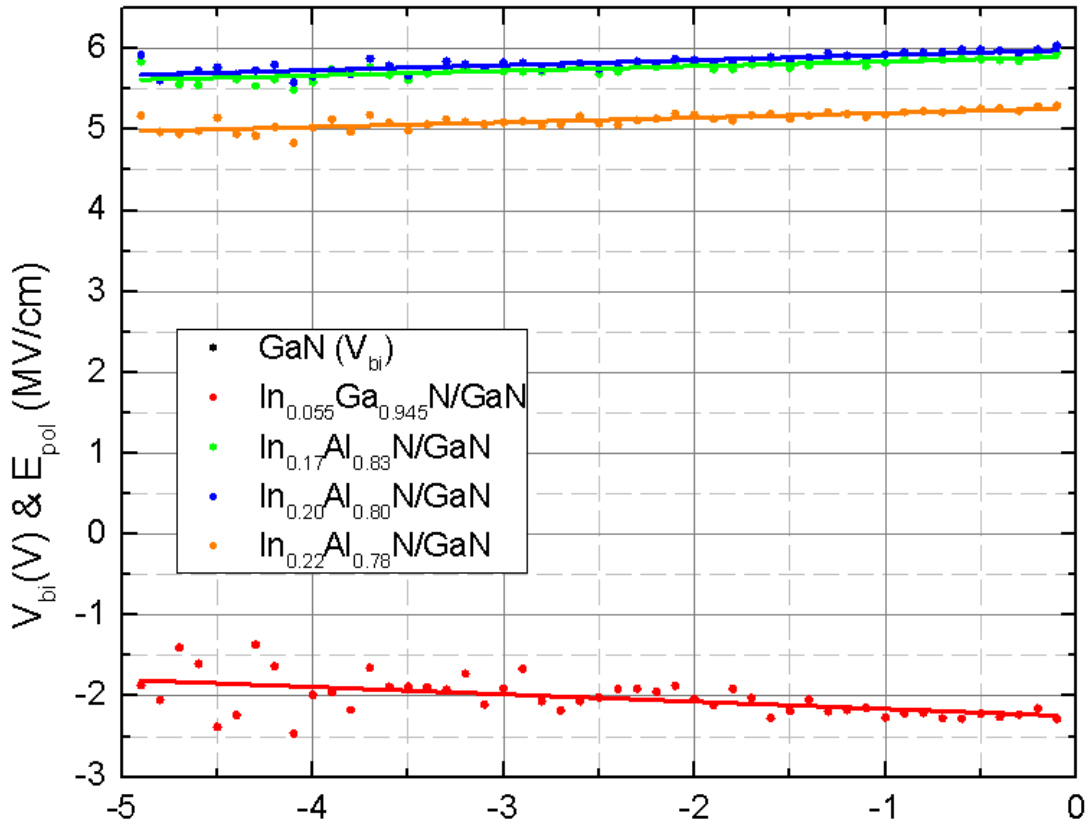


Figure 3.2.6.3.2 Calculation of E_{pol} , using Eq. (3.2.6.3.5) and selection of the value that refers to 0V.

The calculation of polarization fields of the PIN diodes under study resulted in:

- 2.25 ± 1.25 MV/cm for $In_{0.055}Ga_{0.945}N$,
- 5.90 ± 3.10 MV/cm for $In_{0.17}Al_{0.83}N$,
- 5.99 ± 3.14 MV/cm for $In_{0.20}Al_{0.80}N$, and
- 5.26 ± 2.76 MV/cm for $In_{0.21}Al_{0.79}N$.

A very important advantage of the derived equations for E_{pol} over previous equations referred in [24] is that different amounts of the dopant concentrations and the thicknesses can be taken into account, whereas in [24] dopant concentrations and thicknesses have to be the same for all samples. The GaN (no DHS) sample and the DHS samples can thus have almost any (nearly constant) dopant concentration and thickness without inducing any significant error in the calculation. The dependence of V_{bi} on the above terms was investigated using the SiLENSe simulation software. Varying these terms between a nominal and twice this nominal value has proven that the dependence of V_{bi} on the above terms is insignificant, as demonstrated in Fig. 3.2.7.7.1, greatly facilitating the measurement procedure. Previously [24], a large number of diodes had to be investigated, in each sample, attempting to find the same

dopants concentration for all samples. Moreover, if during growth, the GaN (no DHS) sample and DHS samples thicknesses weren't exactly the same, either the samples would have to be re-grown or a large error would be present in the calculation of E_{pol} .

The analytical equation for the CVP signal is:

$$\frac{1}{C^2} = \frac{d_u^2}{\epsilon^2 \cdot A^2} \left[1 + N_i \left(\frac{1}{N_A} - \frac{1}{N_D} - \frac{N_i}{N_A \cdot N_D} \right) \right] + \frac{1}{\epsilon^2 \cdot A^2} \cdot \frac{2 \cdot \epsilon}{q} \cdot \left(\frac{1}{N_A} + \frac{1}{N_D} \right) \cdot \left(V_{bi} - V - \frac{2 \cdot k_B \cdot T}{q} - E_{pol}^{d_{DHS}} \right) \quad (3.2.6.3.6)$$

Considering the effective doping term, $\left(\frac{1}{N_A} + \frac{1}{N_D} \right)$, in Eq. (3.2.6.3.6), if $N_A \gg N_D$ as is the usual case, the slope of the $1/C^2(V)$ curve is proportional to $1/N_D$ and thus N_D can be approximately calculated.

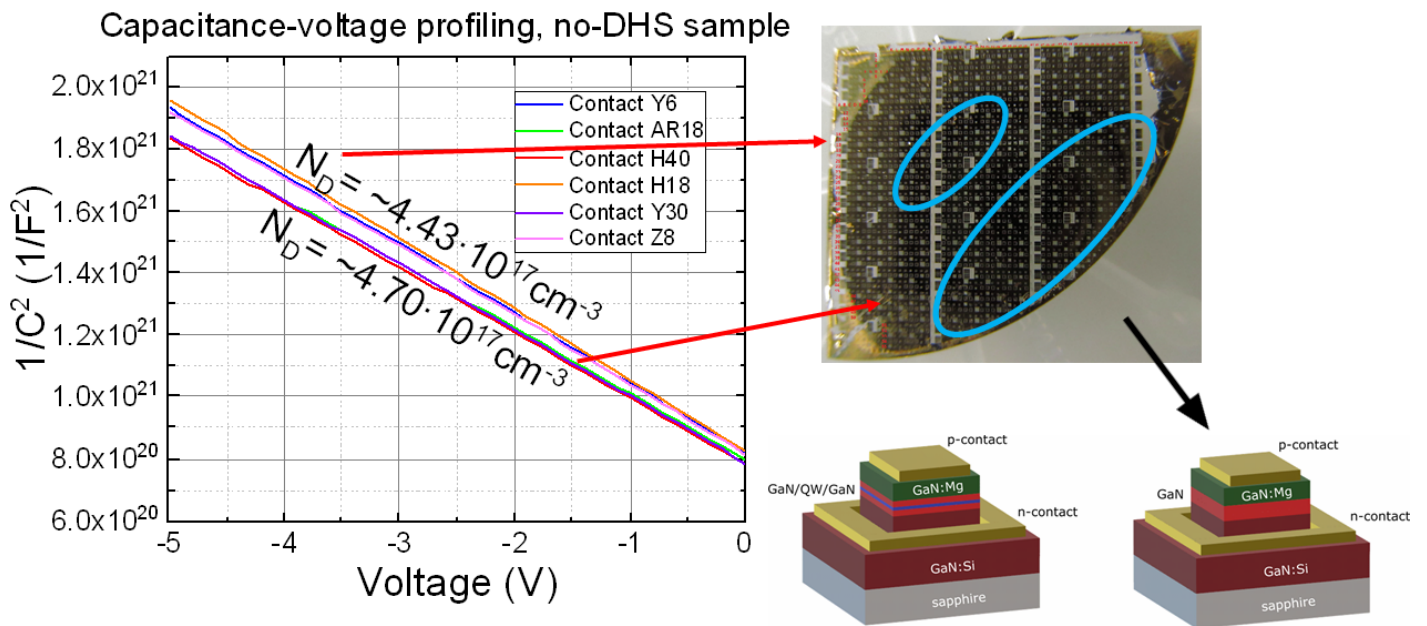


Figure 3.2.6.3.3 By comparison of diodes of the GaN (no DHS) sample, the typical $1/C^2(V)$ curves show a doping variation from $N_D \sim 4.43 \cdot 10^{17} \text{cm}^{-3}$ to $N_D \sim 4.70 \cdot 10^{17} \text{cm}^{-3}$ revealing a radial trend in the increase of dopant concentration.

3.2.6.4

Comparison

For comparison purposes, all theoretically calculated polarization fields E_{pol} are presented in Figs. 3.2.6.4.1-2 in addition to the experimental values. In order to demonstrate the effect of the bowing parameter, a theoretical calculation of E_{pol} using the values and method presented in [97] is also included in Figs. 3.2.6.4.1-2, with $b=0$ (linear interpolation between the binary material systems using Eq. 3.2.6.2.4). It has to be noted, that the bowing parameter b in [97] (Figs. 3.2.6.2.5-6) is completely empirical; this is the reason why in all other approximations (Figs. 3.2.6.2.1-4) $b=0$ was used, since a method for deriving b is not presented in [97]. Nevertheless, it is apparent (Figs. 3.2.6.4.1-2) that using b from [97], the curve is only slightly altered. The Indium content was determined by XRD being $17 \pm 1\%$, $20 \pm 1\%$ and $22 \pm 1\%$ for the $\text{In}_x\text{Al}_{1-x}\text{N}/\text{GaN}$ samples and $5.5 \pm 0.5\%$ for the $\text{In}_x\text{Ga}_{1-x}\text{N}/\text{GaN}$ sample. The experimental values were in agreement with the theoretically predicted values.

$\text{In}_x\text{Ga}_{1-x}\text{N}/\text{GaN}$ Total Internal Polarization fields

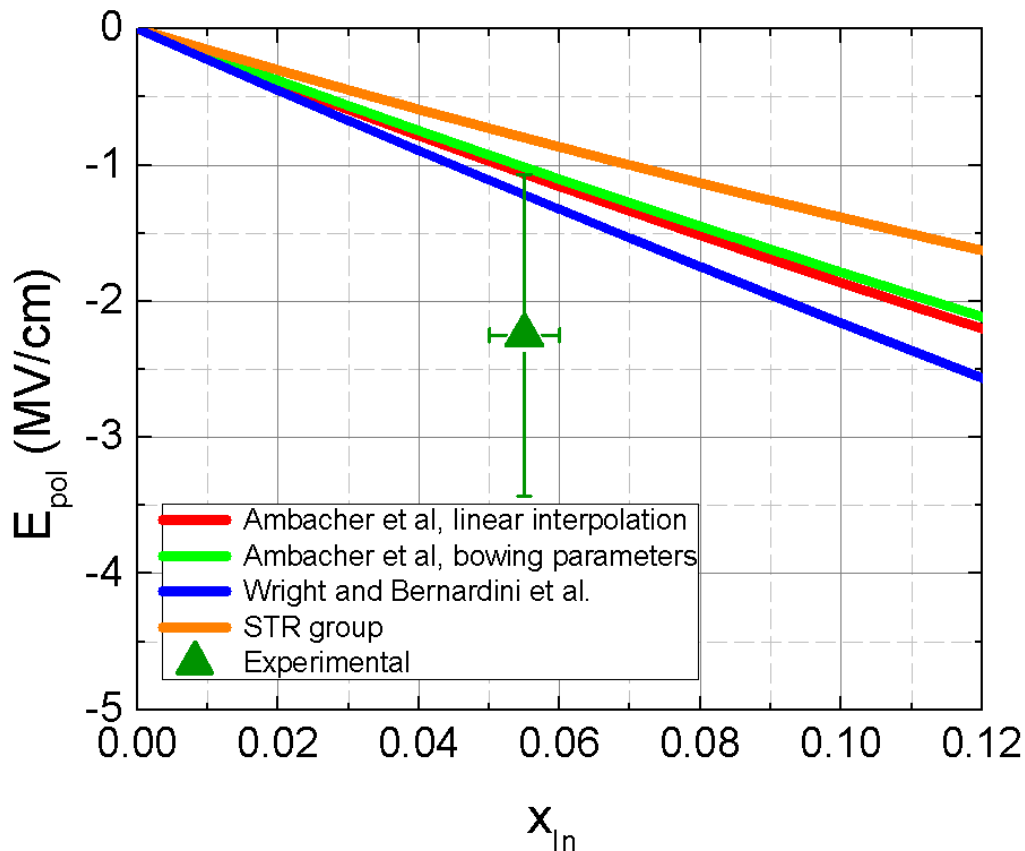


Figure 3.2.6.4.1 Comparison between theoretically predicted and experimental values for the $\text{In}_{0.055}\text{Ga}_{0.945}\text{N}/\text{GaN}$ sample.

In_xAl_{1-x}N/GaN Total Internal Polarization fields

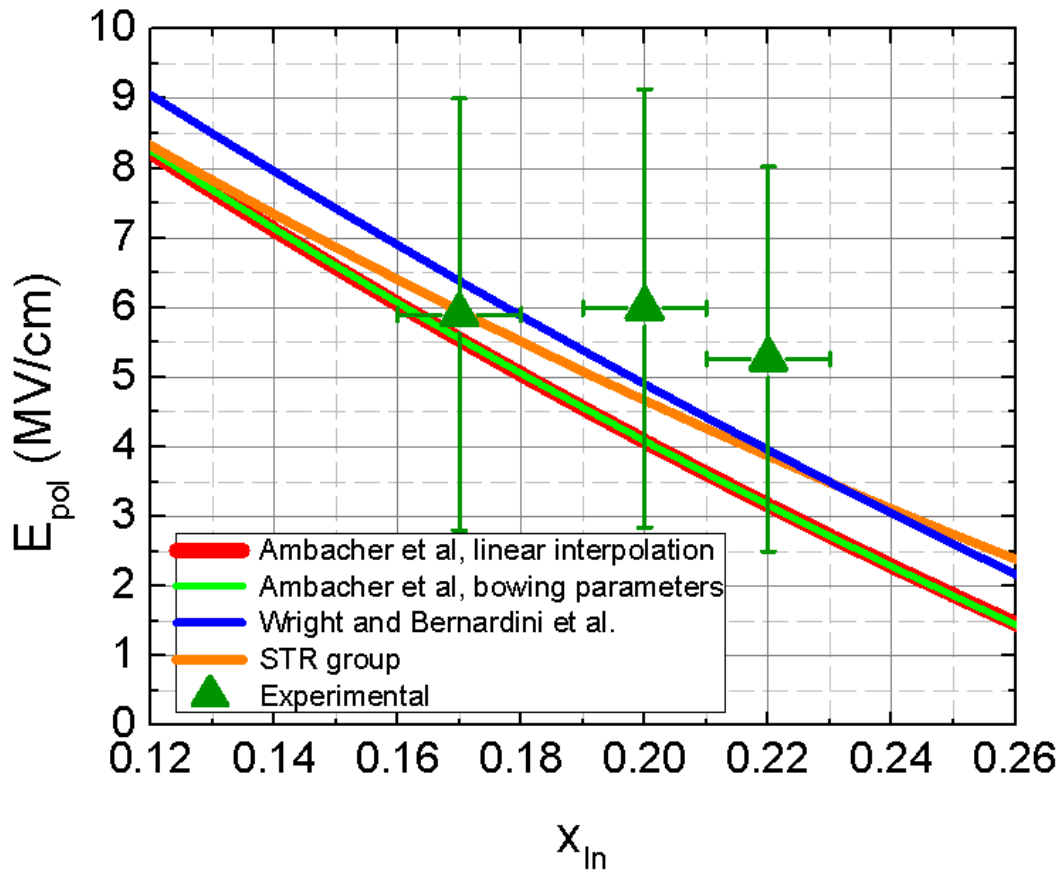


Figure 3.2.6.4.2 Comparison between theoretically predicted and experimental values for the In_xAl_{1-x}N/GaN samples.

3.2.6.5

Overall error evaluation combining methods

The overall relative error of E_{pol} is calculated with respect to multiple parameters. Firstly, it combines the experimental errors of various characterization techniques: XRD, TEM, CVP, and metal contact fabrication. The CVP breaks down ultimately into measurement of voltage, current, and time (when measuring the phase difference of the input voltage to the output current of the sample) and their respective relative errors.

Moreover, the deviation from the non-constant doping profile induces a not assessable error, since it is not possible to derive the E_{pol} and V_{bi} functions in case of an unknown doping profile, as discussed in Chapter 3.2.11.2. In the overall error calculations, this error was set to 0. Apart from this, in PIN diodes, there exists a middle intrinsic layer and the usual approach [24] is to neglect the unintentional doping (N_i) of this layer and set it to 0. Omitting N_i leads to an additional relative error of approximately 5%. In order to eliminate this error source, in this work, analytical functions incorporating the term N_i were derived. Even though only the effective dopant concentration can be determined, as discussed in Chapter 3.2.6.3, including an estimation of N_i and N_A reduces the overall relative error.

Determination of the thickness d_{DHS} induces an additional relative error, since E_{pol} is inversely proportional to the thickness of the double heterostructure (DHS). Provided that the thickness d_{DHS} is determined by TEM measurements for all the samples, the measured thicknesses can be used in the equations without any assumption of the samples having the same thicknesses. Using XRD for the determination of d_{DHS} is not an option, since the thickness ($\sim 4\text{nm}$) of the central layer (InGaN or InAlN) of the double heterostructure d_{DHS} is below the detection limit and this layer is sandwiched between several other nitride layers, as shown in Fig. 2.1.2.1. Still, if XRD is used, the thickness can indirectly be accessed by monitoring the growth rate of a calibration sample consisting of a much thicker layer of the same material as the one under investigation on an appropriate substrate. Similarly, determination of the thicknesses of the intrinsic GaN layers (Fig. 2.1.2.1) also induces an error, even though E_{pol} is not so sensitive to this thickness.

The fact that a direct measurement of the relative permittivity of the samples was not possible and that the literature values [97], [164] vary ($\sim 15\%$) even more than any error this new CVP method incorporates, another very important error connected to this uncertainty arises, as explained in Chapter 3.2.11.

The individual errors of the parameters determining the magnitude of E_{pol} , in Eq. (3.2.6.3.5), which incorporates, in the V_{bi} term, all terms of the GaN (no DHS) reference sample, are given in Table 3.2.6.5.1 denoted as "ref". S denotes the slope of the $1/C^2(V)$. The N_{factor} denotes the following term (Eq.(3.2.6.5.1)), which is also present in Eq. (3.2.6.3.5).

$$N_{\text{factor}} = \left(1 + \frac{N_i}{N_A} - \frac{N_i}{N_D} - \frac{N_i^2}{N_A \cdot N_D} \right) \quad (3.2.6.5.1)$$

The overall relative error of E_{pol} resulting from the propagation of the relative error of each parameter given in Table 3.2.6.5.1 was $\pm 52.5\%$. The effect of the relative error of the E_{pol} parameters, in Eq. (3.2.6.3.5), is depicted in Fig. 3.2.6.5.1.

Table 3.2.6.5.1

Parameter	Relative error (%)	Parameter	Relative error (%)
d_{DHS}	5	ε	5
$d_{\text{GaN}_{\text{DHS}}}$	10	$d_{\text{GaN}_{\text{ref}}}$	10
s_{DHS}	7.5	s_{ref}	7.5
A_{DHS}	0.5	A_{ref}	0.5
$N_{\text{factor}_{\text{DHS}}}$	10	$N_{\text{factor}_{\text{ref}}}$	10
C_{DHS}	5	C_{ref}	5
V_{DHS}	1	V_{ref}	1

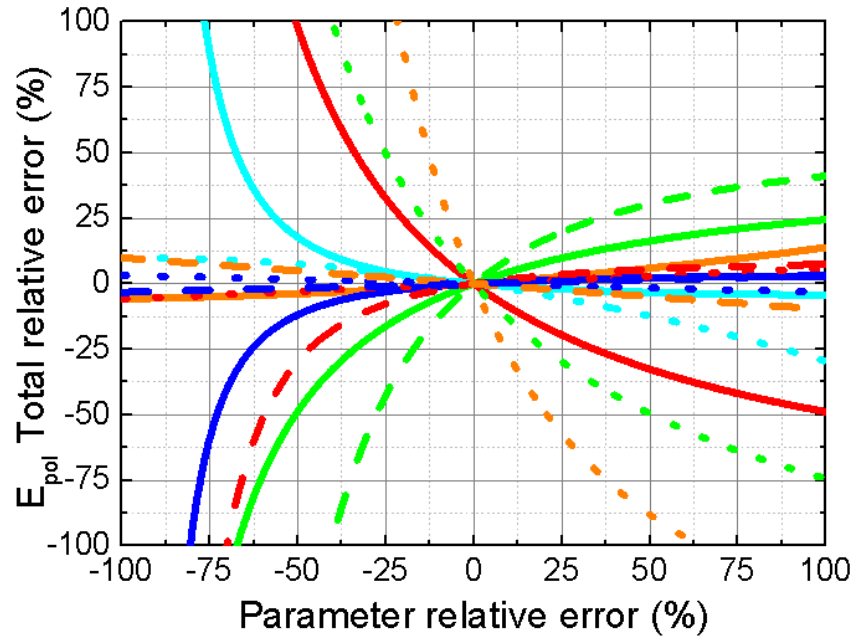
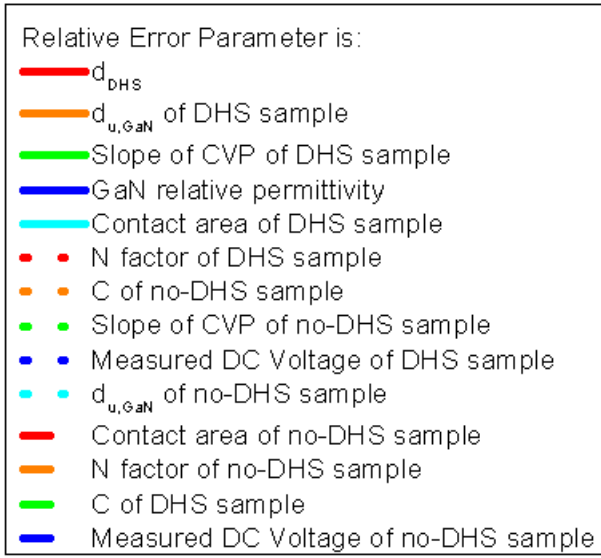


Figure 3.2.6.5.1 Overall relative error of E_{pol} as a function of the relative error of each one of its parameters as shown in Eq. (3.2.6.3.5).

3.2.7

Additional Considerations

3.2.7.1

Light conditions

CVP measurements were performed in a dark environment to avoid a possible influence of light. LEDs are known to also act as light detectors, even though not optimal ones [67]. In the case of measurements under illumination, the device properties may be altered and an additional voltage might be generated, since a light detector, in principle, converts light to an electrical signal.

3.2.7.2

Voltage regulation

For the LCR instrument, voltage regulation is not possible for every current. This translates to random voltage points, if the current is more than 50nA. In this work, when comparing samples of the same series, the currents were in the same instrument current scale and thus the voltage was systematically almost the same.

3.2.7.3

Limitations

Limitations such as minimum and maximum instrument supported currents and voltages existed. Additionally, in several cases, even though the instruments supported a voltage or current range, considerations to avoid damage of the sample used lead to minimum and maximum limits.

3.2.7.3.1

Voltage

The lower limit of the voltage source (μV) was sufficiently accurate. The upper limit though, being an absolute of 40V, was insufficient in a few cases where an investigation in far reverse voltages was desired.

3.2.7.3.2

Current

The current of the instrument power source was insufficient in most of the forward bias investigations. Though an absolute maximum of 100mA was ascertained by the manufacturer, in the praxis, 20mA was the limit, with the instrument indicating an overload for currents greater than that. Furthermore, the noise for the measurement range of 1pA-10nA was too high, so that CVP measurements below 200Hz could not be performed, since the impedance was too high and the induced currents too low (1pA-10nA). It has to be noted that in CVP, even though the DC bias can be sufficiently high, the AC voltage has to be kept low in order to use the “small signal approximation”. At every bias though, the AC component oscillating around the DC bias value slightly changes the capacitance. This leads to controversies in the evaluation of the capacitance, if such a deviation from the DC bias is high, since a root mean square (rms) averaging would have to be performed as the instrument measures the AC components. A better method, even though very complicated, could possibly be devised if the instrument supported capturing the continuous time voltage and current signals, quite like a recording oscilloscope does.

3.2.7.4

Selecting the f- and V-range

Due to the limitations, as explained in Chapter 3.2.7.3, and also due to extreme band bending voltages, the voltage range had to be restricted to bias voltages of 0V-(-5V). Literature explaining in detail and quantifying, what is “too much voltage” with regard to band bending, to the extent of the writer's knowledge, is absent. In that context, 5V reverse bias was assumed to avoid large band bending, even though it could potentially be a reason for the trend observed and commented in Chapter 3.2.6.3. The frequency range of the instrument was 20Hz-2MHz. Due to limitations, as explained in Chapter 3.2.7.3.2, a minimum of 200Hz was used. Also above 1.7MHz, a

frequency dependence of the measurement result was almost always observed. This is probably plasmatic and due to instrument limitations of the time measurement accuracy, when evaluating a certain phase, as a frequency dependence was also found to be present even in single resistor components. An optimum of 200kHz-280kHz was used in order to be in the as best as possible current measurement scale of the instrument also avoiding the frequency dependence present at MHz frequencies.

3.2.7.5

Samples degradation & breakdown

Samples degradation, even failure, was often observed when attempting to measure in forward bias thus limiting measurements to the use of reverse bias. A diode breakdown was never observed for the samples studied, although it is a definite possibility in diodes. An additional possibility is that an electric arc is created between the metal contacts, since their distance is less than 10 μ m. This would possibly mean that the sample is more or less unaffected, but the instrument could possibly be damaged, due to a very rapidly increasing current.

3.2.7.6

Parasitic Diffusion capacitance in forward bias

In forward bias [67], [68], there exists a diffusion capacitance, orders of magnitude greater than the depletion region capacitance the CVP measurement targets to. This renders the actual CVP measurement useless in forward bias. For application purposes and optimum efficiency utilizing certain biases, AC magnitudes, and optimum frequencies making use of such an effect could be a possibility.

3.2.7.7

V_{bi} dependence on N , ϵ_r , N_i , d_u & d_{DHS} (SiLENCE simulation)

Under the assumption that all the PIN diodes have the same V_{bi} , Eq (3.2.6.3.2), an analytical Eq. (3.2.6.3.5) for E_{pol} can be derived, as presented in Chapter 3.2.6.3. This assumption translates in assuming same thicknesses and doping profiles only for the calculation of V_{bi} , since E_{pol} is calculated using another equation.

The GaN sample structure was simulated using SiLENSe simulation software. This sample is the one without a heterostructure (no DHS). Changing the undoped

thickness region had almost no effect in the built-in potential. The depletion region width varied from 100nm to 110nm at 0V approximately. Doubling the dopant concentration in every layer except from the unintentionally doped one, in the intrinsic region, slightly changed the built-in potential for both nominal and doubled thickness of the intrinsic region. The depletion region width for the doubled dopant concentration was 80nm for the normal intrinsic region thickness and 90nm for the doubled.

The V_{bi} variation between the nominal and twice the nominal values was always less than 0.8%, thus proving that the new analytical equation for experimentally calculating E_{pol} by using CVP is valid, even if by comparing samples the permittivity (ϵ), all dopant concentrations and all thicknesses vary as much as 200%.

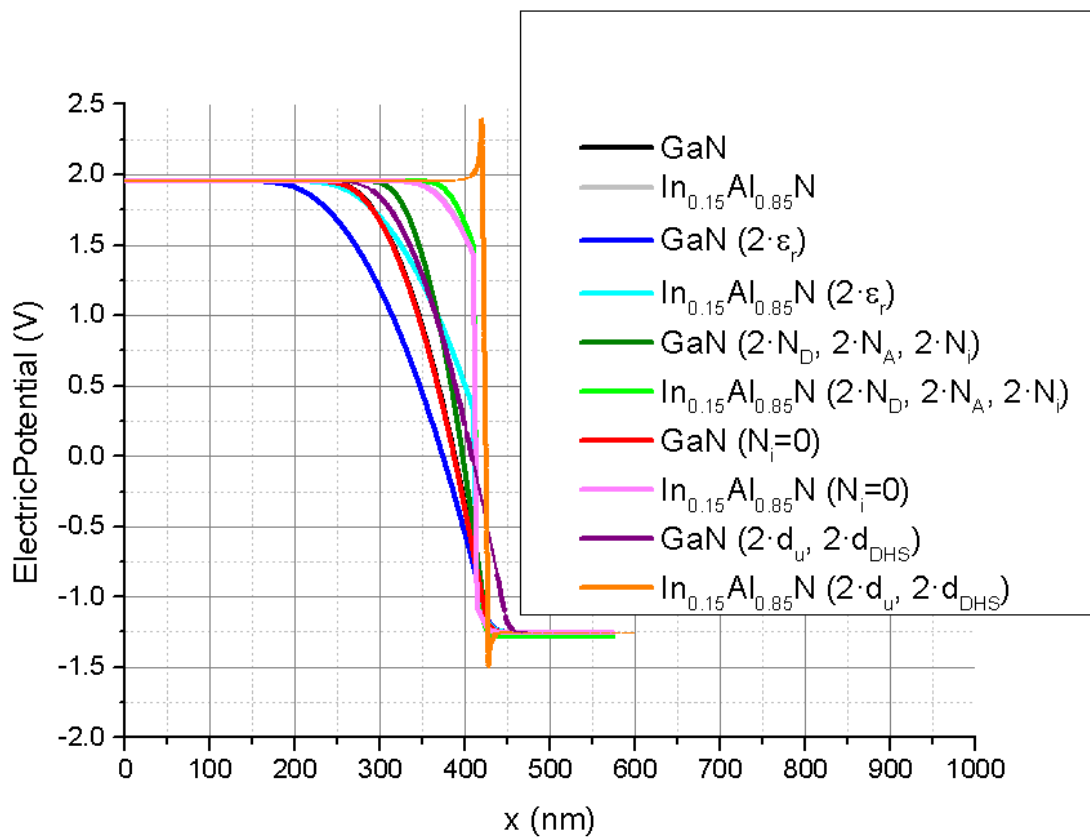


Figure 3.2.7.7.1 V_{bi} variation by varying the V_{bi} parameters between nominal and twice the nominal values (the V_{bi} variation was always less than 0.8% even if, ϵ , all dopants concentrations and all thicknesses vary as much as 200% between samples).

3.2.8

Schottky model

Only in a Schottky diode, the depletion region width calculated using CVP can be converted into a device x-axis. In any other kind of diode, the doping ratio of the p- and n-regions, and also the depletion region width have to be taken into account; because the measured effective dopant concentration is actually the weighted average of the p- and n-regions, only the effective dopant concentration as a function of the depletion region width can be calculated, as shown in Fig. 3.2.11.3.1. This can be also observed on Eq. (3.2.2.2.1), where the capacitance is a function of the depletion region width w (and not the x-axis).

3.2.9

Schottky with intrinsic region model

The case of an n-Schottky diode incorporating an intrinsic region between the doped region and the Schottky metal contact is identical to the normal Schottky diode model by changing only the doping profile accordingly.

3.2.10

p-n junction model

In the p-n junction model, assuming constant doping regions and thus using the abrupt junction approximation [68], the equation for calculating V_{bi} is:

$$W_{Dp} + W_{Dn} = \sqrt{\frac{2\epsilon_s}{q} \left(\frac{N_A + N_D}{N_A N_D} \right) \psi_{bi}}. \quad (3.2.10.1)$$

3.2.11

PIN diode model

3.2.11.1

Constant Doping profile

The approximation most often used is the constant doping. Deviation of maximum 30% from the intended doping during growth and also 15% variation of doping across the depletion region was observed within the samples (Fig. 3.2.11.3.1). V_{bi} can be either calculated using Eq. (3.2.6.3.2) or approximated using the V-axis intercept of the CVP signal [68]. Both approaches are not ideal because the former includes values often not available, such as the exact relative permittivities and thicknesses, and the latter assumes a constant doping profile, which is of course deviating from the truth.

3.2.11.2

General case doping profile

For the case of any doping profile, the general definition of the device potential as a function of length w across the layers is given by Eq. (3.2.6.3.3); using this equation, it is apparent that a non-constant doping profile, as shown in Fig. 3.2.11.3.1, ultimately results in a non-linear CVP signal ($1/C^2(V)$). Note that this equation is only valid within the depletion region width and only if there is no external applied voltage (0V). For a known doping profile, even if the integral cannot be theoretically derived, we can use the discrete x-axis approximation and thus calculate any of the above properties utilizing discrete plane integrals. In the case of an unknown doping profile, Eq. (3.2.6.3.3) cannot be used to derive the equations for calculating E_{pol} . Moreover, as discussed in Chapter 3.2.7.6, in forward bias, it is impossible to use CVP, in general, thus it is also not possible to determine experimentally the effective doping

profile $\left(\frac{1}{N_A} + \frac{1}{N_D} \right)$ for depletion region widths smaller than that present at 0V. The

reason for this is that the depletion region width is reduced with the increase of the voltage as shown in Eq. (3.2.6.3.1).

3.2.11.3

N(w)

The effective dopant concentration (N) and the depletion region width (w) are associated to one another through their dependence on voltage. The dependence of the effective dopant concentration on the depletion region width N(w) is illustrated in Fig. 3.2.11.3.1. The depletion region width (w) is inversely proportional to the capacitance (C), Eq. (3.2.2.2.1) and effective dopant concentration (N) is inversely proportional to the slope of $1/C^2$, Eq. (3.2.6.3.6).

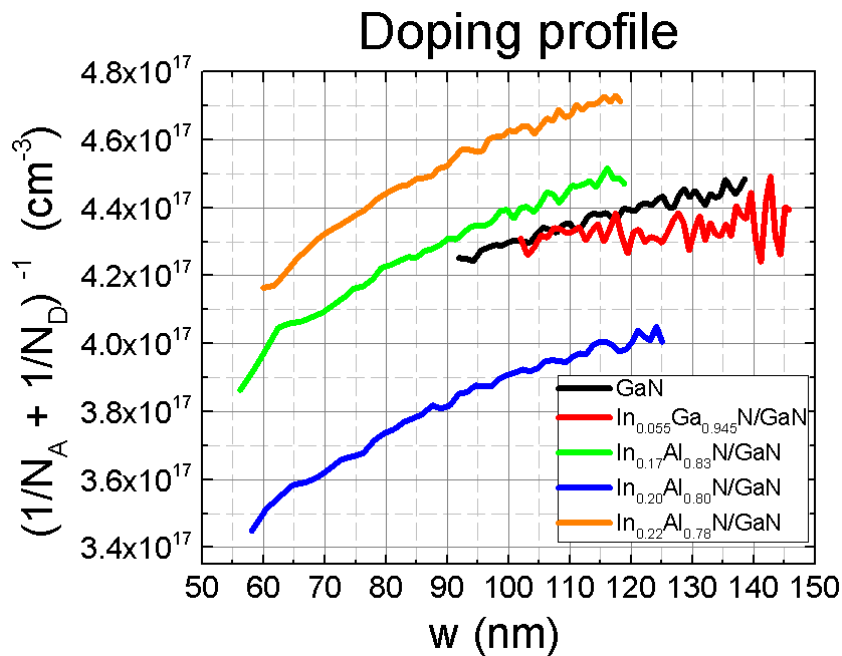


Figure 3.2.11.3.1 PIN diodes doping variation of 15% across the depletion region.

4

Conclusions

4.1

Summary

Several tasks were successfully completed in this work:

- New model for accurate capacitance evaluation: Over 3x less relative error
- New analytical equations for the calculation of polarization field E_{pol} using CVP measurements, valid even if the relative permittivity, dopant concentration, and thicknesses of the samples studied vary by more than 200% from one sample to the other
- Incorporation of the unintentional doping (N_i) and temperature terms in the E_{pol} equation of the constant doping approximation
- Determination of the overall relative error of the polarization field E_{pol} of approximately $\pm 52.5\%$
- Modulated Electroreflectance measurements demonstrating the three valence split bands E_a , E_b , E_c of the PIN diodes based on GaN and InGaN/GaN quantum well heterostructures
- Determination of the fundamental gap energy of the InGaN/GaN QW heterostructure $E_a=E_0= 3.27$ eV from the observed Franz-Keldysh Oscillations (FKOs)
- Calculation of the InGaN layer thickness with respect to the QW width $d= 3.96$ nm, which is in excellent agreement with the XRD results
- Evaluation of the electro-optically modulated field $F = 0.04$ MV/cm from FKOs related to the barrier regions of the InGaN/GaN heterojunction
- Electroluminescence measurements indicating spectral voltage dependence: Higher voltages favor the UV over the VIS defect-related emission
- Experimental quantification of the polarization fields:
-2.25 \pm 1.25 MV/cm for $In_{0.055}Ga_{0.945}N$,
5.90 \pm 3.10 MV/cm for $In_{0.17}Al_{0.83}N$,
5.99 \pm 3.14 MV/cm for $In_{0.20}Al_{0.80}N$, and
5.26 \pm 2.76 MV/cm for $In_{0.21}Al_{0.79}N$.

4.2

Future Perspectives

4.2.1

Equivalent circuit analysis as a means to higher efficiencies

All the electrical and optical emission characteristics could possibly be combined with a thorough investigation of the ideal electrical input characteristics in order to maximize the overall LED efficiency (voltage shape, fundamental frequency, DC and AC components etc).

4.2.2

Future Schottky samples structure design considerations

For a more detailed study of the Polarization fields, it would be greatly beneficial to have a Schottky diode [67], [75] structure. Only then the depletion region width would be equal to the x-axis and thus accurately depict every property with respect to the x-axis, as explained in Chapters 3.2.8-9.

4.2.3

Future samples, with $E_g(\text{DHS}) < E_g(\text{buffer})$

Detailed evaluation of the optical properties (band gaps, three split valence bands, emission properties, etc.) of the InGaN/GaN and InAlN/GaN QW heterostructures in dependence of their Indium (In) content can be accessed using ER and EL spectroscopy, as presented in this work in structures where $E_g(\text{DHS}) < E_g(\text{buffer})$.

5

References

- [1] Zoroddu, Agostino, et al. "First-principles prediction of structure, energetics, formation enthalpy, elastic constants, polarization, and piezoelectric constants of AlN, GaN, and InN: Comparison of local and gradient-corrected density-functional theory." *Physical Review B* 64.4 (2001): 045208.
- [2] Bernardini, Fabio, Vincenzo Fiorentini, and David Vanderbilt. "Spontaneous polarization and piezoelectric constants of III-V nitrides." *Physical Review B* 56.16 (1997): R10024.
- [3] Yu, E. T., et al. "Spontaneous and piezoelectric polarization effects in III-V nitride heterostructures." *Journal of Vacuum Science & Technology B: Microelectronics and Nanometer Structures Processing, Measurement, and Phenomena* 17.4 (1999): 1742-1749.
- [4] Bernardini, Fabio, and Vincenzo Fiorentini. "First-principles calculation of the piezoelectric tensor d_{ij} of III-V nitrides." *Applied physics letters* 80.22 (2002): 4145-4147.
- [5] Brown, Iain Henry, et al. "Determination of the piezoelectric field in InGaN quantum wells." *Applied Physics Letters* 86.13 (2005): 131108.
- [6] Dal Corso, Andrea, et al. "Ab initio study of piezoelectricity and spontaneous polarization in ZnO." *Physical Review B* 50.15 (1994): 10715.
- [7] Topolov, Vitaly Yuryevich, and Christopher Rhys Bowen. *Electromechanical properties in composites based on ferroelectrics*. Springer Science & Business Media, 2008.
- [8] Wetzel, Christian, et al. "Piezoelectric Stark-like ladder in GaN/GaInN/GaN heterostructures." *Japanese journal of applied physics* 38.2B (1999): L163.
- [9] Takeuchi, Tetsuya, et al. "Quantum-confined Stark effect due to piezoelectric fields in GaInN strained quantum wells." *Japanese Journal of Applied Physics* 36.4A (1997): L382.
- [10] Li, J. M., et al. "Effect of spontaneous and piezoelectric polarization on intersubband transition in $\text{Al}_x\text{Ga}_{1-x}\text{N}$ -GaN quantum well." *Journal of Vacuum Science & Technology B: Microelectronics and Nanometer Structures Processing, Measurement, and Phenomena* 22.6 (2004): 2568-2573.
- [11] Dong, L., et al. "Band gap tuning in GaN through equibiaxial in-plane strains." *Applied Physics Letters* 96.20 (2010): 202106.
- [12] Lorenz, K., et al. "Relaxation of compressively strained AlInN on GaN." *Journal of Crystal Growth* 310.18 (2008): 4058-4064.
- [13] Guillot, C., et al. "Capacitance-voltage profiling and thermal evolution of the conduction band-offset of unstrained Ga_{0.47}In_{0.53}As/InP single quantum well." *Journal of electronic materials* 28.8 (1999): 975-979.
- [14] Yan, Qimin, et al. "Effects of strain on the band structure of group-III nitrides." *Physical Review B* 90.12 (2014): 125118.

- [15] Jian-Zhi, Zhao, et al. "Determination of the relative permittivity of the AlGa_N barrier layer in strained AlGa_N/Ga_N heterostructures." *Chinese Physics B* 18.9 (2009): 3980.
- [16] Tawfik, Wael Z., Han-Youl Ryu, and June Key Lee. "Electroreflectance spectroscopy of compressively strained InGa_N/Ga_N multi-quantum well structures." *Current Applied Physics* 14.11 (2014): 1504-1508.
- [17] Kisielowski, Ch, et al. "Strain-related phenomena in Ga_N thin films." *Physical Review B* 54.24 (1996): 17745.
- [18] Ghosh, Sandip, et al. "Polarized photoreflectance spectroscopy of strained A-plane Ga_N films on R-plane sapphire." (2005): 026105.
- [19] Lorenz, K., et al. "Anomalous ion channeling in AlIn_N/Ga_N bilayers: determination of the strain state." *Physical review letters* 97.8 (2006): 085501.
- [20] Kneissl, Michael, and Jens Rass. "III-Nitride Ultraviolet Emitters." Springer Series in Materials Science. Springer International Publishing Cham, 2016.
- [21] Schubert, E. FRED, and Light-Emitting Diodes. "Cambridge, UK." (2006).
- [22] Feneberg, Martin, and Klaus Thonke. "Polarization fields of III-nitrides grown in different crystal orientations." *Journal of Physics: Condensed Matter* 19.40 (2007): 403201.
- [23] Gessmann, Th, et al. "Ohmic contact technology in III nitrides using polarization effects of cap layers." *Journal of applied physics* 92.7 (2002): 3740-3744.
- [24] Rychetsky, Monir, et al. "Determination of polarization fields in group III-nitride heterostructures by capacitance-voltage-measurements." *Journal of Applied Physics* 119.9 (2016): 095713.
- [25] Hanada, T. "Basic properties of ZnO, Ga_N, and related materials." *Oxide and nitride semiconductors* (2009): 1-19.
- [26] Wu, Junqiao. "When group-III nitrides go infrared: New properties and perspectives." *Journal of Applied Physics* 106.1 (2009): 5.
- [27] Schwarz, Ulrich T., and Michael Kneissl. "Nitride emitters go nonpolar." *physica status solidi (RRL)-Rapid Research Letters* 1.3 (2007).
- [28] Morkoç, Hadis. *Handbook of nitride semiconductors and devices, Materials Properties, Physics and Growth*. Vol. 1. John Wiley & Sons, 2009.
- [29] Dreyer, Cyrus E., et al. "Correct implementation of polarization constants in wurtzite materials and impact on III-nitrides." *Physical Review X* 6.2 (2016): 021038.
- [30] Hurni, Christophe A., et al. "Capacitance-voltage profiling on polar III-nitride heterostructures." *Journal of Applied Physics* 112.8 (2012): 083704.
- [31] Fiorentini, Vincenzo, Fabio Bernardini, and Oliver Ambacher. "Evidence for nonlinear macroscopic polarization in III-V nitride alloy heterostructures." *Applied Physics Letters* 80.7 (2002): 1204-1206.
- [32] Bernardini, Fabio, and Vincenzo Fiorentini. "Nonlinear macroscopic polarization in III-V nitride alloys." *Physical Review B* 64.8 (2001): 085207.
- [33] Bernardini, Fabio, and Vincenzo Fiorentini. "Erratum: Nonlinear macroscopic polarization in III-V nitride alloys [Phys. Rev. B 64, 085207 (2001)]." *Physical Review B* 65.12 (2002): 129903.
- [34] Hurni, Christophe A., et al. "Capacitance-voltage profiling on polar III-nitride heterostructures." *Journal of Applied Physics* 112.8 (2012): 083704.

- [35] Al-Kuhaili, M. F., et al. "Electroreflectance of hexagonal gallium nitride at the fundamental and E 1 spectral regions." *Applied physics letters* 82.8 (2003): 1203-1205.
- [36] Drabinska, Aneta, et al. "Electroreflectance and photorefectance spectra of tricolor III-nitride detector structures." *physica status solidi (a)* 204.2 (2007): 459-465.
- [37] Huang, Jian-Jang, Hao-Chung Kuo, and Shyh-Chiang Shen. *Nitride Semiconductor Light-Emitting Diodes (LEDs): Materials, Technologies and Applications*. Woodhead Publishing, 2014.
- [38] Manasreh, Mahmoud Omar, ed. *III-nitride semiconductors: electrical, structural and defects properties*. Elsevier, 2000.
- [39] Ruterana, Pierre, Martin Albrecht, and Jörg Neugebauer, eds. *Nitride semiconductors: handbook on materials and devices*. John Wiley & Sons, 2006.
- [40] Madelung, O., U. Rössler, and M. Schulz. "Impurities and defects in group IV elements, IV–IV and III–V compounds. Part a: group IV elements." Landolt-Börnstein (Ed.), *Numerical Data and Functional Relationships in Science and Technology–New Series, Group III Condensed Matter* 41 (2002): 877.
- [41] Madelung, O., U. Rössler, and M. Schulz. "Impurities and defects in group IV elements, IV–IV and III–V compounds. Part b: group IV elements." Landolt-Börnstein (Ed.), *Numerical Data and Functional Relationships in Science and Technology–New Series, Group III Condensed Matter* 41 (2002): 877.
- [42] Madelung, O., U. Rössler, and M. Schulz. "Impurities and Defects in Group IV Elements, IV-IV and III-V Compounds. Part b: Group IV-IV and III-V Compounds." (2003).
- [43] König, E., and G. König. "73A1-73V6." *Magnetic Susceptibilities*. Springer Berlin Heidelberg, 1984. 661-668.
- [44] Xu, Dongwei, et al. "Stacking and electric field effects in atomically thin layers of GaN." *Journal of Physics: Condensed Matter* 25.34 (2013): 345302.
- [45] Moram, M. A., and M. E. Vickers. "X-ray diffraction of III-nitrides." *Reports on progress in physics* 72.3 (2009): 036502.
- [46] Kim, Min-Ho, et al. "Origin of efficiency droop in GaN-based light-emitting diodes." *Applied Physics Letters* 91.18 (2007): 183507.
- [47] Hao, M., et al. "Photoluminescence studies on InGaN/GaN multiple quantum wells with different degree of localization." *Applied physics letters* 81.27 (2002): 5129-5131.
- [48] Jeon, E. S., et al. "Recombination dynamics in InGaN quantum wells." *Applied physics letters* 69.27 (1996): 4194-4196.
- [49] DenBaars, Steven P., et al. "Development of gallium-nitride-based light-emitting diodes (LEDs) and laser diodes for energy-efficient lighting and displays." *Acta Materialia* 61.3 (2013): 945-951.
- [50] Goldhahn, R., et al. "Refractive index and gap energy of cubic In_xGa_{1-x}N." *Applied Physics Letters* 76.3 (2000): 291-293.
- [51] Leung, Mandy MY, Aleksandra B. Djurišić, and E. Herbert Li. "Refractive index of InGaN/GaN quantum well." *Journal of applied physics* 84.11 (1998): 6312-6317.
- [52] Laws, G. M., et al. "Improved refractive index formulas for the Al_xGa_{1-x}N and In_yGa_{1-y}N alloys." *Journal of applied Physics* 89.2 (2001): 1108-1115.

- [53] Sanford, Norman A., et al. "Refractive index and birefringence of $\text{In}_x\text{Ga}_{1-x}\text{N}$ films grown by MOCVD." *physica status solidi (c)* 2.7 (2005): 2783-2786.
- [54] Wilkins, N. J. M. "Infra-red interference measurements on oxide films on zirconium." *Corrosion Science* 4.1-4 (1964): 17-24.
- [55] Teolis, B. D., et al. "Infrared reflectance spectroscopy on thin films: Interference effects." *Icarus* 190.1 (2007): 274-279.
- [56] Hunger, Ralf, et al. "In situ deposition rate monitoring during the three-stage-growth process of Cu (In, Ga) Se 2 absorber films." *Thin Solid Films* 431 (2003): 16-21.
- [57] Erman, M., et al. "Electronic states and thicknesses of GaAs/GaAlAs quantum wells as measured by electroreflectance and spectroscopic ellipsometry." *Journal of applied physics* 56.11 (1984): 3241-3249.
- [58] Thorn, A. P., et al. "The electro-reflectance lineshape for a quantum well: the dependence on angle of incidence and temperature." *Journal of Physics C: Solid State Physics* 20.26 (1987): 4229.
- [59] Kallergi, N., et al. "Correlation of interference effects in photoreflectance spectra with GaAs homolayer thickness." *Journal of applied physics* 68.9 (1990): 4656-4661.
- [60] Klipstein, P. C., et al. "Electroreflectance spectroscopy from quantum well structures in an electric field." *Journal of Physics C: Solid State Physics* 19.6 (1986): 857.
- [61] Klipstein, P. C., and N. Apsley. "A theory for the electroreflectance spectra of quantum well structures." *Journal of Physics C: Solid State Physics* 19.32 (1986): 6461.
- [62] Shan, W., et al. "Temperature dependence of interband transitions in GaN grown by metalorganic chemical vapor deposition." *Applied physics letters* 66.8 (1995): 985-987.
- [63] Li, C. F., et al. "Temperature dependence of the energies and broadening parameters of the interband excitonic transitions in wurtzite GaN." *Physical Review B* 55.15 (1997): 9251.
- [64] Schenk, H. P. D., M. Leroux, and P. De Mierry. "Luminescence and absorption in InGaN epitaxial layers and the van Roosbroeck–Shockley relation." *Journal of Applied Physics* 88.3 (2000): 1525-1534.
- [65] Ambacher, Oliver, et al. "Absorption of InGaN single quantum wells determined by photothermal deflection spectroscopy." *Japanese journal of applied physics* 37.3R (1998): 745.
- [66] Kvietkova, J., et al. "Optical investigations and absorption coefficient determination of InGaN/GaN quantum wells." *physica status solidi (a)* 190.1 (2002): 135-140.
- [67] Kasap, Safa O. *Principles of electronic materials and devices*. Vol. 2. New York: McGraw-Hill, 2006.
- [68] Sze, Simon M., and Kwok K. Ng. *Physics of semiconductor devices*. John Wiley & sons, 2006.
- [69] Zheng, Xue Feng, et al. "Energy and Spatial Distributions of Electron Traps Throughout $\text{SiO}_2/\text{Al}_2\text{O}_3$ Stacks as the IPD in Flash Memory Application." *IEEE Transactions on Electron Devices* 57.1 (2010): 288-296.

- [70] Cohen, S. S., and G. S. Gildenblat. "Metal-semiconductor contacts and devices. VLSI electronics microstructure science, vol. 13." (1986).
- [71] Yakovlev, G., D. Frolov, and V. Zubkov. "Investigation of delta-doped pHEMT InGaAs/GaAs/AlGaAs structures by the electrochemical capacitance-voltage technique." *Journal of Physics: Conference Series*. Vol. 690. No. 1. IOP Publishing, 2016.
- [72] Qu, Shenqi, et al. "Analysis of transconductance characteristic of AlGaIn/GaN HEMTs with graded AlGaIn layer." *The European Physical Journal-Applied Physics* 66.2 (2014).
- [73] Mönch, Winfried. "Adsorbate-induced surface states and Fermi-level pinning at semiconductor surfaces." *Journal of Vacuum Science & Technology B: Microelectronics Processing and Phenomena* 7.5 (1989): 1216-1225.
- [74] Grundmann, Marius. *Physics of Semiconductors*. Vol. 11. Berlin: Springer, 2010.
- [75] Kahng, D., and S. H. Wemple. "Measurement of nonlinear polarization of KTaO₃ using Schottky diodes." *Journal of Applied Physics* 36.9 (1965): 2925-2929.
- [76] Ye, P. D., et al. "GaN metal-oxide-semiconductor high-electron-mobility-transistor with atomic layer deposited Al₂O₃ as gate dielectric." *Applied Physics Letters* 86.6 (2005): 063501.
- [77] Kaplar, R. J., S. R. Kurtz, and D. D. Koleske. "Novel optical probes of InGaIn/GaN light-emitting diodes: 1. Electroreflectance Stark spectroscopy, and 2. Time-resolved emission." *physica status solidi (c)* 2.7 (2005): 2866-2870.
- [78] Wu, Yuh-Renn, et al. "Electronic and optical properties of InGaIn quantum dot based light emitters for solid state lighting." *Journal of applied physics* 105.1 (2009): 013117.
- [79] Hatakeyama, Yoshitomo, et al. "High-Breakdown-Voltage and Low-Specific-on-Resistance GaN p-n junction diodes on free-standing GaN substrates fabricated through low-damage field-plate process." *Japanese Journal of Applied Physics* 52.2R (2013): 028007.
- [80] Krishnamoorthy, Sriram, et al. "Low resistance GaN/InGaIn/GaN tunnel junctions." *Applied Physics Letters* 102.11 (2013): 113503.
- [81] Nakamura, Shuji, Masayuki Senoh, and Takashi Mukai. "High-power InGaIn/GaN double-heterostructure violet light emitting diodes." *Applied Physics Letters* 62.19 (1993): 2390-2392.
- [82] Cao, X. A., et al. "Temperature-dependent emission intensity and energy shift in InGaIn/GaN multiple-quantum-well light-emitting diodes." *Applied Physics Letters* 82.21 (2003): 3614-3616.
- [83] Kuball, M., et al. "Gain spectroscopy on InGaIn/GaN quantum well diodes." *Applied physics letters* 70.19 (1997): 2580-2582.
- [84] Masui, Hisashi, et al. "Optical polarization characteristics of m-oriented InGaIn/GaN light-emitting diodes with various indium compositions in single-quantum-well structure." *Journal of Physics D: Applied Physics* 41.22 (2008): 225104.
- [85] Willner, Alan E., et al. "Optics and photonics: Key enabling technologies." *Proceedings of the IEEE 100.Special Centennial Issue* (2012): 1604-1643.

- [86] Shur, Michael S., and Jian-Qiang Lu. "Terahertz sources and detectors using two-dimensional electronic fluid in high electron-mobility transistors." *IEEE Transactions on microwave theory and techniques* 48.4 (2000): 750-756.
- [87] Bai, J., T. Wang, and S. Sakai. "Influence of the quantum-well thickness on the radiative recombination of InGa_N/Ga_N quantum well structures." *Journal of Applied physics* 88.8 (2000): 4729-4733.
- [88] Park, Seoung-Hwan, et al. "Light emission enhancement in blue InGaAlN/InGa_N quantum well structures." *Applied Physics Letters* 99.18 (2011): 181101.
- [89] Ibbetson, J. P., et al. "Polarization effects, surface states, and the source of electrons in AlGa_N/Ga_N heterostructure field effect transistors." *Applied Physics Letters* 77.2 (2000): 250-252.
- [90] Wang, Dong-Po, Chi-Chang Wu, and Chia-Chun Wu. "Determination of polarization charge density on interface of Al Ga_N/Ga_N heterostructure by electroreflectance." *Applied physics letters* 89.16 (2006): 161903.
- [91] Zhou, Yu-gang, et al. "Investigation of the Polarization-Induced Charges in Modulation-Doped Al_xGa_{1-x}N/Ga_N Heterostructures through Capacitance–Voltage Profiling and Simulation." *Japanese journal of applied physics* 41.4S (2002): 2531.
- [92] Yu-Gang, Zhou, et al. "Polarization-induced charges in modulation-doped Al_xGa_{1-x}N/Ga_N heterostructures through capacitance-voltage profiling." *Chinese physics letters* 19.8 (2002): 1172.
- [93] Zervos, M., et al. "Investigation into the charge distribution and barrier profile tailoring in AlGa_N/Ga_N double heterostructures by self-consistent Poisson–Schrödinger calculations and capacitance–voltage profiling." *Journal of applied physics* 91.7 (2002): 4387-4393.
- [94] Miller, E. J., et al. "Direct measurement of the polarization charge in AlGa_N/Ga_N heterostructures using capacitance–voltage carrier profiling." *Applied physics letters* 80.19 (2002): 3551-3553.
- [95] Bernardini, Fabio, Vincenzo Fiorentini, and David Vanderbilt. "Accurate calculation of polarization-related quantities in semiconductors." *Physical Review B* 63.19 (2001): 193201.
- [96] Zhou, Lin, et al. "Measurement of polarization-induced electric fields in Ga_N/AlIn_N quantum wells." *Applied Physics Letters* 101.25 (2012): 251902.
- [97] Ambacher, O., et al. "Pyroelectric properties of Al (In) Ga_N/Ga_N hetero- and quantum well structures." *Journal of physics: condensed matter* 14.13 (2002): 3399.
- [98] Perillat-Merceroz, Guillaume, et al. "Intrinsic degradation mechanism of nearly lattice-matched InAlN layers grown on Ga_N substrates." *Journal of Applied Physics* 113.6 (2013): 063506.
- [99] Carlin, J-F., and M. Ilegems. "High-quality AlIn_N for high index contrast Bragg mirrors lattice matched to Ga_N." *Applied Physics Letters* 83.4 (2003): 668-670.
- [100] Sutherland, Danny. *Optical Characterisation of Non-polar InGa_N/Ga_N Quantum Wells*. 2015. University of Manchester, PhD dissertation.
- [101] Moses, Poul Georg, et al. "Hybrid functional investigations of band gaps and band alignments for AlN, Ga_N, In_N, and InGa_N." *The Journal of chemical physics* 134.8 (2011): 084703.

- [102] Böttger, H., and V. V. Bryksin. "Hopping conductivity in ordered and disordered solids (I)." *physica status solidi (b)* 78.1 (1976): 9-56.
- [103] Kaplar, R. J., et al. "Electroreflectance studies of Stark shifts and polarization-induced electric fields in InGaN/GaN single quantum wells." *Journal of applied physics* 95.9 (2004): 4905-4913.
- [104] Pohl, Udo W. *Epitaxy of semiconductors: introduction to physical principles*. Springer Science & Business Media, 2013.
- [105] Vennéguès, P., et al. "Nature and origin of V-defects present in metalorganic vapor phase epitaxy-grown (In_xAl_{1-x})N layers as a function of InN content, layer thickness and growth parameters." *Journal of Crystal Growth* 353.1 (2012): 108-114.
- [106] Ariel, V., et al. "Investigation of epitaxial Pp CdTe/Hg_{0.775}Cd_{0.225}Te heterojunctions by capacitance-voltage profiling." *Journal of electronic materials* 24.5 (1995): 655-659.
- [107] Rangel-Kuoppa, Victor-Tapio, Cesia Guarneros Aguilar, and Victor Sánchez-Reséndiz. "Electrical Properties Of GaN Layers Grown By Metal Organic Vapor Phase Epitaxy (MOVPE)." *AIP Conference Proceedings*. Vol. 1399. No. 1. AIP, 2011.
- [108] Akazawa, M., et al. "Measurement of valence-band offsets of InAlN/GaN heterostructures grown by metal-organic vapor phase epitaxy." *Journal of Applied Physics* 109.1 (2011): 013703.
- [109] Brown, David F., et al. "Growth and characterization of In-polar and N-polar InAlN by metal organic chemical vapor deposition." *Journal of Applied Physics* 107.3 (2010): 033509.
- [110] Miao, Z. L., et al. "The origin and evolution of V-defects in In_xAl_{1-x}N epilayers grown by metalorganic chemical vapor deposition." *Applied Physics Letters* 95.23 (2009): 231909.
- [111] Brillson, Leonard J., ed. *Contacts to semiconductors: fundamentals and technology*. Noyes publications, 1993.
- [112] Khotkevich, Andrei Vladimirovich, and Igor K. Yanson. *Atlas of point contact spectra of electron-phonon interactions in metals*. Springer Science & Business Media, 2013.
- [113] Goodman, Alvin M. "Metal—Semiconductor barrier height measurement by the differential capacitance method—One carrier system." *Journal of applied physics* 34.2 (1963): 329-338.
- [114] Willardson, Robert K., and Albert C. Beed. *Semiconductors and semimetals: contacts, junctions, emitters*. Academic Press, 1981.
- [115] Sharma, B. L., ed. *Metal-semiconductor Schottky barrier junctions and their applications*. Springer Science & Business Media, 2013.
- [116] Pollak, Fred H. "Study of semiconductor surfaces and interfaces using electromodulation." *Surface and interface analysis* 31.10 (2001): 938-953.
- [117] Aspnes, David E. "Third-derivative modulation spectroscopy with low-field electroreflectance." *Surface Science* 37 (1973): 418-442.
- [118] Hosea, T. J. C. "Estimating Critical-Point Parameters from Kramers-Kronig Transformations of Modulated Reflectance Spectra." *physica status solidi (b)* 182.1 (1994).

- [119] Misiewicz, J., and R. Kudrawiec. "Contactless electroreflectance spectroscopy of optical transitions in low dimensional semiconductor structures." *Opto-Electronics Review* 20.2 (2012): 101-119.
- [120] Yunovich, Alexander E., et al. "Electroreflectance Spectra of InGaN/AlGaIn/GaN pn-Heterostructures." *MRS Online Proceedings Library Archive* 955 (2006).
- [121] Avakyants, L. P., et al. "Electroreflectance spectra of InGaN/AlGaIn/GaN quantum-well heterostructures." *Semiconductors* 41.9 (2007): 1060-1066.
- [122] Yoon, J., et al. "Electroreflectance and photoluminescence study on InGaIn alloys." *JOURNAL-KOREAN PHYSICAL SOCIETY* 49.5 (2006): 2143.
- [123] Kudrawiec, R., et al. "Contactless electroreflectance of InGaIn layers with indium content $\leq 36\%$: The surface band bending, band gap bowing, and Stokes shift issues." *Journal of Applied Physics* 106.11 (2009): 113517.
- [124] Avakyants, Lev, et al. "The difference between reflectance and electroreflectance spectra of AlGaIn/GaN/InGaIn LED structures." *physica status solidi (c)* 9.3-4 (2012): 818-821.
- [125] Avakyants, Lev, et al. "Electroreflectance diagnostics of InGaIn/AlGaIn/GaN based LEDs structures." *physica status solidi (c)* 6.12 (2009): 2852-2854.
- [126] Shokhovets, S., R. Goldhahn, and G. Gobsch. "Study of the linear electro-optic effect in α -GaIn by electroreflectance." *Materials Science and Engineering: B* 93.1 (2002): 215-218.
- [127] Kuzmany, Hans. *Solid-state spectroscopy: an introduction*. Springer Science & Business Media, 2009.
- [128] Tang, X., et al. "Electrical characterization of zinc oxide thin films by electrochemical capacitance–voltage profiling." *Applied physics letters* 84.16 (2004): 3043-3045.
- [129] Reynolds, Neal D., Cristian D. Panda, and John M. Essick. "Capacitance-voltage profiling: Research-grade approach versus low-cost alternatives." *American Journal of Physics* 82.3 (2014): 196-205.
- [130] Xin-Hua, Wang, et al. "The physical process analysis of the capacitance—voltage characteristics of AlGaIn/AlIn/GaN high electron mobility transistors." *Chinese Physics B* 19.9 (2010): 097302.
- [131] Knübel, A., et al. "Nonuniformity of electron density in In-rich InGaIn films deduced from electrolyte capacitance-voltage profiling." *Applied Physics Letters* 96.8 (2010): 082106.
- [132] Iniewski, K., and C. A. T. Salama. "Optimization of the capacitance–voltage profiling method based on inverse modeling." *Journal of Vacuum Science & Technology B: Microelectronics and Nanometer Structures Processing, Measurement, and Phenomena* 10.1 (1992): 480-484.
- [133] Biswas, Dipankar, and Siddhartha Panda. "An effective approach for the minimization of errors in capacitance-voltage carrier profiling of quantum structures." *Journal of Applied Physics* 115.13 (2014): 134308.
- [134] Aghaei, Samira, et al. "Challenges and opportunities in atomistic dopant profiling using capacitance-voltage measurements." *Advanced Semiconductor Manufacturing Conference (ASMC), 2014 25th Annual SEMI. IEEE, 2014*.
- [135] Bobylev, B. A., et al. "Capacitance-voltage profiling of multiquantum well structures." *Solid-State Electronics* 41.3 (1997): 481-486.

- [136] Rimmer, J. S., B. Hamilton, and A. R. Peaker. "Capacitance-Voltage Profiling of Multilayer Semiconductor Structures." *Low-Dimensional Structures in Semiconductors*. Springer US, 1991. 139-146.
- [137] Tschirner, B. M., et al. "Capacitance-voltage profiling of quantum well structures." *Journal of applied physics* 79.9 (1996): 7005-7013.
- [138] Sundaram, M., and A. C. Gossard. "Capacitance-voltage profiling through graded heterojunctions: Theory and experiment." *Journal of applied physics* 73.1 (1993): 251-260.
- [139] Panda, Siddhartha, and Dipankar Biswas. "Inconsistent temperature dependence in capacitance-voltage profiling of quantum wells." *Journal of Applied Physics* 109.5 (2011): 056102.
- [140] Watanabe, Miyoko O., and Yasuo Ohba. "Interface properties for GaAs/InGaAlP heterojunctions by the capacitance-voltage profiling technique." *Applied physics letters* 50.14 (1987): 906-908.
- [141] Schubert, E. F., et al. "Spatial resolution of the capacitance-voltage profiling technique on semiconductors with quantum confinement." *Applied Physics Letters* 57.5 (1990): 497-499.
- [142] Schubert, E. F., J. M. Kuo, and R. F. Kopf. "Theory and experiment of capacitance-voltage profiling on semiconductors with quantum-confinement." *Journal of electronic materials* 19.6 (1990): 521-531.
- [143] Peter, Y. U., and Manuel Cardona. *Fundamentals of semiconductors: physics and materials properties*. Springer Science & Business Media, 2010.
- [144] Pollak, Fred H. "Modulation spectroscopy of semiconductors and semiconductor microstructures." *Handbook on Semiconductors 2* (1994): 527-635.
- [145] Aspnes, D. E. "Modulation Spectroscopy/Electric Field Effects on the Dielectric Function of Semiconductors, Handbook on Semiconductors, Vol. TS Moss." (1980): 109.
- [146] Papadimitriou, Dimitra N., et al. "Optimization of Electrochemically Deposited Highly Doped ZnO Bilayers on Ga-Rich Chalcopyrite Selenide for Cost-Effective Photovoltaic Device Technology." *Energies* 9.11 (2016): 951.
- [147] Stoklas, R., et al. "Trapped charge effects in AlGaN/GaN metal-oxide-semiconductor structures with Al₂O₃ and ZrO₂ gate insulator." *Semiconductor Science and Technology* 29.4 (2014): 045003.
- [148] Shen, H., et al. "Unambiguous evidence of the existence of polarization field crossover in a semipolar InGa_N/Ga_N single quantum well." *Applied Physics Letters* 95.3 (2009): 033503.
- [149] Dimopoulos, Hercules G. *Analog electronic filters: theory, design and synthesis*. Springer Science & Business Media, 2011.
- [150] Dimopoulos, Hercules G. "Optimal use of some classical approximations in filter design." *IEEE Transactions on Circuits and Systems II: Express Briefs* 54.9 (2007): 780-784.
- [151] Batchelor, R. A., and A. Hamnett. "A Franz-Keldysh model for photoreflectance from GaAs/GaAlAs heterojunction structures." *Journal of applied physics* 71.5 (1992): 2414-2422.
- [152] Wetzel, C., et al. "Piezoelectric Franz-Keldysh effect in strained GaInN/GaN heterostructures." *Journal of applied physics* 85.7 (1999): 3786-3791.

- [153] Clark, Terence J., et al. "The use of infrared interference spectra to measure ceramic coating thickness in a CVD reactor." *Thin solid films* 254.1-2 (1995): 7-9.
- [154] Alibert, C., et al. "Measurements of electric-field-induced energy-level shifts in GaAs single-quantum-wells using electroreflectance." *Solid state communications* 53.5 (1985): 457-460.
- [155] Shokhovets, S., R. Goldhahn, and G. Gobsch. "Study of the linear electro-optic effect in α -GaN by electroreflectance." *Materials Science and Engineering: B* 93.1 (2002): 215-218.
- [156] Aspnes, D. E. "Band nonparabolicities, broadening, and internal field distributions: The spectroscopy of Franz-Keldysh oscillations." *Physical Review B* 10.10 (1974): 4228.
- [157] Aspnes, D. E. "Band nonparabolicities, broadening, and internal field distributions: The spectroscopy of Franz-Keldysh oscillations." *Physical Review B* 10.10 (1974): 4228.
- [158] Shen, H., et al. "Direct measurement of piezoelectric field in a [111] B grown InGaAs/GaAs heterostructure by Franz-Keldysh oscillations." *Applied physics letters* 60.19 (1992): 2400-2402.
- [159] Yin, X., et al. "Photoreflectance study of the surface Fermi level at (001) n- and p-type GaAs surfaces." *Journal of Vacuum Science & Technology A: Vacuum, Surfaces, and Films* 10.1 (1992): 131-136.
- [160] Yang, Tao, et al. "Optical properties of GaN thin films on sapphire substrates characterized by variable-angle spectroscopic ellipsometry." *Japanese journal of applied physics* 37.10A (1998): L1105.
- [161] Shen, H., and Fred H. Pollak. "Generalized Franz-Keldysh theory of electromodulation." *Physical Review B* 42.11 (1990): 7097.
- [162] Pollak, Fred H., and H. Shen. "Modulation spectroscopy of semiconductors: bulk/thin film, microstructures, surfaces/interfaces and devices." *Materials Science and Engineering: R: Reports* 10.7 (1993): xv-374.
- [163] White, Peter. "Group delay explanations and applications." *Applied Radio Labs*(1999): 1-6.
- [164] STR group. "Material Properties of AlInGaN Alloys." STR Group - Materials Properties of InAlGaN Alloys, www.str-soft.com/learn/InAlGaN_Alloys/.
- [165] Wright, A. F. "Elastic properties of zinc-blende and wurtzite AlN, GaN, and InN." *Journal of Applied Physics* 82.6 (1997): 2833-2839.

PERSONAL INFORMATION



Georgios G. Roumeliotis

📍 8, Ippokratous, Aniksi, Attiki, 14569
15, Suarezstraße, Berlin, 14057, room 505
☎ +30 2108142742 📠 +30 6997120016, +49 01748917919
✉ g_roumeliwth@hotmail.com

Sex: Male | Date of birth: 22/06/1985 | Nationality Greek

2015 - present

Materials Science & Engineering M.Sc.

Interdisciplinary Interdepartmental Postgraduate Program involving various schools of the National Technical University of Athens, coordinated by the School of Chemical Engineering (NTUA).

- First 2 semesters courses with Grade-Point Averages of 8.1/10 and 8.6/10. Courses description at <http://mse.ntua.gr/%CE%BC%CE%B1%CE%B8%CE%AE%CE%BC%CE%B1%CF%84%CE%B1/?lang=en#1460471315259-5bab95d9-2eb3>.

Master Thesis partly elaborated at NTUA (until December 2016) and partly (and currently) at TU-Berlin (Institute of Solid State Physics) until 31.08.2017. The last part of the MSc Thesis (September-October 2017) will also be elaborated at NTUA.

2014 - 2015

Prerequisite studies for Materials Science & Engineering M.Sc.

NTUA School of Chemical Engineering

- Coursework and examination of two semesters in four prerequisite courses of semesters 5th, 7th, 8th and 8th, (7.8/10) for the admission to IIPP Materials Science and Engineering M.Sc., NTUA

2004 - 2008, 2014

Electronics Engineering B.Sc.

Piraeus University of Applied Sciences

(former Technological Education Institute of Piraeus, Greece)

- ECTS Credits: 240
- 8 Semesters (Including 6 Months Internship and Thesis)
- 7.24/10, (6th highest grade out of 123 students)
- Thesis Title:
“Organic photovoltaic cells using cuprous oxides/sub oxides for efficient hole collection”

(in collaboration with the Institute of Nanoscience and Nanotechnology of the National Center for Scientific Research, NCSR “Democritus”)

Courses description at <http://www.electronics.teipir.gr/index.php/en/2016-02-01-10-11-06/2016-02-01-10-12-32/undergraduate-curriculum>

OTHER STUDIES

- 1993 - 1997, 1998 - 2000 Piano Lessons (6 years) and Theory of Music (3 years) in the National Conservatoire of Greece
- 2000 Cambridge FCE (Grade B, B2 equivalent)

WORK EXPERIENCE

- 2014 (6 months) Internship in National Center for Scientific Research (NCSR) "Democritus" Practice Laboratory
- Thin Films Laboratory (Chemical Vapour Deposition Laboratory), Design and construction of a low cost, audio frequency generator, of controlled frequency (8 Hz- 24kHz) and controlled voltage 0 - 230 VAC rms, as a power supply to Electroluminescent Ink Devices

OTHER SKILLS

- 2000-present Professional Musician & Music Teacher
- Vocals
 - Electric Guitar
 - Acoustic Guitar

Amateur Photographer

LIST OF PUBLICATIONS

- Publications relative to the MSc Thesis
- Dimitra N. Papadimitriou, Georgios Roupakas, Georgios G. Roumeliotis, Patrick Vogt, and Tristan Köhler "Optimization of Electrochemically Deposited Highly Doped ZnO Bilayers on Ga-Rich Chalcopyrite Selenide for Cost-Effective Photovoltaic Device Technology." *Energies* 9.11 (2016): 951.
- Pending publications relative to the MSc Thesis
- Norman Susilo, Georgios G. Roumeliotis, Monir Rychetsky, Martin Guttmann, Michael Narodovitch, Tore Niermann, Tim Wernicke, Michael Lehmann, Bernd Witzigmann, Dimitra N. Papadimitriou, and Michael Kneissl "Accurate determination of polarization fields in (0001) c-plane InAlN/GaN heterostructures with Capacitance-Voltage-Measurements", *physica status solidi*
- Pending publications relative to the MSc Thesis
- Georgios G. Roumeliotis, Norman Susilo, Martin Guttmann, Tim Wernicke, Dimitra N. Papadimitriou, and Michael Kneissl "Polarization Fields and Electro-Optical Response of (0001) c-plane InGaN/GaN and InAlN/GaN heterostructures studied by Capacitance-Voltage, Electroluminescence Spectroscopy"